Ultrathin Cobalt Films on Ruthenium (0001): Growth, Structure, and Magnetism

Farid El Gabaly Márquez
of
Universidad Autónoma de Madrid
—2006—

A dissertation submitted to the Universidad Autónoma de Madrid
in fulfillment of the thesis requirement for the degree of Doctor of Philosophy in Physics

Abstract

In this thesis we study the growth, structure, and magnetism of ultrathin films of cobalt on ruthenium (0001). The first step is to understand the structure of the clean Ru(0001) surface. While a perfect hcp (0001) surface has three-fold symmetry, the diffraction patterns commonly obtained are six-fold symmetric. This apparent change in symmetry occurs because on a stepped surface, the geometry of the atomic layers on adjacent terraces are rotated by 180 degrees. We use a Low-Energy Electron Microscope (LEEM) to acquire the three-fold diffraction pattern from a single hcp Ru terrace and measure the intensity-vs-energy curves for several diffracted beams. By means of multiple scattering calculations fitted to the experimental data with a Pendry R-factor of 0.077, we find that the surface is contracted by 3.5($\pm$0.9)% at 456 K.

We follow then the layer-by-layer growth of cobalt on ruthenium by means of LEEM and Low Energy Electron Diffraction (LEED). At suitable deposition temperature around 700 K, each layer forms through nucleation-and-growth of triangular islands. The first monolayer grows pseudomorphically in the hcp stacking sequence. The vertical lattice spacing is contracted by 4% relative to the bulk ruthenium value. In films thicker than a monolayer the in-plane lattice spacing is relaxed. The resulting superstructures produce satellite spots in the diffraction patterns. In three monolayer thick regions, additional stacking faults located at the topmost Co layer can be identified. These stacking faults are associated with distinct island shapes and unique diffraction spectra.

By means of Spin-Polarized LEEM (SPLEEM), we show that the magnetic easy axis of one to three atomic-layer thick cobalt films on Ru(0001) changes its orientation twice during deposition: One-monolayer and three-monolayer thick films are magnetized in-plane, while two-monolayer films are magnetized out-of-plane. The Curie temperatures of films thicker than one monolayer are well above room temperature. Fully relativistic calculations based on the screened Korringa-Kohn-Rostoker method demonstrate that

the interplay between strain, surface, and interface effects lead to perpendicular magnetization only for two-monolayer cobalt films.

Finally, we report the spin-reorientation transition that takes place on three and four cobalt layers on Ru(0001) upon copper deposition. The bare films present an in-plane magnetization in remanence. By means of SPLEEM we observe in real space and real time with nanometer resolution how the magnetization changes from in-plane to perpendicular orientation when depositing a single copper atomic layer. Deposition of an additional copper layer drives the magnetization in-plane again. No other thicknesses below six cobalt layer show such behavior.

Presentación

En esta tesis hemos estudiado el crecimiento, la estructura y la imanación de películas delgadas de cobalto en rutenio (0001). Para realizar un estudio completo hemos comenzado con la superficie limpia del Ru(0001). Mientras que una superficie ideal hcp (0001) tiene simetría de orden tres, los patrones de dirección que se obtienen comúnmente presentan simetría seis. Este cambio de simetría aparente se debe a que en una superficie escalonada, la disposición de los átomos en terrazas adyacentes está rotada 180 grados. En esta tesis hemos usado microscopía de electrones lentos (Low Energy Electron Microscopy, LEEM) para medir el patrón de difracción de simetría de orden tres de una terraza del Ru sin escalones y hemos medido la intensidad de los haces difractados en funcin de la energía de los haces incidentes. Mediante cálculos de dispersión múltiple hemos ajustado los datos experimentales con un factor R de Pendry de tan solo 0.077. Hemos encontrado que la superficie se haya contraída un 3.5($\pm$0.9)% a 456 K.

Hemos observado el crecimiento capa a capa de cobalto en rutenio mediante LEEM y difracción de electrones lentos (LEED). A una temperatura de alrededor de 700 K, cada capa se forma mediante la nucleación y el crecimiento de islas triangulares. La primera monocapa crece con el mismo parámetro de red en el plano de la película que el substrato, y con estructura hexagonal compacta (hcp). La capa de cobalto está contraída un 4 % en vertical con respecto al valor del rutenio en volumen. En películas más gruesas que una monocapa el parámetro de red en el plano está relajado. Las superestructuras resultantes producen haces satélite en los patrones de difracción. En las regiones de tres monocapas de grosor podemos identificar fallas de apilamiento en la última capa de Co. Dichas fallas de apilamiento son identificadas debido a una orientación diferente de las islas y a un espectro de difracción característico.

Mediante microscopía de electrones lentos con polarización de espín (Spin Polarized LEEM, SPLEEM) hemos detectado que el eje fácil de imanación del sistema compuesto

por entre 1 y 3 capas atómicas de cobalto en Ru(0001) cambia su orientación dos veces durante el crecimiento: las películas con una y tres monocapas están imanadas en el plano, mientras que las películas de dos monocapas están imanadas fuera del plano, de forma perpendicular a la superficie. Las temperaturas de Curie para películas de más de una monocapa están muy por encima de temperatura ambiente. Hemos demostrado mediante cálculos totalmente relativistas basados en el método de Korringa-Kohn-Rostoker apantallado que sólo para películas de dos monocapas de cobalto la interacción entre los efectos producidos por las tensiones, la superficie y la intercara pueden desembocar en un eje fácil de imanación perpendicular.

Hemos estudiado con SPLEEM el efecto de cubrir con películas de cobre 3 y 4 capas de Co en Ru(0001). Las películas de 3 y 4 capas de Co/Ru están imanadas en el plano. Mediante SPLEEM hemos observado en tiempo real y en el espacio real con resolución nanométrica cómo la imanación cambia su orientación a perpendicular cuando depositamos una capa atómica de Cu. Depositando una capa más de Cu cambia la dirección de la imanación a dentro del plano. No hemos observado más cambios en la superficie o estructura. Las reorientaciones del eje fácil de imanación no ocurren para otros grosores de Co por debajo de seis monocapas.

Declaration

This dissertation is the result of my own work, except where explicit reference is made to the work of others, and has not been submitted for another qualification to this or any other university.

Farid El Gabaly

Thesis Advisor: Juan de la Figuera

Acronyms and Abbreviations

AES Auger Electron Microscopy

DFT Density Functional Theory

eE Electron Energy

fcc Face-Centered Cubic

FOV Field Of View

fps Frames Per Second

hcp Hexagonal Close-Packed

IV Intensity-Voltage

LEED Low Energy Electron Diffraction

LEEM Low Energy Electron Microscopy

LBNL Lawrence Berkeley National Laboratory

MAE Magnetic Anisotropy Energy

MEM Mirror Electron Microscopy

ML Monolayer

NCEM National Center for Electron Microscopy

NN Nearest Neighbor

PEEM Photoemission Electron Microscopy

PMA Perpendicular Magnetic Anisotropy

QSE Quantum Size Effect

SBZ Surface Brillouin Zone

SKKR Screened Korringa-Kohn-Rostoker

SNL Sandia National Laboratories

SPLEEM Spin Polarized Low Energy Electron Microscopy

SRT Spin-Reorientation Transition

SV Start Voltage

SXRD Surface X-Ray Diffraction

TEM Transmission Electron Microscopy

UHV Ultra High Vacuum

VLEED Very Low Energy Electron Diffraction

Preface

Over the last four decades the demand for increased magnetic recording density was achieved by scaling the magnetic bits. Fundamental physical properties, like superparamagnetic effects [1], no longer allow simple scaling approach. Most of the current magnetic storage media uses longitudinal recording, in which the bits magnetization direction is in the film plane. In contrast, the magnetization in perpendicular recording media is in a direction normal to the surface plane. Perpendicular magnetic recording has been shown to allow a further increase of the recording density. Some advantages of the perpendicular recording media compared with the longitudinal recording media are: higher thermal stability, higher signal, lower medium noise and sharper bit transition. It is anticipated that the recording media industry will eventually switch to perpendicular recording technology. The recording media research is one of the many fields in which the fundamental research and the end-user application gets closer in time every day. In this thesis we study two novel perpendicularly magnetized thin-film systems (Co/Ru and Cu/Co/Ru) with atomic detail by means of state-of-the-art surface science experimental techniques.

Surface and thin-film physics has in recent decades become one of the main subdisciplines within the condensed matter physics. Furthermore, these research fields are of fundamental importance in many applied fields, like nanoelectronics, thin-film recording media, catalysis or nanostructured materials. Since the early days of surface science, lateral averaging measurement techniques (like AES, LEED, RBS, XPS...) have provided considerable understanding of surfaces. But it has become evident that many problems can only be solved with non lateral averaging techniques, like the STM. STM was discovered in the 1980s and it has revolutionized the whole way to understand surfaces. Ten years after the discovery of the STM, Ernst Bauer presented the first working Low Energy Electron Microscope (LEEM) [2]. The LEEM shows us in real time some typical surface dynamics processes like growth, sublimation, stacking changes, clouds

of adatoms, phase transitions and more. Some years later, and using a spin polarized electron gun, the Spin Polarized LEEM (SPLEEM) [3] surprises us in a similar way. It shows for the first time non time- or space-averaged images of ferromagnetic domains at the surface. It has been used to measure the magnetization direction of surface layers, to image the domains dynamics (coalescence, fluctuations) and more. We have used LEEM to study in detail the structure of the Ru(0001) surface, the growth and structure of the first atomic layers of Co on Ru(0001) and the effect of Cu capping layers over Co/Ru(0001) films. We used SPLEEM to study the magnetic structure and the spin reorientation transitions (SRT) that both systems (Co/Ru and Cu/Co/Ru) present.

Cobalt on Ruthenium is a system that has been popular for magnetic studies, but not so much for structure determinations. Ru is used to induce antiferromagnetic coupling between thin films of Co-alloys in both spin-valves and magnetic recording media [4]. We study thin-film magnetism and structure in Co on Ru because its components do not intermix too much. Previous work [5, 6] has shown that the easy axis of magnetization in Co/Ru multilayers changes from perpendicular at low Co thickness to in-plane for films thicker than 7 ML [7]. Because the Co films did not grow layer-by-layer [8, 9], the films contained islands of varying thickness. Previous studies detected that Co on Ru grows in Stranski-Krastanov growth mode [8–10], and under these conditions, determining precisely how the magnetization changes and why, as a function of film thickness is quite taxing. Under appropriate substrates and growth conditions we show here that Co can be grown on Ru(0001) layer-by-layer up to 10 monolayers [11].

The thesis begins (chap. 1) with a review of two fundamental issues (epitaxy and thin film magnetism) that we consider relevant to understand the methods and results presented. In chap. 2 we explain the elements and capabilities of the experimental equipment used, basically the LEEM and the SPLEEM. Both microscopes are not yet widely known instruments by the surface science researchers, so we briefly review them. Chap. 3 presents LEEM experiments on the clean Ru(0001) surface. Ru(0001) is the substrate used to grow all the thin films studied in this work. In conjunction with LEED-IV curves fit, we determined the structural parameters of the Ru(0001) surface. Chap. 4 and chap. 5 show the results in the structural and magnetic studies of the first monolayers of Co on Ru(0001). Growth dynamics and the structure of every layer up to three layers is presented in chap. 4. In chap. 5 the magnetization of each film has been characterized, discovering two SRTs. The film magnetization easy-axis changes from an in-plane orientation for monolayer thick films, to perpendicular to the surface for bilayer islands or films, and finally to in-plane again for thicker islands or films. The

last chapter of the thesis (chap. 6) describes, from an experimental point of view, how the addition of Cu induces another double SRT in films with 3 and 4 ML Co/Ru(0001): from in-plane to perpendicular with 1 ML Cu on top and from perpendicular to in-plane with 2 ML Cu.

Farid El Gabaly
Madrid, October 2006

♡ *A Carlota y Micaela . . .* ♡
por todo.

— F.G.M.

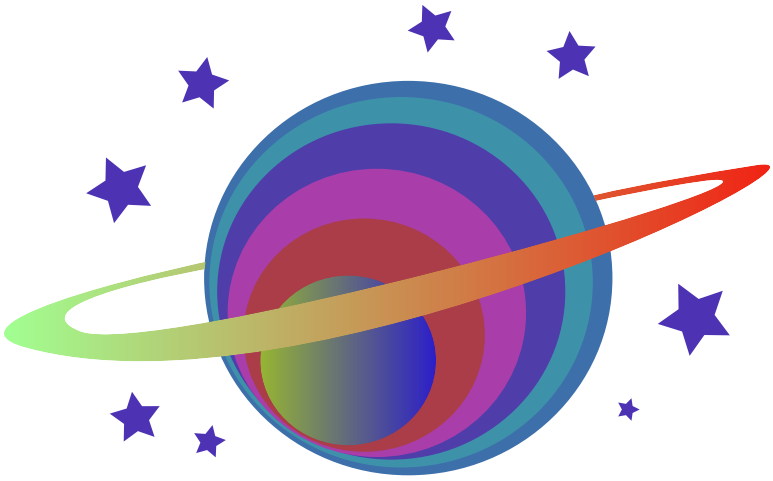

Contents

Chapter 1

Fundamentals of Epitaxy and Surface Magnetism

"Let's cultivate the Science by itself, leaving apart the applications for the moment. They always arrive, some times after years; some time after centuries"

— *Reglas y Consejos Sobre Investigación Científica*, Santiago Ramon y Cajal, 1852–1934

This chapter gives an introduction to some fundamental aspects of the epitaxial growth, surface magnetism and spin-reorientation transitions (SRT) of metallic materials. Reviewing all these basic concepts will be helpful to understand the work presented in this thesis: all the films investigated in this work were grown epitaxially over a Ru(0001) substrate; Co/Ru(0001) and Cu/Co/Ru(0001) present multiple SRTs.

1.1 Epitaxy

The word epitaxy, from Greek, (*epi* – over; *taxis* – arrangement) is used to designate the growth *over a substrate of different chemical nature*. The ability to create new materials with new properties simply by deposition of one of them on top of another is the most extended approach of the solid state and materials scientist. The new properties sometimes arise from the low dimensionality of the structures formed. Some times, specific properties of the materials change when they are mixed, even when the

mixture involve extremely small amounts of one of them. In both cases, to control the deposition process of the adsorbate (guest material) on top of the substrate (host material) will give us relevant information that can always be used to understand the change in the observed new properties.

An adsorbate will not always grow in an ordered way on top of a substrate. In fact, to grow small amounts of defect-free crystalline material on top of a preexisting crystal is not straightforward. To achieve the growth, the surface adhesion energy[1] ,also called the interfacial interaction energy or γ_{i}, must be considerable (~ -1 to -10 eV/atom). If γ_{i} is not strong enough, the adsorbate will not *wet* the surface and will probably grow three-dimensionally (in 3D clusters) to reduce the contact area with the substrate (see Fig. 1.1a). If the adhesion is strong , i.e. the substrate-adatom interaction γ_{i}, is comparable to the adatom-adatom[2] interaction (γ_{f}), and if there is a clear structural relation (similar crystalline symmetry, low misfit[3] between the species), then epitaxy takes place. There is an old rule [12] that states that epitaxial growth is expected if the misfit is smaller than 14%, but it has been impugned by more recent works that take more detailed view of the problem.

If we know the surface free energy of the substrate (γ_{s}) and that of the film (γ_{f}) as well as the interfacial interaction energy (γ_{i}) for every layer, the growth mode can be predicted using Bauer's criteria [13]. It can be summarized as follows:

$$\begin{aligned} \Delta\gamma = \gamma_{\mathrm{f}} + \gamma_{\mathrm{i}} - \gamma_{\mathrm{s}} \quad &\leq 0 \quad \text{layer + islands growth (Frank-van der Merve)} \\ &> 0 \quad \text{three dimensional growth (Volmer-Weber)} \end{aligned}$$

suggesting, in particular, that the growth of a substance on itself is considered Frank-van der Merve. It is evident that, with a high layer-substrate interaction (high γ_{i}), the guest crystal will perfectly *wet* the surface for one monolayer[4] (sometimes even more) with different structure in general to the one it would have in the bulk. As the adsorbate atomic layers grow with a substrate-induced structure, the binding energy of this layers becomes weaker due to the increasing distance with the bulk, which is the responsible of the in-

[1] The surface adhesion energy is the equivalent of the cohesion energy but for two different materials and in the surface. The surface adhesion energy per atom is the energy needed to remove (move to an infinite distance) one adsorbate atom from the substrate surface.

[2] An adatom is an atom adsorbed on a crystal surface so that it can migrate over the surface.

[3] The lattice misfit is defined as $(a - b)/b$, with a and b the interatomic in-plane distances of the adsorbate and the substrate respectively, in their natural crystalline structure along a common direction.

[4] A monolayer (ML), is defined as a concentration of deposited or adsorbed atoms onto a substrate equal to the number of atoms per surface unit of the substrate.

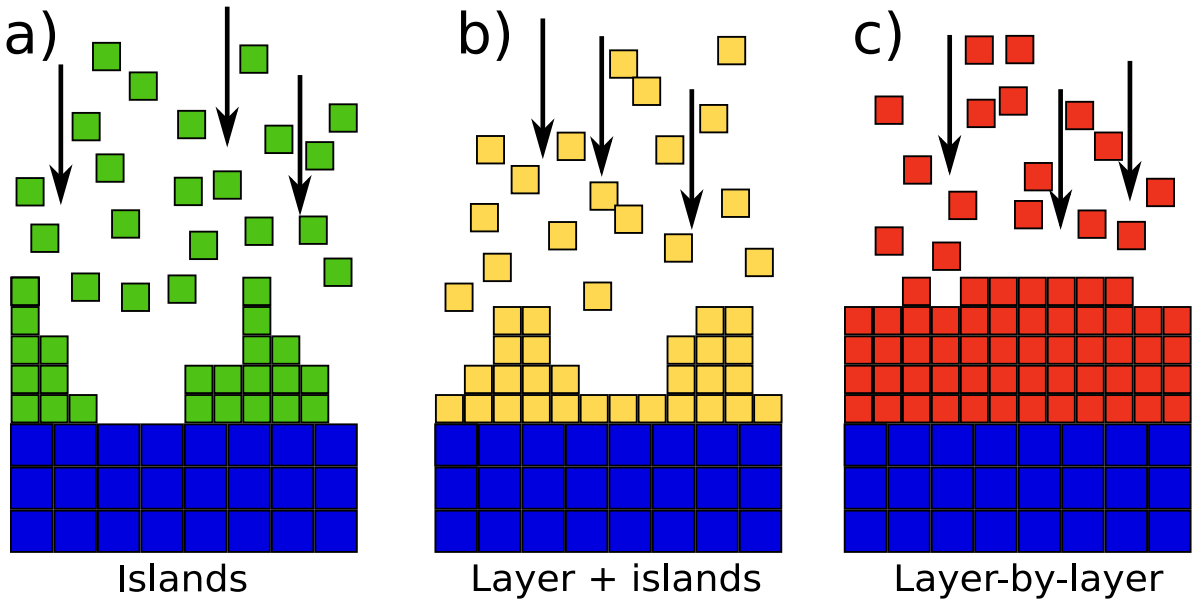

Figure 1.1: Schematic representation of the three main growth modes of a film on a surface. Alternative names are: a) Volmer-Weber, b) Stranski-Krastanov, c) Frank-van der Merve.

duced structure. Also, the structure cannot converge to the bulk material structure when the number of layers increase, as they have started with a wrong structure[5]. Beyond some critical thickness the new condensation of adatoms proceeds three-dimensionally. This makes the, a priori counterintuitive, Stranski-Krastanov (Fig. 1.1b) growth mode common. Actually it is the most widespread among technologically interesting films.

If the misfit is small, the ratio $\Delta\gamma$ is positive and the growth conditions (kinetic conditions) are appropriate, it is possible to smoothly adapt the substrate lattice parameter to the adsorbate lattice parameter by the generation of interfacial dislocations[14], allowing the adsorbate material to growth layer-by-layer (Fig. 1.1c) for many layers. However, layer-by-layer growth does not mean that the layers are growing pseudomorphically, i.e. with exactly the same structure of the substrate. In a pseudomorphic growth of two different materials, the misfit between them will generate strain (for soft adsorbate/hard substrate), i.e. expansion and/or contraction of the natural lattice distance of the adsorbate. Generally, the misfit between the adsorbate and the substrate makes it unfavorable for the growing material to follow the surface structure for too many layers.

To adopt a different in-plane lattice parameter, the growing material will usually

[5]The evolution to the bulk structure can be achieved through the introduction of defects.

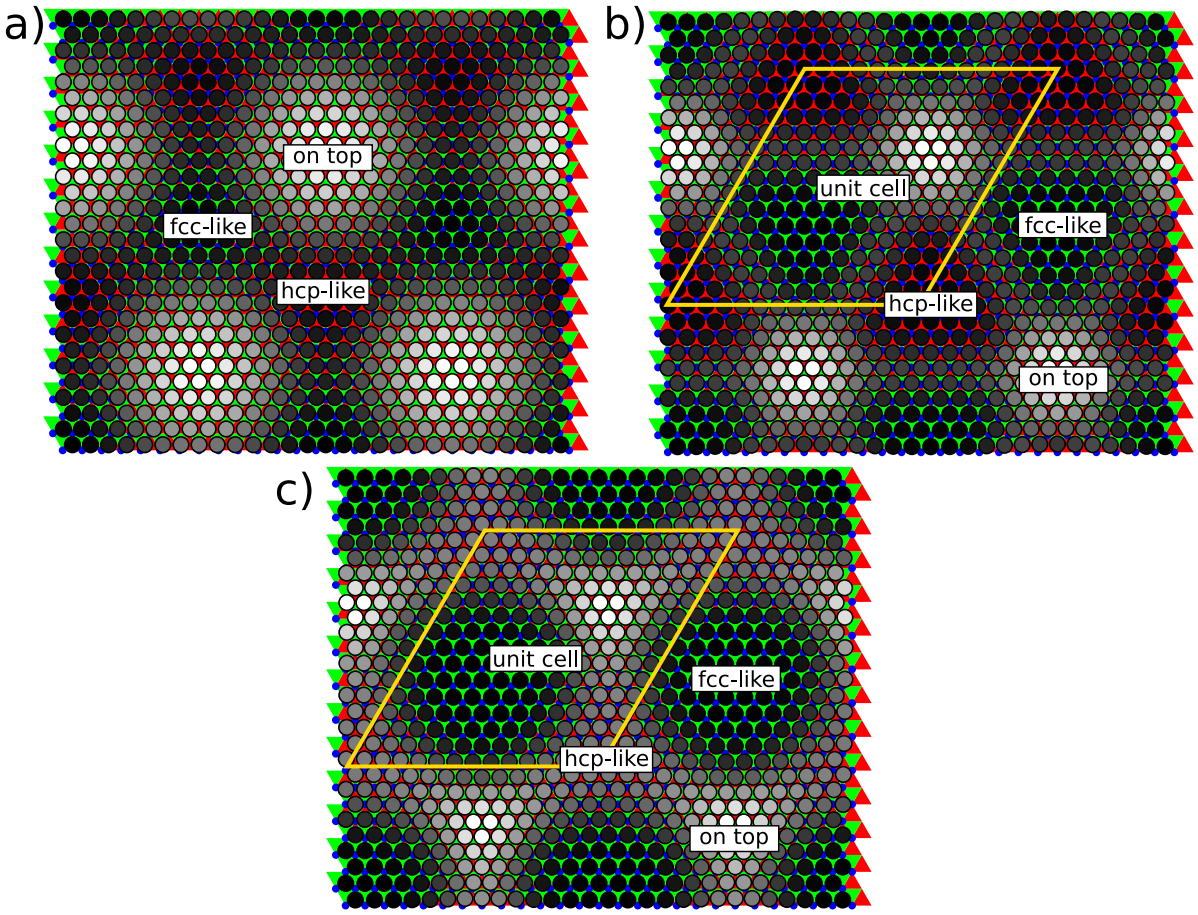

Figure 1.2: Moiré structure formation. a) Schematic representation of a moiré pattern (top view) structure obtained by the superposition of an adsorbate layer with different periodicity (28 atoms) on top of an hexagonal substrate (24 atoms). The blue circles represent the topmost layer of the substrate. The green and red triangles underneath are drawn to make easier the distinction between fcc and hcp sites. The grey circles represent the adsorbate layer and its brightness the position with respect to the layer below: brighter atoms are close to or in on-top position and the darker ones close to or in an hexagonal compact position. b) The resulting structure after a relaxation [15] based on a Frenkel-Kontorova [16] model with a Morse potential [17] between adsorbate atoms, in which the fcc and the hcp structure have the same energy. c) Schematic prediction of a similar structure in the case of having an adsorbate with fcc preferential stacking. In this case, the fcc regions are larger than the hcp, on-top and bridge (intermediate positions) regions.

produce a moiré like structure. A moiré pattern is achieved by putting one lattice on top of another, both with different in-plane lattice spacings. An example of the typical resulting moiré for an hexagonal compact atomic-layer structure can be seen (top view) in Fig. 1.2a. The direct superposition of different-periodicity atomic planes will place some of the top layer atoms in the less favorable[6] on-top position. If we let the system evolve the system (relax), by means of a simple Frenkel-Kontorova model [16] we obtain a more realistic situation (Fig. 1.2b), where the atoms close to on-top positions have moved to the closest high-coordination position, hcp or fcc[7]. The unit cell of the relaxed structure has now both fcc and hcp stackings (and some intermediate positions), and is much bigger than the pseudomorphic unit cell. If the growing material has the fcc stacking as preferential stacking, the structure would be similar to the one shown in Fig. 1.2c, with bigger fcc regions and smaller hcp regions.

To study and understand the fundamentals of many of the properties that ultrathin films exhibit, it is desirable to grow the adsorbate material in crystalline form, layer-by-layer and to know the detailed structure at every layer. In this thesis we will follow this easy-to-explain-but-hard-to-perform scientific procedure to understand the layer-by-layer structure and magnetism of cobalt on ruthenium (0001).

1.2 Thin Film Magnetism and Spin-Reorientation Transitions

Research in thin film magnetism has undergone a revolution since the discovery of (i) films with an easy-axis of magnetization perpendicular to the film plane [18] and (ii) the giant magnetoresistance effect (GMR) [19, 20]. An obvious reason for the increasing research in magnetic thin films is the important practical applications of these two discoveries.

Ultrathin films are one of the best approach to two-dimensional systems. It is, therefore, expected to observe a noticeable change in their magnetic properties. The parallel alignment of the magnetic moments of the atoms due to the exchange interaction is the basis of the spontaneous magnetization in ferromagnetic metals. In bulk $3d$ ferromagnets

[6] For metals.

[7] Using hcp and fcc labels in ultra thin films is some times confusing. The reason is that three layers are needed in order to define the stacking sequence. In Fig. 1.2 we use the last two (non-reconstructed) layers of the substrate, that is hcp, to study the stacking. Stacking sequences end in the following way (the notation is substrate/adsorbate): fcc= BABA/C, and hcp=BABA/B.

like Fe, Co and Ni, the orbital magnetic moment is almost quenched due to the hight symmetry of the arrangement of the surrounding atoms in the crystal. In ultrathin films, the reduction in the coordination number due to the absence of part of the surrounding atoms, and the strain due to the epitaxial growth on the substrate [21] partly lift this quenching. Finite size effects are responsible of another thin film magnetic effect, the decrease of the Curie temperature with the decreasing layer thickness [22, 23].

1.2.1 Main contributions to the total energy in a ferromagnet

In absence of external field the three main contributions [24–27] to the magnetic energy in a ferromagnet are the exchange energy, the magnetocrystalline anisotropy energy and the magnetostatic energy (or demagnetizing energy, responsible for the shape anisotropy).

Exchange interaction energy

The exchange interaction between electron spins, of quantum mechanical origin, tries to align and keep parallel the adjacent spins on a ferromagnet, in spite of the thermal agitation, which tends to randomize any atomic-level order. This produces spontaneous magnetization[8] and is responsible of the long-range magnetic order [27]. Its contribution to the energy can be written (using the Heisenberg model) as $E_{\mathrm{X}} = -J\mathbf{S}_i \cdot \mathbf{S}_j$, where J is the exchange constant ($J > 0$ for ferromagnets and $J < 0$ for antiferromagnets) and $\mathbf{S}_{i,j}$ are the spins of the electrons i, j. The exchange interaction is a direct consequence of the Pauli's exclusion principle, and hence it is of electrostatic nature [27]. For a given ferromagnetic material the long-range order abruptly disappears at a certain temperature which is called the Curie temperature for the material.

Magnetocrystalline anisotropy energy

The magnetocrystalline anisotropy energy is the consequence of the coupling of the electron spin with its surroundings, i.e. the crystal lattice, by means of the spin-orbit interaction. It is responsible for the alignment of the magnetization along some preferred crystallographic directions. Its energy contribution can be written, in its simplest form[9],

[8] Magnetization is defined as the density of effective magnetic dipole moments [28].

[9] For metals with empirically-demonstrated uniaxial anisotropy, like Co, and considering only the first term in an expansion series. In general it strongly depends on the lattice geometry.

as: $E_{\mathrm{A}} = K \sin^2 \theta$, where K is the anisotropy constant and θ is the angle between the actual magnetization direction and the *easy* axis of magnetization. This expression makes clear that, in the simplest case, there are two orientations degenerate in energy (note the quadratic sine dependence). The physical meaning of having two degenerate values is that the sign of the magnetization can be chosen arbitrarily[10]. Every change in the lattice constants will produce an effect in the magnetization. If the lattice is strained along a certain direction, for example, the magnetoelastic [29, 30] anisotropy can overcome the magnetocrystalline term. Historically, the magnetocrystalline anisotropy and the *magnetoelastic anisotropy* are distinguished from each other. However, on a microscopic level they both arise from the same mechanism, i.e. spin-orbit interaction superimposed to the atomic structure and bonding.

Néel [31] was the first to predict that the magnetic anisotropy would be considerably different at the surface of ferromagnets compared to the bulk. The reasons for that are the missing bonds and the incompletely quenched orbital moment. The experiments of Gradmann [32] in 1969 verified that surface or interface induced magnetocrystalline anisotropy of ultrathin ferromagnetic films can be strong enough to produce perpendicular magnetic anisotropy (PMA).

Magnetostatic energy

By minimizing the above mentioned energy terms, a ferromagnet would align all its spins along the easy axis of magnetization determined by the magnetocrystalline anisotropy (single domain state). However, when a ferromagnet is in a single domain state, the demagnetization field[11] could be very large because of the strong magnetic poles at the surface, which rises the total energy of the system trough the magnetostatic energy term. The magnetostatic energy term increases with the demagnetization field[12]. Its contribution to the total energy can be written as $E_{\mathrm{D}} = \mu_0/2 \times (N_x M_x^2 + N_y M_y^2 + N_z M_z^2)$, where μ_0 is the vacuum permeability and $M_{x,y,z}$ the magnetization vector per unit volume. $N_{x,y,z}$ is the trace of the demagnetization tensor (also called demagnetization constant)

[10] It actually means that magnetism is invariant upon time-inversion.

[11] Within a uniformly magnetized ferromagnet with a finite shape, the magnetization of the material itself generates a magnetic field in the opposite direction from the direction of the magnetization, a demagnetization field (usually denoted by H_{d}). The demagnetization field is created by unpaired surface magnetic poles and always exists as long as the size of the material is finite [33].

[12] Actually, it also depends on the stray field. The stray field is the magnetic field produced by the unpaired surface magnetic poles of the ferromagnet outside the sample. To minimize the magnetostatic energy we must minimize both fields by avoiding unpaired magnetic poles.

that fulfills $N_x + N_y + N_z = 1$ and depends only on the exact shape of the sample. For that reason this term is also called the shape anisotropy energy.

Ultrathin films can be described by an ultrathin disk for which $N_x = N_y = N_\parallel$ and $N_z = N_\perp$, and the shape anisotropy is given by $E_\mathrm{D} = \mu_0/2 \times (N_\perp - N_\parallel)M^2$. For an ideal ultrathin infinite disk $N_\parallel = 0$ and $N_\perp = 1$, that means that the demagnetizing field is maximum if the sample is magnetized perpendicularly to the disk surface and zero if the sample is magnetized in-plane[13]. Hence, the shape anisotropy contribution, which results from the long-range magnetic dipole-dipole interaction [27], will always favor an in-plane magnetization direction for ultrathin films (that minimizes the field).

Total magnetic anisotropy energy (MAE)

In a three-dimensional system, the maximum value of the shape anisotropy energy is taken when all the spins point in the same direction[14], because the demagnetization field will be larger in that direction. Hence, it is favorable energetically to align the spins parallel only in certain regions of the ferromagnet, with different direction from region to region to minimize the surface magnetic poles [33] responsible of the demagnetizing field. These regions are called *magnetic domains* [26]. The balance between the exchange and the magnetostatic energy explains the existence of the domains. The magnetization is oriented along an easy axis direction within them.

Only at *domain walls* [26] the magnetization deviates from the easy axis direction within a, in general, narrow region. The balance between the exchange and magnetocrystalline energy explains the width of the domain walls. The exchange interaction tries to keep the spins parallel, and will favor large width domain walls. Magnetocrystalline anisotropy, on the other hand favors abrupt changes in domain walls[15].

A reduction in the dimensionality affects the MAE. The demagnetization constant can be zero if, in an ultrathin film, as stated above, the magnetization is parallel to the surface plane ($N_\parallel = N_\perp = E_\mathrm{D} = 0$)— this predicts a single-domain situation, due to the fact that the existence of domains cannot reduce further the magnetostatic energy. In contrast, perpendicularly magnetized ultra thin films generally present domains[16] [27].

[13] The stray field of an ultrathin infinite disk magnetized in-plane or perpendicular is zero.

[14] The exchange interaction tries to orient them in the same direction.

[15] Perpendicularly magnetized thin films usually present narrow domain walls (∼10 nm) because the anisotropy is strong. On the other hand, in-plane magnetized films usually present wider domain walls (10–500 mn).

[16] The creation of domains in a perpendicularly polarized ultrathin infinite disk produce stray field

In thin films the dominating term is often the shape anisotropy which, as stated above, favors an in-plane orientation of the magnetization. However, other contributions such as the bulk, interface and surface magnetocrystalline anisotropy energies, as well as magnetoelastic terms [29, 30], can compete with the shape anisotropy and can favor a perpendicular magnetization direction. In this thesis the MAE is calculated as the difference of the total magnetic energy for an in-plane and a perpendicular magnetization[17]. A positive MAE corresponds to a perpendicular magnetization.

1.2.2 Spin-reorientation transitions

A spin-reorientation transition (SRT) describes the change of the easy axis of magnetization. It can be a change between in-plane and perpendicular (or vice versa), or between two non-equivalent easy axis of magnetization in-plane. The system will *reorient* its magnetization direction if the contributions to the energy (above discussed) change upon variation of e.g. temperature, thickness or strain.

In general, for films thicker than a few monoatomic layers, the magnetization is in-plane due to the shape anisotropy. However, in very thin films this may change due to the increasing importance of surface effects. As stated above, at surfaces, due to the broken symmetry, uniaxial anisotropy energies arise which, in general, are much higher than in the bulk [31]. These anisotropy energies may favor a perpendicular orientation of magnetization [32]. In these films a reorientation of the spontaneous magnetization is observed either as a function of film thickness or as a function of temperature [27, 34–36]. An schematic of the typical MAE plot (at constant temperature) is shown in Fig. 1.3.

but reduces considerably the demagnetizing field and the overall magnetostatic contribution.

[17] This is the standard sign convention but it can be chosen arbitrarily

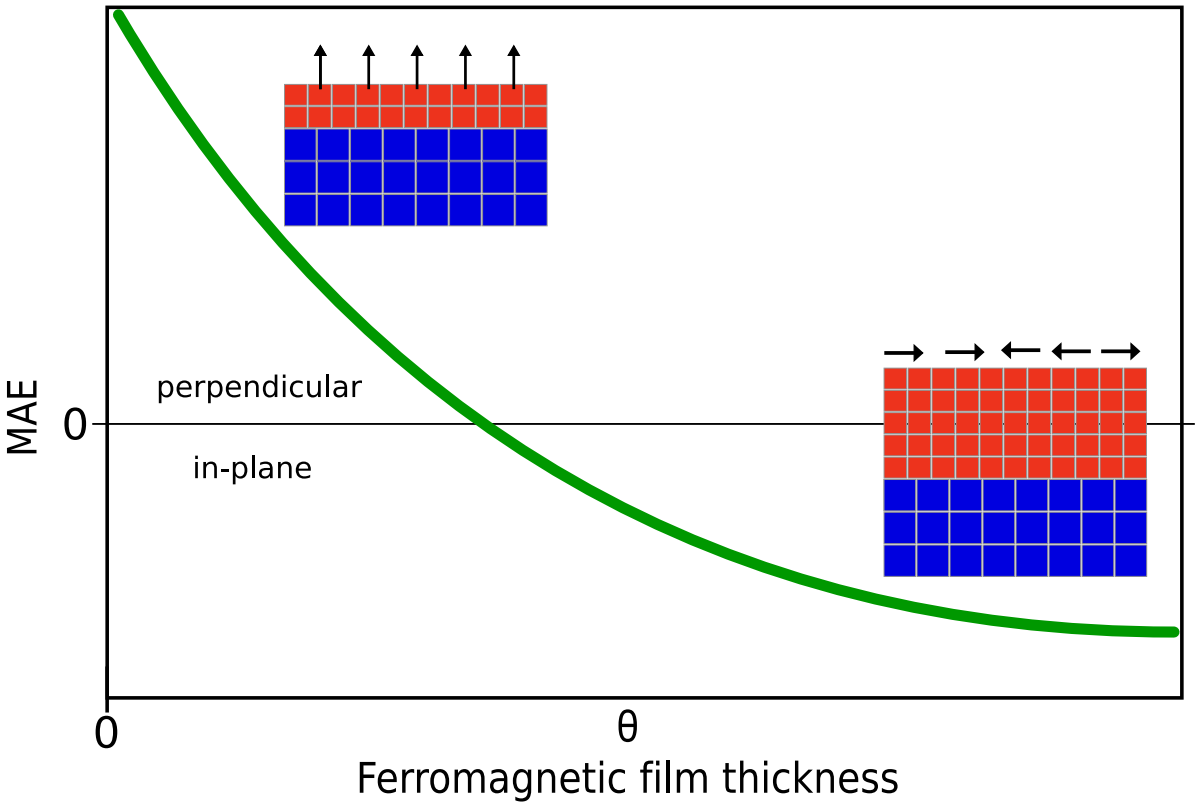

Figure 1.3: Diagram of the universal total MAE curve for thin ferromagnetic films. In the general case, ferromagnetic ultrathin films suffer a SRT from perpendicular to in-plane, as a function of thickness.

Chapter 2

Experimental Details

"There, sir! that is the perfection of vessels!"
— *20,000 Leagues Under the Sea*, Jules Verne, 1828–1905

This chapter describes the experimental techniques used in this work. We start with Low Energy Electron Microscopy (LEEM [2]). It is a powerful microscopy that has been used for almost every experiment presented in this thesis. The other microscopy technique used is an offspring of the LEEM, the Spin Polarized Low Energy Electron Microscopy (SPLEEM [3]). The LEEM is a relatively new microscopy technique capable of high-resolution (8 nm) and video-rate (30 fps) imaging of surfaces. The LEEM is also capable of measuring the diffraction pattern (LEEM-LEED) of micrometer sized areas. The SPLEEM is used to determine the magnetization direction of a ferromagnetic surface with high lateral resolution together with the topographical image of the region under observation. This allows to correlate locally the magnetic and structural properties.

2.1 LEEM

The LEEM, invented and developed by Ernst Bauer, is based on the reflection of a low-energy electron beam to image a surface in the real space. The wave length[1] of an electron beam with energy between 5 eV and 500 eV (LEEM typical electron energy

[1]The de Broglie wave length is: $\lambda = \sqrt{\frac{h^2}{2mE}}$, being m the mass and E the energy. For electrons, (energy in electron volts (eV) units and λ in Angstrom (Å)), it can be expressed: $\lambda_{e^-}[\text{Å}] = \sqrt{\frac{150.4}{E[\text{eV}]}}$.

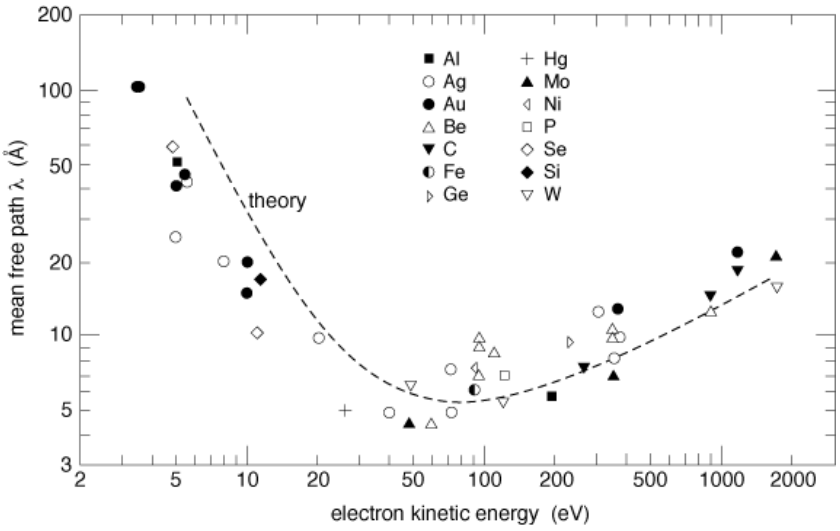

Figure 2.1: Mean free path of the electrons in solid. The dashed curve shows a calculation [37] of the mean free path independent of the material and the points are measured data [38, 39] from many elemental solids. The data points scatter more or less around the calculation. The curve is therefore often called a universal curve. The reason for this universality is that the inelastic scattering of electrons in this energy range mostly involves excitations of conduction electrons, which have more or less the same density in all elements. At lower energies other scattering mechanisms are important, like scattering with phonons. Taken from Zangwill [40].

range) is on the order of interatomic distances in solids ($\lambda_{5\text{eV}} \sim 5.5$ Å, $\lambda_{500\text{eV}} \sim 0.55$ Å). The universal mean free path curve for electrons, plotted in Fig. 2.1, shows that the LEEM energy range is optimum for surface studies due to the low penetration of its beam. Therefore, LEEM is very sensitive to the surface. Fig. 2.2 shows a schematic view of a LEEM set-up.

The idea is simple. Illuminate a region of a flat surface with an electron beam and get the reflected electrons to form a real space image. The first difficulty in the experimental set-up is to work with low-energy electron optics because of the large aberrations they produce. This problem is minimized by using 20 keV electron beam energies within the instrument and decelerating the beam very close to the sample. The sample thus sits within a strong electrostatic (up to 10 kV/mm for optimum resolution [41]) and magnetic[2] fields, and thus becomes one element of an immersion objective lens. After

[2]One of the two LEEM microscopes used in this thesis (the SPLEEM) has a completely electrostatic objective lens to allow the observation of magnetic samples without the interaction of magnetic stray fields.

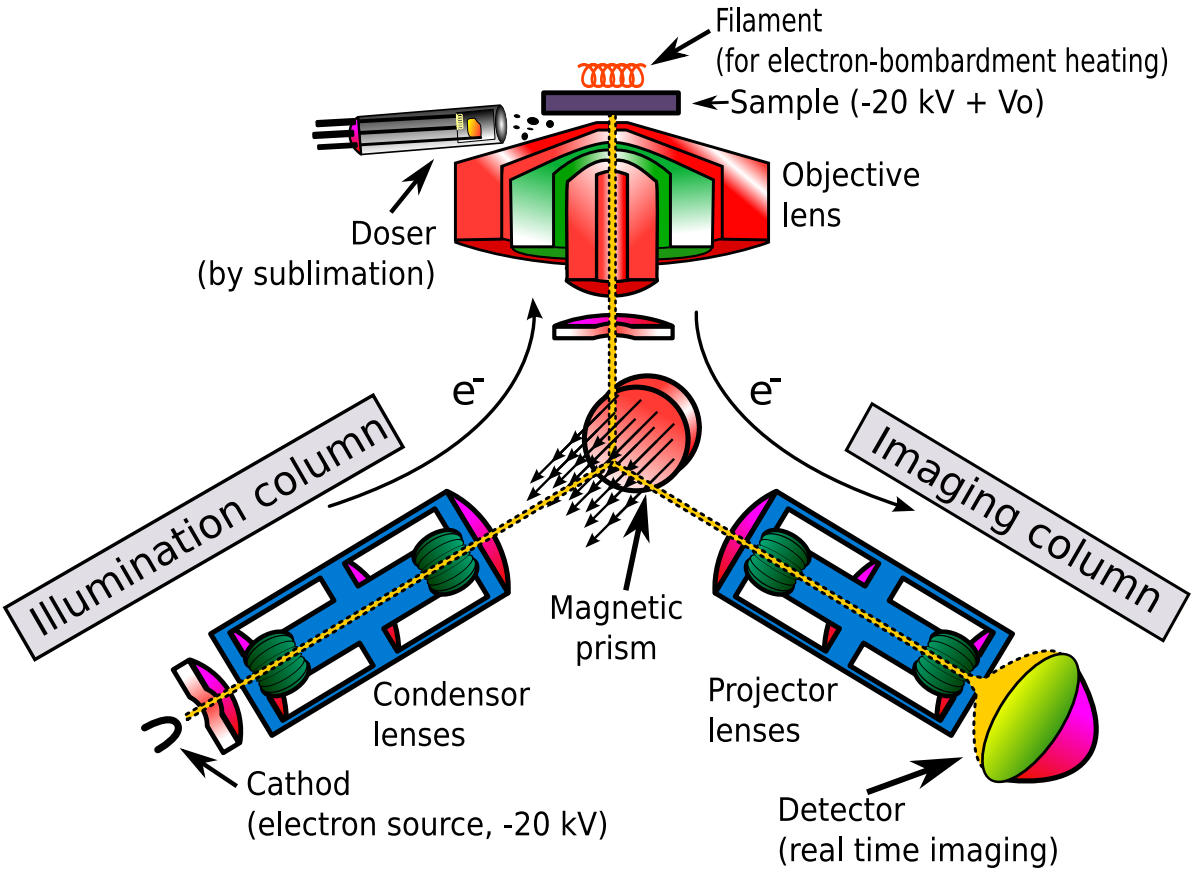

Figure 2.2: Schematic LEEM set-up. The electron beam, generated in the electron source, is directed to the magnetic prism through the illumination column, and from there it reaches the sample at normal incidence. The reflected beam goes again through the magnetic prism and is directed to the electron-detector and screen through the imaging column.

reflection, the electrons are accelerated again.

Another technical difficulty arises from the perpendicular incidence of the beam. This has two main consequences: (i) the LEEM can only measure very flat surfaces because the outgoing beam must also be perpendicular to go through the same objective lens and (ii) the incident and outgoing beams share the same path. For flat surfaces, the image contrast comes from variations in the local atomic arrangement or composition. However, strongly varying topography alters the accelerating field locally and is expected to produce focusing effects, complicating the analysis of images [42]. A manipulator with precision tilt control is used to adjust the sample tilt and get perpendicular incidence. The second issue is solved with the introduction of a magnetic prism in the beam trajectory which separates the incoming and the outgoing beams. This allows to use separate illumination and imaging columns (Fig. 2.2 and Fig. 2.3a).

LEEM systems can only work inside ultra high vacuum (UHV) chambers with pressures well below 10^{-8} torr (1 torr $\equiv$ 133.28 Pa). Hight voltage electron lenses need UHV to avoid electric arcs between the elements. Also, as in many other surfaces science techniques, UHV is a way to maintain a surface clean for a reasonable period of time. The two systems used in this thesis are the LEEM at Sandia National Laboratories (California) (Fig. 2.3a), managed by Kevin F. McCarty and the LEEM (actually SPLEEM) at Berkeley National Laboratory (Fig. 2.3b), managed by Andreas K. Schmid. Although its popularity has increased year by year, at the time this thesis is being written there are around 30 LEEM systems and only 3 working SPLEEM systems in the world.

Here we will introduce the most important features of LEEM. In the literature there are numerous references about LEEM basics [2, 41, 43–45], history [46], and experiments in which LEEM has played a crucial role [47–51].

2.1.1 LEEM elements

There are three parts in the microscope that we can treat separately, (i) the illumination column, (ii) the magnetic prism , (iii) the objective lens, and (iv) the image formation column.

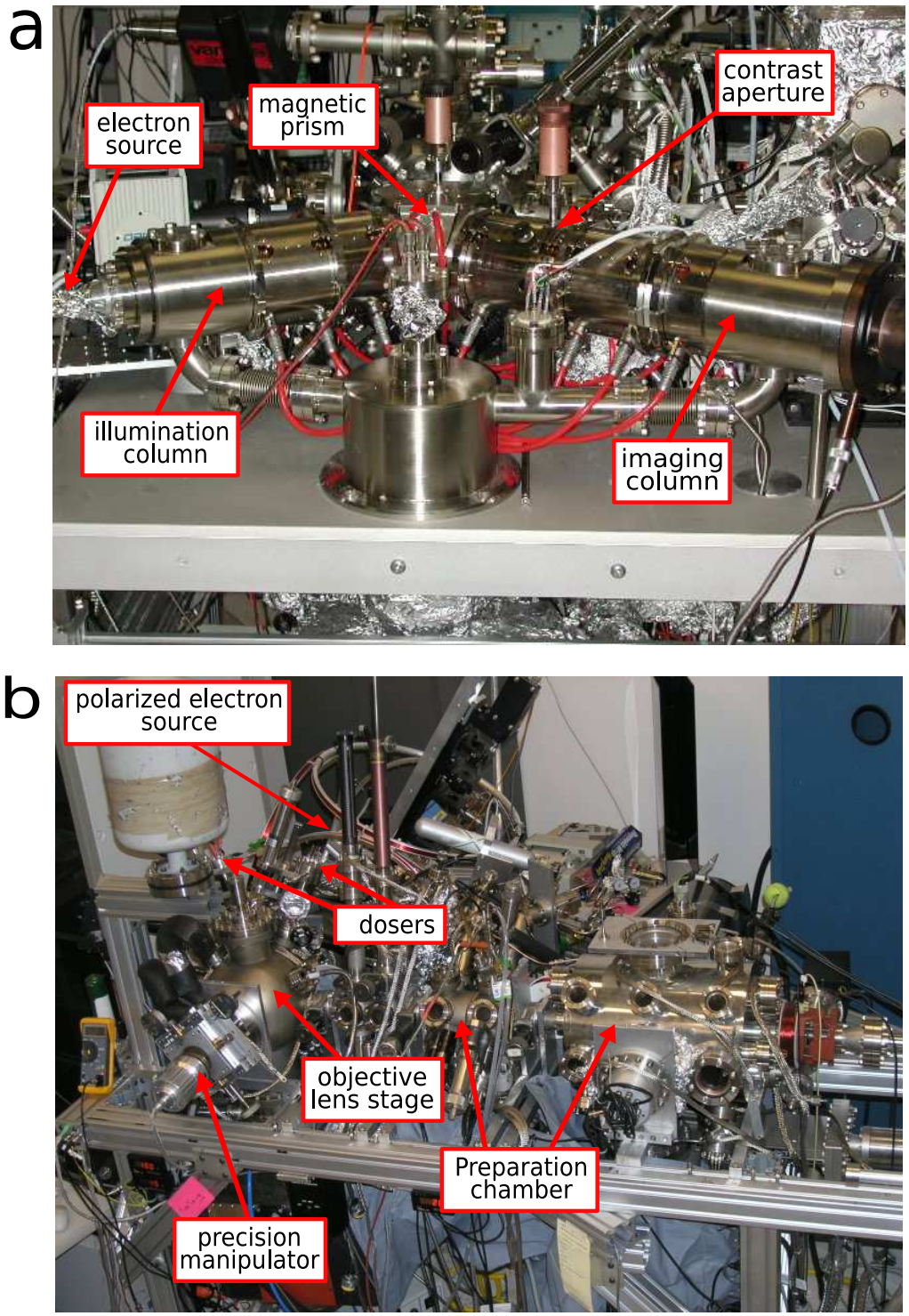

Figure 2.3: Pictures of LEEM set-ups. Both are variable temperature (100 K to 1700 K) and allows in-situ sample cleaning and thin-film deposition. a)Picture of the Sandia National Laboratories (SNL) LEEM set-up. b) Picture of the Berkeley National Laboratory SPLEEM set-up. It features an spin-polarized electron gun for magnetic studies.

Illumination column: formation of the electron beam

The electron source can vary from LEEM to LEEM. It can be a heated LaB_6 crystal, a field-emission source or, for polarized electrons, a GaAs photocathode (see section 2.2.2). The typical current of the beams generated is around 0.1-10 μA. The beam is focalized by the condensor lenses. The condensor lenses adjust the beam focus to the back focal plane of the objective lens, after the magnetic prism (Fig. 2.2).

The magnetic prism

The magnetic prism is the most complex lens in the system. The configuration introduced in 1991 [52] has become the standard beam separator for most of the LEEM instruments[3]. A magnetic prism consists of a magnetic field that bends the illumination beam onto the axis normal to the sample surface. The reflected electron beam, after the interaction with the surface[4], travels back along the same axis to reach the prism again, where it is deflected further, to enter the imaging column. In summary, the magnetic prism separates the incoming and reflected (image) beams. After the interaction with the sample, the beam contains information about image (real) and diffraction planes, and both must be faithfully transfered by the magnetic prism to the imaging column.

The objective lenses: real and reciprocal space

The LEEM (electron-) optics system is analogous to a visible-light optics system[5]. In both systems all the lenses simultaneously image the real space and, in the back focal plane, the reciprocal space (see Fig. 2.4). If the illuminated surface has long-range ordered regions, the beam will be reflected with different angle for each different ordered region, and with a common angle for the identically ordered regions. Constructive interference of the waves (light or electrons) is only fulfilled within certain angles where the Bragg condition is satisfied, which are, in general, different for every structure. The back focal plane[6] [54] of a lens *sorts* the rays by angle: the back focal plane shows the

[3]The early beam separators [53] consist of a uniform magnetic field over a circular region, with a strategically placed D-shaped cutout. Images obtained with the separator present image distortion due to unequal in-plane and out-of-plane magnifications [41].

[4]The illuminated surface area can vary from 3 μm to 100 μm.

[5]The main differences of an electron-optics system with respect to an optical system are that only convex lenses are possible and the quality of the lenses is much worse.

[6]In an ideal lens, all the incoming rays with the same angle will converge at one point of the back focal plane.

diffraction spots of those regions. We call this pattern, when is recorded by a LEEM, the LEEM-LEED pattern.

In certain LEEM instruments[7] the sample itself is at the same negative high voltage (∼15–20 kV) of the electron beam, plus a small (0-300 eV, in $\sim 0.2\ eV$ steps) difference, called start voltage (V_s). The electron beam reaches the sample with voltage V_s. Other possible design[8] implements a strong, homogeneous retarding field between the objective lens and the sample, which is at ground potential. In this case V_s is the final voltage of the electron beam after its deceleration. Cathode lenses have large chromatic and spherical aberrations, due to the strong electrostatic field that interfere with the beam used for the deceleration (and re-acceleration) of the electrons, that limits[9] the lateral resolution of the instrument to about 10 nm [55] in the absent of aberration corrections.

The projector lenses: imaging column

The first real space (slightly magnified, ∼20 times) image is formed at the magnetic prism, and then it is directed to the transfer lenses and finally to the projector lenses. Adjusting suitably the power of the transfer and projector lenses it is possible to image the real space (LEEM) or the diffraction pattern (LEEM-LEED). The last set of lenses magnifies the resulting image before the beam reaches the multichannel plates[10] and finally the phosphor screen. Behind the phosphor screen there is a CCD digital camera to record the images in real time.

2.1.2 LEEM contrast mechanisms

In the following a brief summary of the main LEEM contrast imaging modes and their advantages is given.

[7] Commercial ELMITEC Elektronenmikroskopie GmbH LEEM system at Sandia National Laboratories, Livermore, CA, USA.

[8] SPLEEM at National Center for Electron Microscopy, Berkeley, CA, USA.

[9] The aberrations of the magnetic prism separator have been demonstrated to be smaller than the cathode lenses aberrations, and to affect mainly to the quality of the transfer of the LEEM-LEED pattern, not the global resolution [43].

[10] Multichannel plates consist of an array of miniature electron multiplier channels ($\sim 10\ \mu m$ diameter, $\sim 15\ \mu m$ spacing between channels). These channels are parallel to each other and often enter the plate at a small angle to the surface. It intensifies the incident radiation or subatomic particles (electrons in our case) by the multiplication of electrons via secondary emission. This multiplication takes place in the small channels, under the presence of a strong electric field [56].

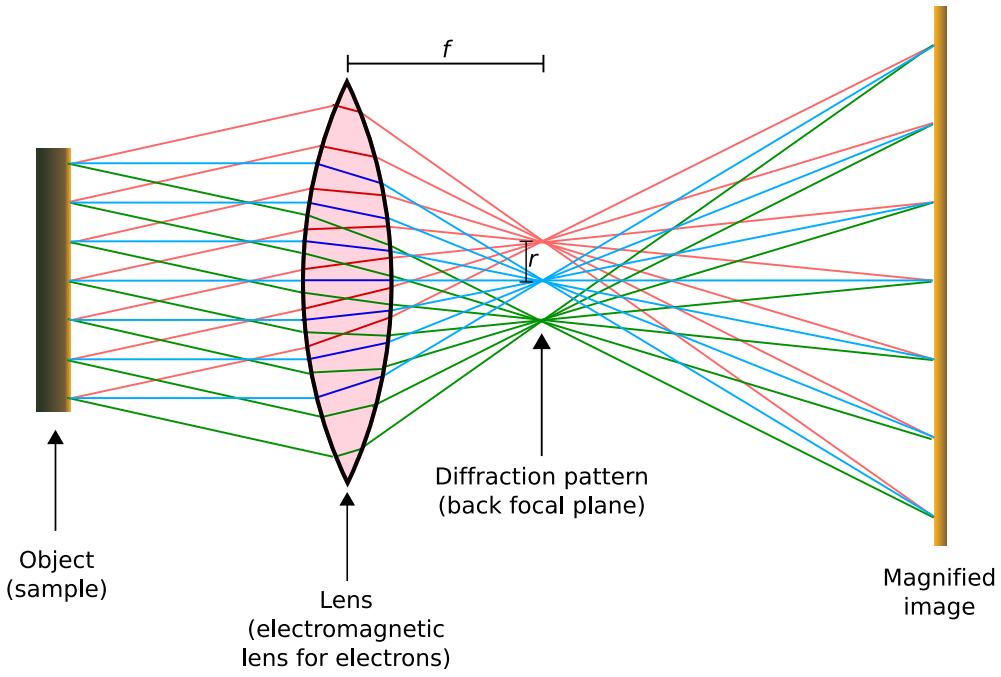

Figure 2.4: Ray diagram for a conventional (optical) lens. Rays with the same origin and different angle coincide in the magnified image. On the other hand, the rays with different origin but with the same angle coincide in the back focal plane.

Phase contrast

The contrast originating from the phase of the imaging electron wave is the standard contrast method for LEEM measurements. Every change in the electron beam phase will generate a change in the contrast. The phase contrast mechanism is used to characterize different regions of the surface based on its different thickness, structure, or composition. There is no easy way to predict the contrast change when one of this properties change, but it is useful to detect those changes.

The best known example of phase contrast is the step contrast that gives subatomic vertical resolution to the LEEM. It is possible to distinguish monoatomic steps with the LEEM (see Fig. 2.5). The wavelength of the electrons in the low energy regime ($\lambda_{5eV} \sim 5.5$ Å) appropriate for LEEM is on the order of the step height (∼2–6 Å). Hence, for perpendicular incidence, the electronic waves that hit the upper and lower part of the step will interfere and give a different contrast at the step (easily modified changing the electron energy). The electronic beam phase shift at the step has been modeled [57]: it predicts a Fresnel interference pattern at the step position similar to the one produced by an aperture (Fig. 2.6). The contrast at the steps observed with LEEM (see for example Fig. 2.5), present a much more simple interference pattern due to aberrations in the system lenses.

Quantum size effect (QSE) [59] contrast is another consequence of the phase contrast. QSE contrast uses the phase interference of the electrons reflected at the surface of a film and at the interface of the film with the substrate. It is very useful to reveal the thickness of ultra thin films, measuring energy scans[11] and studying the resulting oscillatory (Fabry-Perot interference type) brightness of the regions with different thickness and energy.

Mirror electron microscopy (MEM)

When the electrons have energies below the surface work function, all of them are reflected in front of the sample. The sample acts like an electron mirror and it is extremely sensitive to the sample tilt. The MEM mode can be used to adjust the tilt to get a perpendicularly incident and reflected beam and to measure the work function: in a surface with two structures (or materials) with different work function, it is possible to get MEM

[11] Changing the electron beam energy, typically from 5 eV to 30 eV, while recording LEEM images every 0.2 eV.

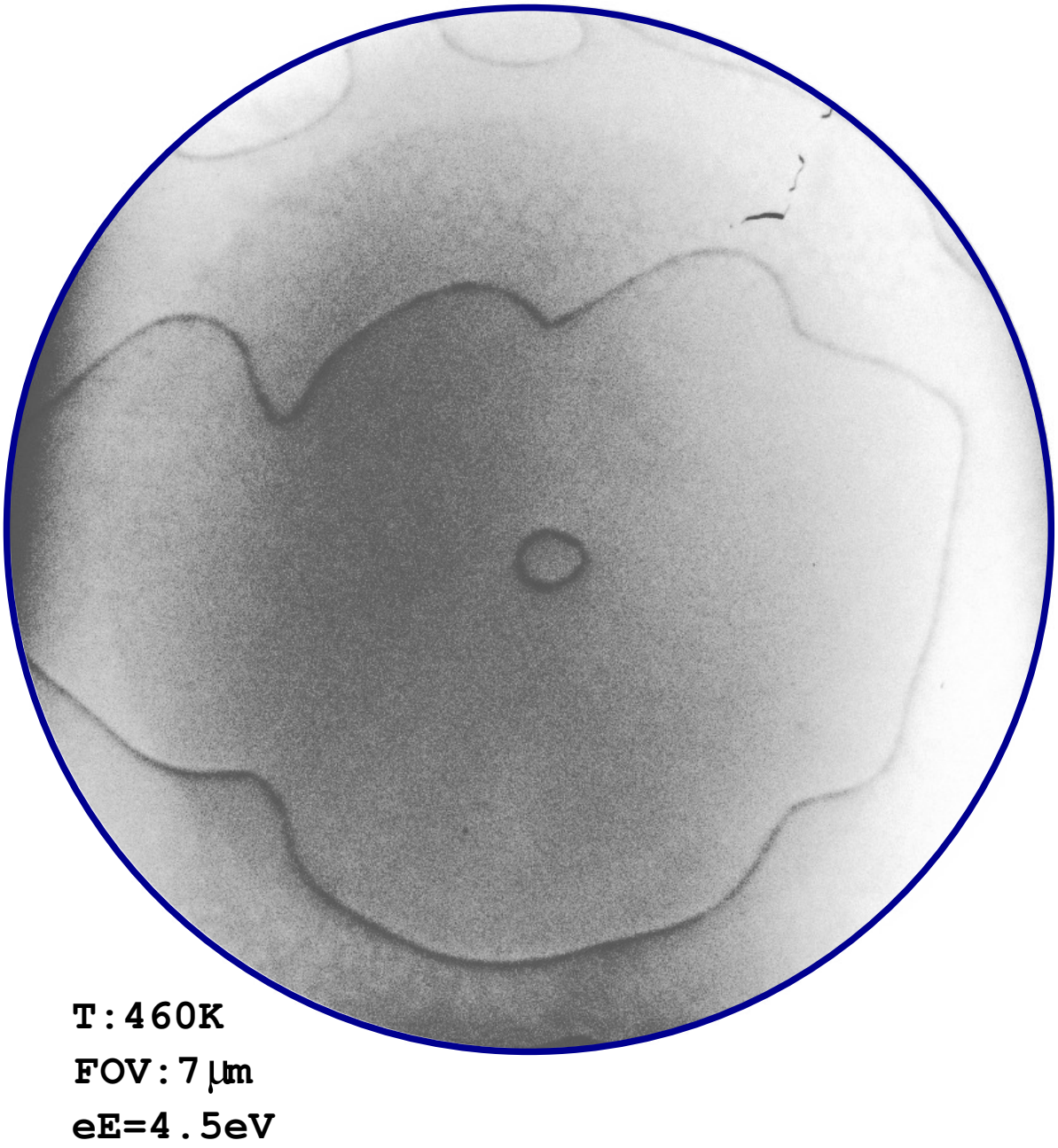

Figure 2.5: LEEM image of the clean surface of Ru(0001). The phase contrast makes possible to distinguish the Ru monoatomic steps (darker grey). The field of view (FOV) is 7 μm, and the electron beam energy eE (eE $\equiv V_s$) is 4.5 eV.

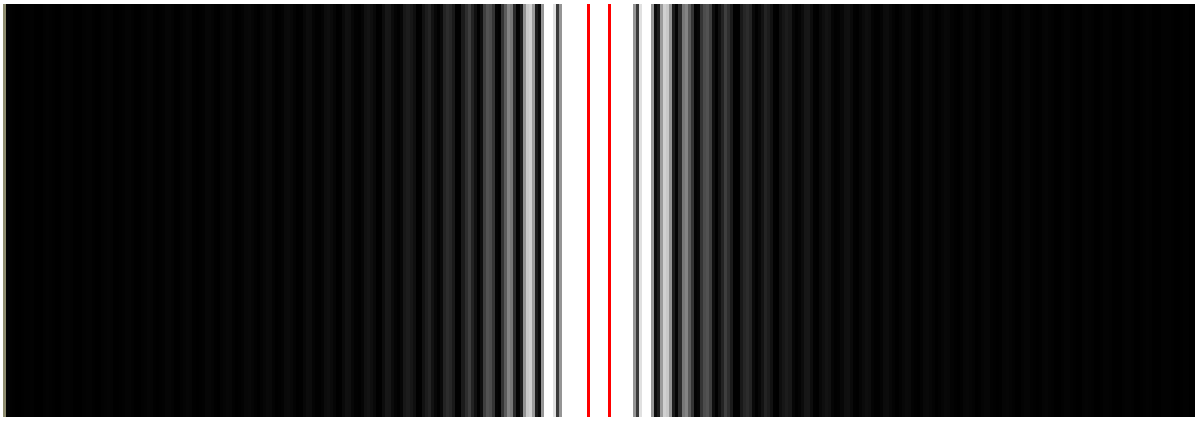

Figure 2.6: Calculated Fresnel interference pattern [58]. In this example, white and black regions are produced by the shadows cast by a small aperture (red lines, 1 mm width) when using a plane source of monochromatic light as a light source.

contrast: if the beam energy is below the work function of one of them and above of the other, the electrons will be reflected in front of one region and partly penetrate the other, giving brighter and darker regions, respectively.

The field distribution above the surface causes a smearing of the contrast which effectively reduces the resolution, compared to that of the phase contrast.

LEEM-LEED: μLEED and other improvements

As explained above, it is possible to image the diffraction pattern with a LEEM, adjusting the transfer and imaging lenses. The LEEM pattern formation is quite different from a conventional LEED diffractometer, in which the screen is curved and there is an energy selector/filter.

The first obvious difference is that the spots on the LEEM-LEED do not move towards the center [43] when the beam energy increases, in contrast to the conventional LEED. This can be seen from the diffraction condition:

$$\sin \alpha_0 = \lambda_0 \mathbf{G} \tag{2.1}$$

where α_0 is the scattering angle from the sample normal, λ_0 the wave length and $\mathbf{G}$ a surface reciprocal vector. After being reflected by the surface the electrons are accelerated to 20 keV. The new angle α and electron wave length λ are related by the Snell's law:

$$\frac{\sin\alpha_0}{\lambda_0} = \frac{\sin\alpha}{\lambda} \tag{2.2}$$

The combination of these two equations gives:

$$\sin\alpha = \lambda\mathbf{G} \tag{2.3}$$

Hence, the position of the reciprocal space spots, from equation 2.3 and Fig. 2.4, is given by

$$r = f\tan\alpha \tag{2.4}$$

where r is the position of the diffraction spot relative to the center of the back focal plane and f is the focal length. Therefore, the reciprocal spot position r is independent of λ_0 and of initial the beam energy ($E = 1/\lambda_0^2$). Spots that do not move simplify the process of recording intensity versus energy (I-V) curves.

Another advantage is that, since the illumination and the imaging column are separated by the magnetic prism, nothing blocks the specular spot. LEEM-LEED also allows to arbitrarily magnify every spot. This is very convenient to study in detail satellite spots of large unit cell surfaces. The fact that there is no optical straight path from the sample to the phosphor screen makes it possible to measure the diffraction pattern during sample heating, as no light from the sample surface reaches the screen.

There are several disadvantages: (i) there is usually no energy filter and, therefore, we will always obtain a secondary-electron diffuse spot in the background of the LEEM-LEED image (see upper-left region close to specular spot in Fig. 2.7c and Fig. 2.9a). (ii) There is no way to normalize the intensity of the spots with the incident beam intensity.

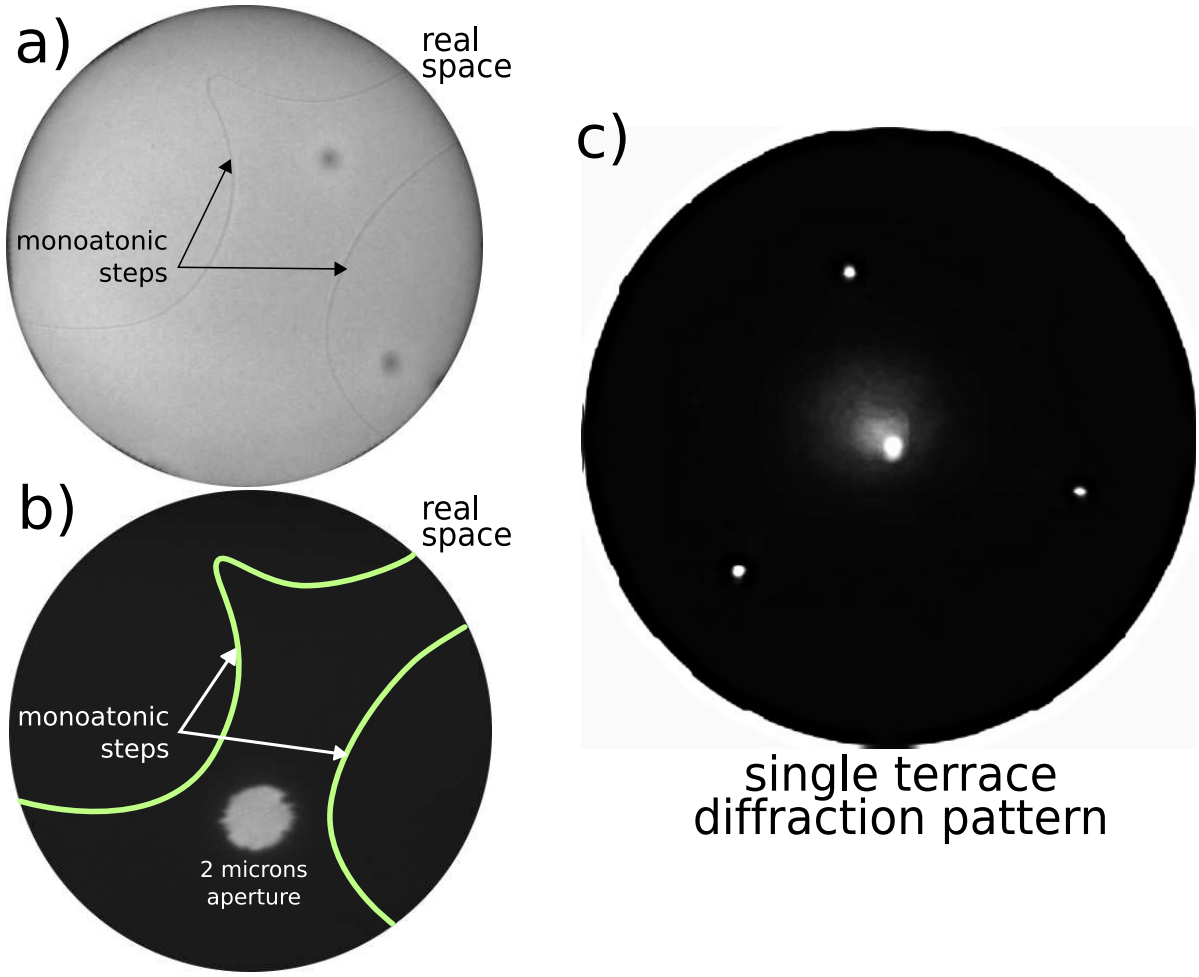

Figure 2.7: μLEED imaging procedure. a) LEEM image of the clean Ru(0001) surface. The field of view is 15 μm, and the electron energy is 2.5 eV. The arrows mark the position of two atomic steps present in the field of view. The two monoatomic steps are visible due to phase contrast. b) LEEM image of the same area where a small aperture limits the electron beam to a 2.1 μm diameter region on a single terrace. The steps are framed to indicate that the aperture region is step-free. c) The diffraction pattern (LEEM-LEED pattern) formed from this selected area by changing the power of the imaging lenses.

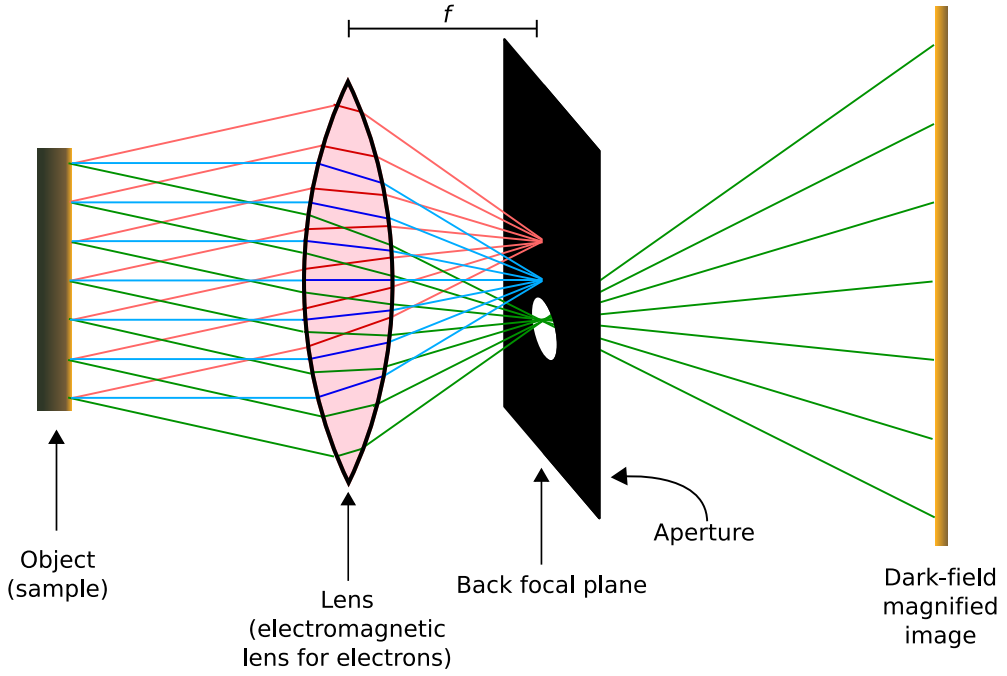

Figure 2.8: Ray diagram for a conventional lens with a contrast aperture placed in the back focal plane. Only the rays that generate the selected spot can form the final image (green rays). All the other rays will be blocked by the aperture. In a LEEM system the aperture is located at the imaging column, close to the magnetic prism.

(iii) The LEEM-LEED patterns are distorted by the electron optics in far-off-axis regions.

It is possible to place an aperture into the illuminating beam to select a small region[12] of the surface[13], and image the diffraction pattern of that region. This mode is called μLEED (see Fig. 2.7). It can be used to, for example, measure the structure of a certain region of the real space which we can be sure, looking with the LEEM, that it is defect free or that it has a uniform thickness. It is a clean way to avoid the lateral averaging inherent on the LEED diffractometers.

LEEM also allows to place an aperture in the imaging column (contrast aperture)

[12] An aperture is a metallic plate with a hole. There are different aperture sizes, all of them circularly shaped. The smallest can select an area at the surface of $\sim$2 μm diameter.

[13] It is also possible to change the size of the electron beam by focussing it. The smallest illuminated region can be $\sim$3μm FOV. However, an aperture can choose a more uniformly illuminated area (for example at the center of a bigger FOV), and can be easily chosen just moving the aperture itself.

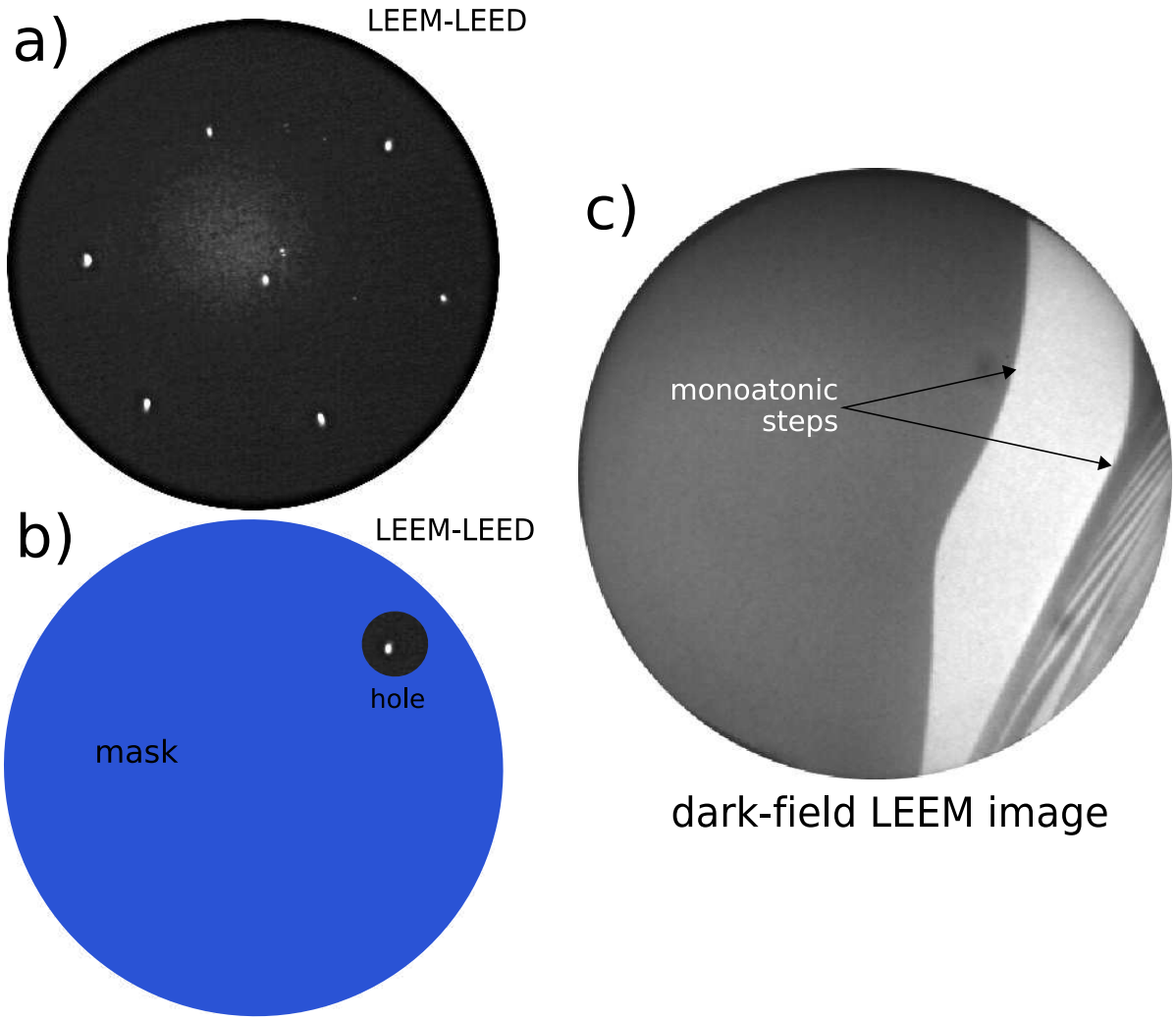

Figure 2.9: a) LEEM-LEED pattern of a clean Ru(0001) surface, averaging over several steps. The perfect (step-free) Ru(0001) surface exhibits three-fold ($p3m$) symmetry. Thus, diffraction from a single terrace should give a 3-fold pattern. However, most diffraction techniques show six-fold symmetry ($p6$) in the corresponding diffraction pattern [60, 61], like in this figure. This apparent change in symmetry results from the different stacking on neighbor terraces, with termination ...BABA and ...ABAB respectively (where A and B indicate the two possible stacking positions of the hcp crystal.) b) We select one of the spots of the six-fold pattern shown in a) by means of a contrast aperture (Fig. 2.8). The selected spot belongs to one of the two three-fold patterns averaged (see the three-fold pattern obtained using μLEED for the same surface in Fig. 2.7). Then the selected spot is the product of the electrons reflected by one of every two consecutive terraces. c) Dark-field real-space image of the clean Ru(0001) surface. Only one of every two consecutive terraces appear bright.

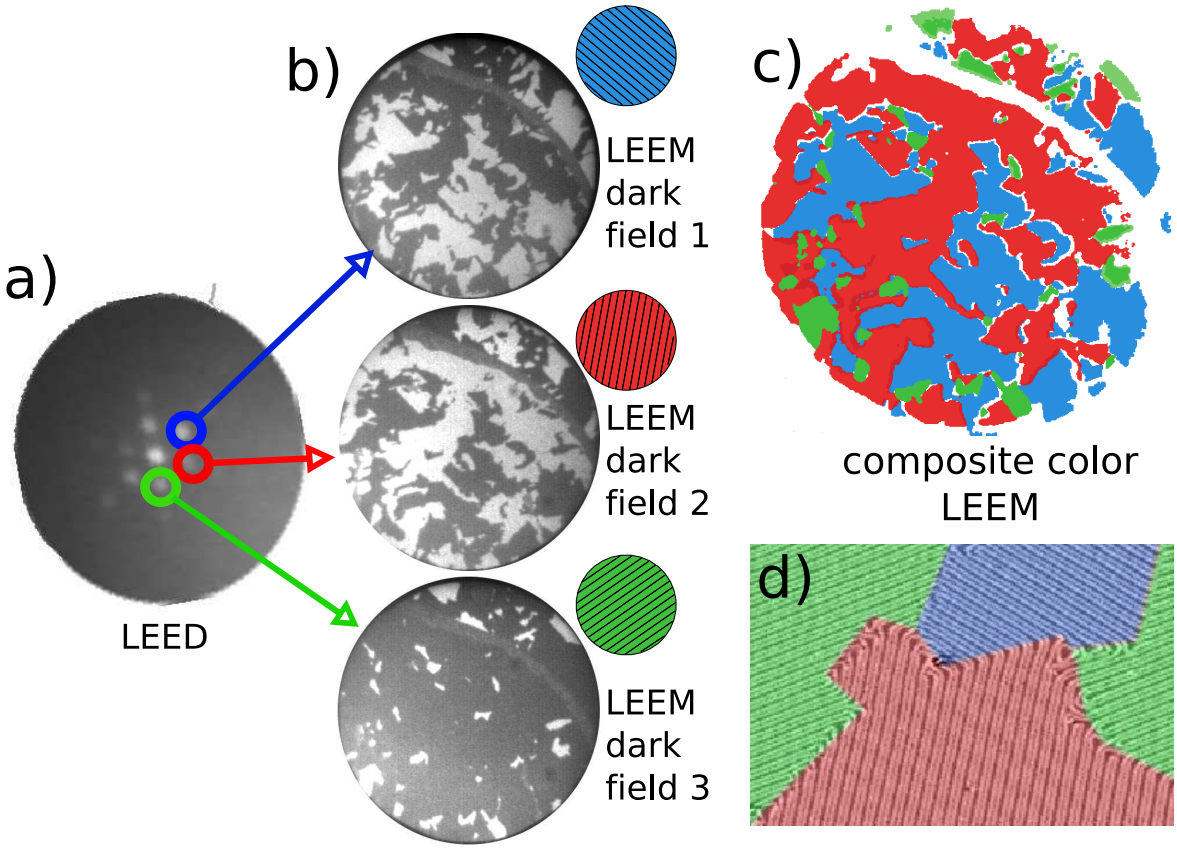

Figure 2.10: Dark-field LEEM study on 2 ML Cu/Ru(0001). Clean Cu films two atomic layers thick on Ru(0001) relax the difference in lattice parameters with the substrate along close-packed directions by the introduction of extra planes of atoms in the film relative to the substrate, with three equivalent orientations, forming three different rotational domains. a) LEED pattern around the specular beam showing satellite spots due to the film orientation relative to the substrate. Each selected spot can be used in turn to make a dark-field image showing, in b), the corresponding rotational domain. FOV = 5 μm. The lines in the red, green and blue circles mark the unique in-plane directions that distinguish the different rotational domains deduced from the diffraction pattern. c) Composite color image obtained from the superposition of the three dark-field images of b), where the colors indicate the orientation of each rotational domain. The areas that are not shown in any color correspond to 3-ML Cu. d) STM image of the surface of a 2 ML copper film on Ru(0001), showing a detailed view of the rotational domains. The rotational domains have been colored for comparison with the other panels. The image is 278 nm wide. For further details see Ref. [51].

to select one spot of the diffraction pattern (Fig. 2.8), opening the door to two well known contrast methods widely used in transmission electron microscopy: The bright- and dark-field imaging modes.

Bright-field imaging mode

Even when the projector lenses are adjusted to image the real space, the diffraction pattern is formed inside the LEEM. It is possible to place an aperture (metallic plate with a hole) in order to block all the diffraction spots but the specular beam. The real image will be formed only with the intensity information of the specular beam spot. The contrast will depend, then, on the kinetic energy of the reflected electrons, responsible of the specular beam spot intensity. This mode is called bright-field imaging in Transmission Electron Microscopy (TEM) [62].

Dark-field imaging mode

If, in the same conditions, we place the contrast aperture on a diffraction spot[14] different from the specular beam the image mode obtained is called dark-field imaging [62] (see Fig. 2.9 and Fig. 2.10). This mode is extremely useful as it gives information about structure domains in the sample. In dark field mode, the real space image will have brightness *only* in the ordered regions of the surface where the structure forms the selected diffraction spot. This has been used by the author and his group to map the three rotational equivalent domains of misfit dislocations of the surface of 2 monolayers of Cu/Ru(0001) with the LEEM [51]. The dislocation structure present on the film has a periodicity smaller than the LEEM resolution and would be impossible to resolve only with LEEM real-space imaging (Fig. 2.10).

2.2 SPLEEM

Spin-polarized low energy electron microscopy (SPLEEM) is an extension of the LEEM: SPLEEM is LEEM with spin-polarized electrons as illumination.

In addition to the regular LEEM contrast and imaging modes[15], the SPLEEM pro-

[14] It is also possible to move the diffraction spot to the aperture position.

[15] The SPLEEM used in this work, located at the NCEM, (LBNL, Berkeley, USA) is not adequate

vide us with magnetic contrast of ferromagnetic surfaces. The interaction of the spin-polarized electrons with the ferromagnetic surface layers depends upon the relative orientation of the spin polarization of the electron beam **P** and the local magnetization **M** in the surface layers of the sample, i.e. upon the spin-dependent exchange scattering. The reflected electrons, *whose polarization is not measured*, are used to form the image exactly in the same way as in a regular LEEM (see section 2.1.1). The fast image acquisition and the non lateral-averaging magnetism imaging makes the SPLEEM an excellent complement to other magnetic methods [55].

2.2.1 SPLEEM basics

Magnetic contrast of SPLEEM is based upon the exchange scattering interaction. The exchange energy term (E_{ex}) of the incident electrons with spin $\mathbf{s}_{\mathrm{i}}$ and the sample surface electron spins $\mathbf{s}_{\mathrm{j}}$ at their positions $\mathbf{r}_{\mathrm{i}}$ and $\mathbf{r}_{\mathrm{j}}$ can be written as:

$$E_{\mathrm{ex}} = \sum_{ij} J(\mathbf{r}_i - \mathbf{r}_j)\mathbf{s}_i \cdot \mathbf{s}_j \tag{2.5}$$

where J is the exchange coupling constant. In regions with preferred spin alignment directions, i.e. in magnetic domains (see section 1.2.1) of ferromagnetic samples, there will exist a net magnetization $\mathbf{M} \propto \sum_j \mathbf{s}_j$. If the electron beam has a mean polarization $\mathbf{P} \propto \sum_i \mathbf{s}_i$, the magnetic contrast contribution will be proportional to $\mathbf{P} \cdot \mathbf{M}$ [3].

The polarization of the incident beam (P_0) is ∼20-25 %[16]. The exchange interaction magnetic contrast in a spin-polarized LEEM image is only a small fraction of the structural contrast [55]. To enhance the magnetic contrast of the SPLEEM images and to remove all the topographic non-magnetic contrast, two images are recorded with opposite incident polarizations and then subtracted [2]. Since the topographic contrast is independent of P and the magnetic contrast is proportional to $\mathrm{P} \cdot \mathrm{M}$ the resulting image will have only magnetic contrast. The magnetic signal (or scattering asymmetry) is obtained from the normalized intensity difference [55]:

$$A = \frac{I^{\uparrow} - I^{\downarrow}}{I^{\uparrow} + I^{\downarrow}} \tag{2.6}$$

where $I^{\uparrow}$ and $I^{\downarrow}$ are the reflected intensities for oppositely polarized incident electron

for LEEM-LEED acquisition.

[16]For the GaAs electron source of the SPLEEM used in this work (section 2.2.2).

beams. The division by the spin-up and spin-down image sum yields an asymmetry image in which intensities are proportional to the sample magnetization. An example of how an SPLEEM image is generated can be seen in Fig. 2.11. This procedure can be repeated for three orthogonal alignments of the spin polarization of the electron beam, to obtain image-triplets reflecting the 3D components of the magnetization vector field of the samples [63].

The magnetic contrast will depend on the electron energy. The band structure of single crystals plays an important role on this dependence [64]. When the electron energy is increased from zero (theoretically 100% reflectivity) to the onset of the spin-up band in the spin-split asymmetry, the reflectivity of the spin-up electrons suddenly decreases, while the spin-down electrons are still 100% reflected until the onset of the spin-down band is reached. If we increase the electron energy, the magnetic contrast A will be weaker but still nonzero because of the slightly different density of states at a given energy. Quantum size effects also plays an important role in thin films: the reflectivity will oscillate with electron energy because the interference condition is fulfilled for different energies for spin-up and spin-down electrons. Since it is no trivial to find a priori the electron energy for the maximum contrast, it is always necessary to measure it experimentally.

While LEEM works at video rates, SPLEEM needs around half a second to gather enough electrons to yield a detectable magnetic contrast in the image. Hence the acquisition rate of the SPLEEM is $\sim$1 s. The image integration and subtraction processes makes the images noisier than the LEEM ones. The final SPLEEM resolution decreases to $\sim$20 nm.

2.2.2 SPLEEM elements

In this section we will briefly review the two main differences between LEEM and SPLEEM set-ups: the spin-polarized electron source and the spin manipulator. Fig. 2.12 shows a schematic view of the NCEM SPLEEM set-up. In depth details of the instrumentation and operation of SPLEEM have been described elsewhere [3, 55, 65, 66].

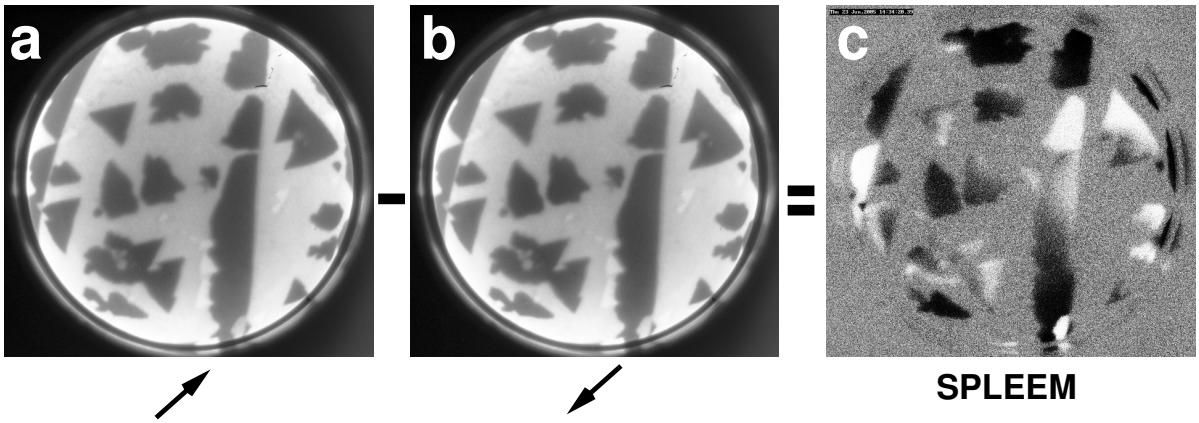

Figure 2.11: Method for obtaining an SPLEEM image. A spin-polarized electron beam is used to illuminate the sample surface, and a pair of LEEM images of the same sample region is acquired [a) and b)]. The direction of the spin-polarization of the electron beam is rotated by 180 degrees between the two images [black arrows below a) and b) indicate beam polarization directions]. When a pixel-by-pixel difference image is formed from the images a) and b) all structural image contrast vanishes except for the contrast which is due to the sample magnetization. Normalizing this difference image results in the grey-scale image c), where bright (dark) contrast reveals the strength of the component of the local magnetization direction parallel (antiparallel) to the direction of the spin-polarization used in panel a). (Field of view in the images is 2.8 μm and the electron energy is 7 eV).

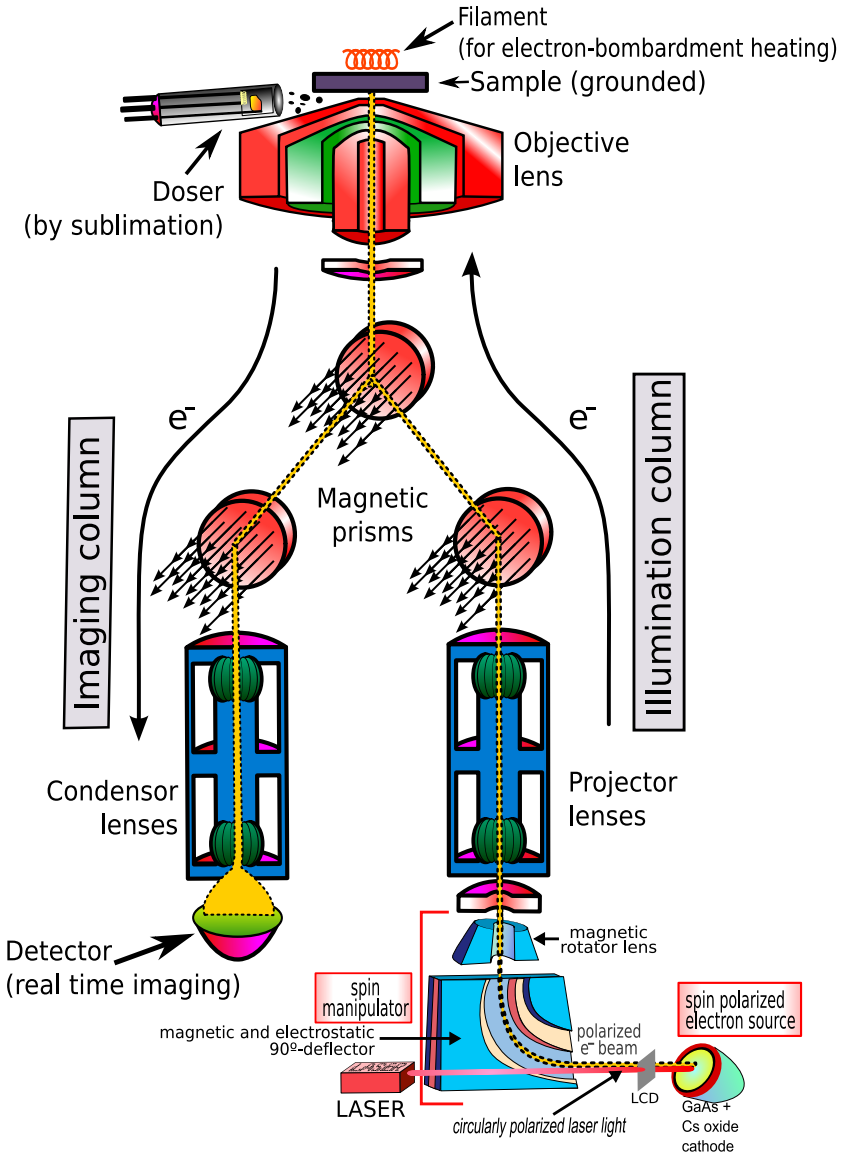

Figure 2.12: Schematic SPLEEM set-up. The polarized electron beam is generated at the GaAs photocathode. The spin manipulator (see Fig. 2.13 for more details) selects the desired spin polarization direction. After the spin manipulator, the beam is directed to the deflection stage through the illumination column. There, the electronic beam passes through two magnetic prisms and from there it reaches the sample. The reflected beam goes again through the deflection stage and is directed to the electron-detector (multi channel plates) and to the screen.

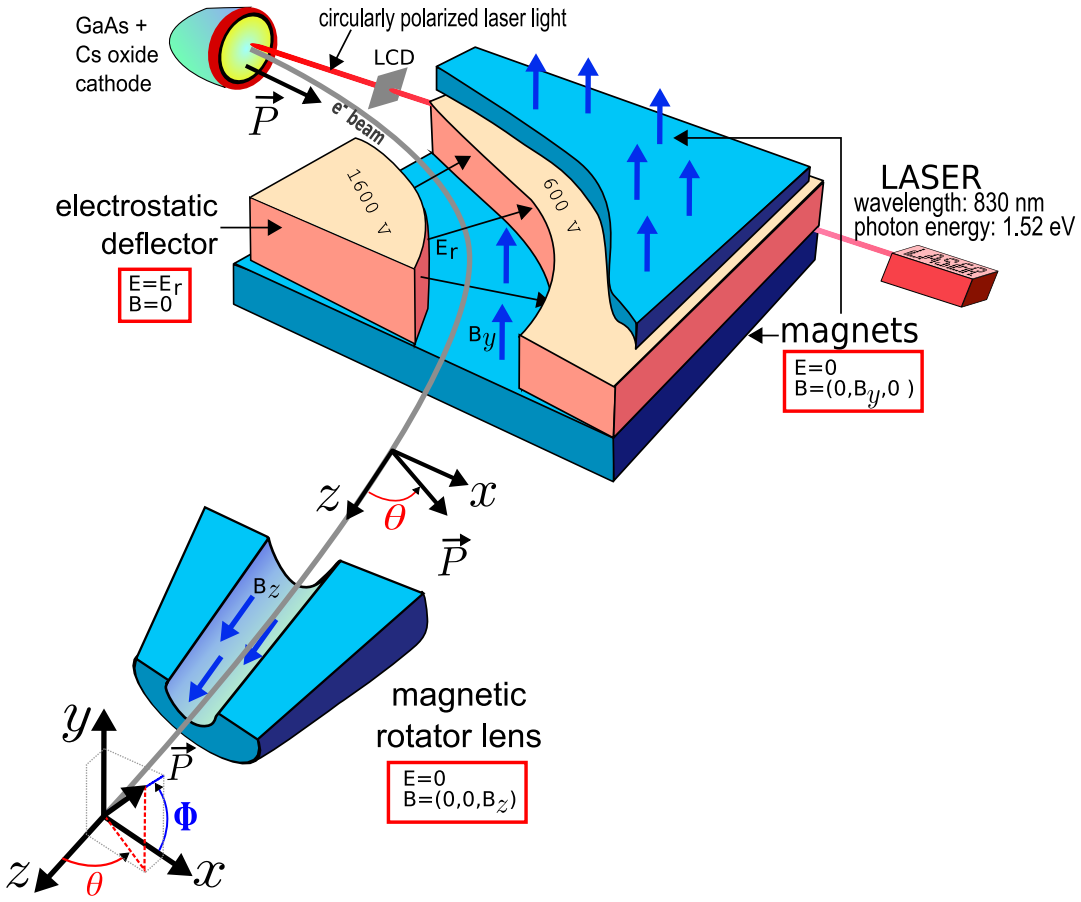

Figure 2.13: Cartoon of a spin manipulator arrangement. The GaAs photocathode is illuminated by a circularly polarized laser light. The electronic photoemitted beam leaves the cathode with polarization in the same direction of the incident circularly-polarized laser light (perpendicular to the surface). The 90°-deflector, composed of the electrostatic deflector (that produces the radial electric field E_r) and magnetic deflector (that produces the magnetic field B_y), can switch the spin polarization direction of the electron beam from perpendicular ($\theta = 0°$) to in plane ($\theta = 90°$), and to all the angles in-between (i.e. within the z-x plane). After the 90° deflector, the magnetic rotator lens change the in-plane angle Φ of the spin-polarized beam with a longitudinal magnetic field (B_z). The spin manipulator is able of changing the beam polarization direction in to every desired direction. (Based on the schematic from Ref. [65]).

Spin-polarized electron source

A GaAs[17] photoemission cathode is the spin-polarized electron source used in SPLEEMs. When GaAs is illuminated with circularly-polarized laser light[18] with energies slightly larger than its bandgap, electrons are excited from the spin-split levels at the top of the valence band ($p^{1/2}$ and $p^{3/2}$). The conduction band is unequally populated with the two spins states [67]. In normal conditions, the conduction electrons cannot escape from the crystal. One cesium oxide layer [68] plus one oxygen layer deposited on the surface of the GaAs cathode (in UHV conditions) enhances the electronic photoemission by lowering the vacuum level below the minimum of the bulk conduction band [69], i.e. the surface achieves negative electron affinity [68]. As a result, the photo-emitted electrons can leave the surface when the cathode is illuminated with a circularly polarized laser light (perpendicular to the surface in the SPLEEM set-up). The outgoing electrons are polarized in the illumination direction. The sense of the circularly polarized light (clockwise or anticlockwise) determines the final sense of the electron spin polarization (perpendicular pointing to the GaAs crystal or perpendicular pointing to the vacuum). Switch between both polarizations is done by means of an liquid crystal. This method is routinely used in the measurement of SPLEEM images, since two images with opposite beam polarization are needed to form every SPLEEM image (see Fig. 2.11). The percentage of polarized electrons in the beam (P_0) is ∼20-25 %(see footnote 16).

Spin manipulator

The schematic arrangement of a typical spin manipulator is shown in Fig. 2.13. A 90°-deflector can change the polarization direction of the newly-generated and perpendicularly-polarized electron beam from perpendicular to in-plane. By superposition of the electric and the magnetic deflection fields, any orientation of P between $0° \leq \theta \leq 90°$ within the (x, z) plane can be obtained. After the 90°-deflector, the rotator magnetic lens with its longitudinal magnetic field causes a precession of the transverse component of P around the beam axis. The combination of the electrostatic and magnetic deflectors and the rotator lens allows to orient the polarization direction of the beam in any direction. We usually measure three orthogonal directions (one perpendicular to the surface and two in-plane separated 90°) to completely resolve the surface magnetization direction.

[17]The GaAs crystal is a direct gap semiconductor with a minimum band separation of 1.42eV at room temperature near the center of the Brillouin zone.

[18]Diode laser with a wavelength of 830 nm and photon energy of ≈1.52eV.

2.3 Using the LEEM and the SPLEEM

Both LEEM and SPLEEM are complex microscopes. Their operation is far from being automated and requires the knowledge of most of their parts and permanent attention from the scientist. In this work we present measurements in two different microscopes, one LEEM and one SPLEEM. The operation of both instruments is briefly described in the following sections.

2.3.1 Using the SNL LEEM

The LEEM used is located at Sandia National Laboratories (SNL), Livermore, California (USA). It is a commercial LEEM system named Elmitec III[19]. The LEEM UHV chamber (Fig. 2.3a) is composed of two parts, the main chamber and the preparation chamber. The preparation chamber can expose the sample to gases like O_2 to clean it and has a fast entry system to introduce new samples without breaking the UHV. There is also a parking section to store several samples mounted in their sample-holders. It also has an Auger electron spectrometer (AES). A transfer bar is used to move the samples from the preparation to the main chamber, and vice versa.

The main chamber houses the LEEM, which is composed of three columns separated by 120°, due to the LEEM design (like the schematic view of Fig. 2.2). For aligning the sample relative to the incident electron beam, the sample is mounted on a precision manipulator with two independent tilt axes. Further optimization of the substrate/electron-beam alignment was performed by adjusting the microscope lenses so that the equivalent diffraction beams appeared/disappeared at the same electron energy (i.e., the Ewald sphere was centered).

The SNL LEEM has a lateral spatial resolution of 10 nm and uses a heated LaB_6 crystal as an electron source. It allows in-situ sample heating (up to 1300 K) and cooling (down to 100 K). The sample heating is carried out by electron bombardment by means of a filament directly mounted in the sample holder (see Fig. 2.14), while the cooling is carried out by an inefficient liquid nitrogen circuit that cools down the rear of the sample holder down to ∼200 K. The SNL LEEM allows to introduce gases and to grow materials by molecular beam epitaxy (MBE) over the samples (see Fig. 2.2) while recording images at up to video rate. In this set-up we have deposited Co and

[19]By ELMITEC Elektronenmikroskopie GmbH.

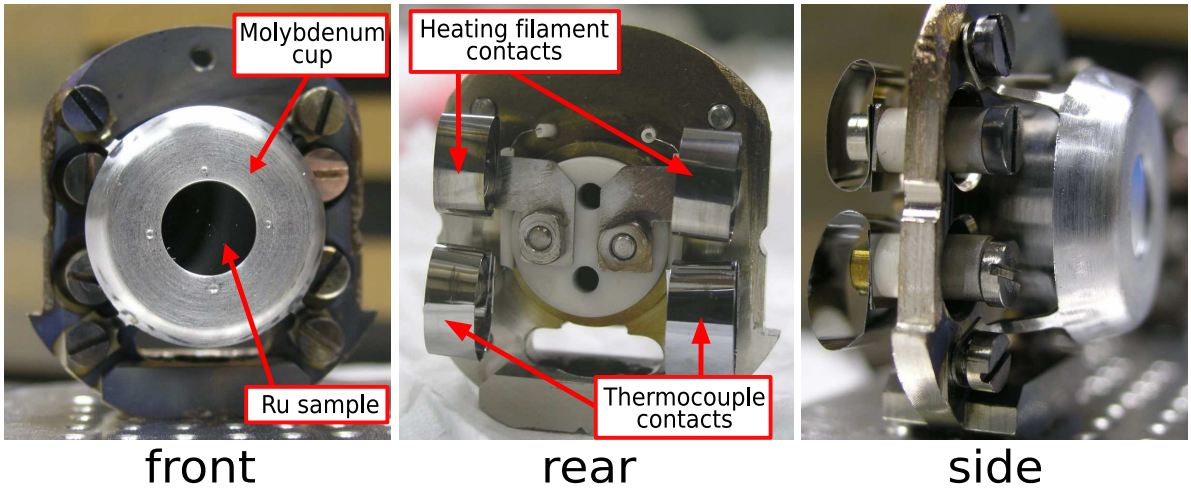

Figure 2.14: Pictures of the Elmitec sample holder, used by the LEEM and the SPLEEM. The sample holder allows to heat the sample by electron bombardment of the rear of the sample by means of a filament directly mounted in the sample holder. It also allows to precisely measure the sample temperature by means of a tungsten/rhenium alloy (W-5%Re vs. W-26%Re) thermocouple. The whole sample holder is transported between main and preparation chambers with the help of a transfer bar.

Cu on a Ru(0001) sample. The evaporators consist of a high purity rod (Co) or a W crucible (Cu), which is brought to sublimation temperature by electron beam heating inside a water-cooled cap. The evaporators are calibrated with the LEEM, following in real time the growth. The sample holder used is an Elmitec design (see Fig. 2.14) that, in addition to the heating filament, incorporates a thermocouple to measure the sample temperature in-situ. The background pressure in the main chamber is 1×10^{-10} torr.

The LEEM is operated by changing the current of the different magnetic lenses with a control computer. After the alignment of the sample tilt, the different lenses allow us to focus the surface, to zoom in and out, and to switch from the real space (LEEM) to the diffraction pattern (LEEM-LEED). Changing the voltage of the sample (SV) it is possible to choose the final electron beam energy[20]. The experimental set-up allows to place illumination and contrast apertures to measure in bright- and dark-field modes, as well as in μLEED mode. The video-rate acquisition system consists of a Peltier-cooled CCD camera whose output is digitized by a commercial digital video system at 30 frames of 720×480 8-bit pixels per second.

[20]Because the sample is part of the immersion objective lens.

2.3.2 Using the NCEM SPLEEM

The other LEEM instrument used is the SPLEEM located at the National Center for Electron Microscopy (NCEM), at Lawrence Berkeley National Laboratory (LBNL), Berkeley, California (USA). This unique experimental set-up (Fig. 2.3b) is one of the three SPLEEMs working nowadays in the world. This system, in contrast with the SNL LEEM, is an *user facility*, and hence open to external scientific proposals.

The NCEM SPLEEM electron source is a laser-light illuminated GaAs (section 2.2.2). The actual composition of the optimized cathode is: GaAs substrate + one monolayer of CsO + one monolayer of O_2. To maximize the electron emission of the source it is necessary to renew the cathode every three days. The process has two steps: (i) clean the GaAs surface (i.e. remove the CsO and the O_2) by flashing it by means of electron bombardment heating up to ∼800 K, and (ii) grow the CsO and cover it with O_2. The optimized emission must be $\geq$5 μA.

The NCEM UHV chamber is also divided into preparation and main chambers. One important difference with the 120°-design SNL LEEM resides in the magnetic prism. The NCEM SPLEEM has one magnetic prism to separate the incoming and outgoing beams, and two additional magnets to reorient the illumination and the imaging columns from being separated 120° to be parallel (see Fig. 2.12). The three magnets allows a single-column design. The SPLEEM is also able of changing the sample temperature in-situ between 100 and 2000 K. All the cathode objective lens are fully electrostatic. One benefit of electrostatic lens over a magnetic lens is that it causes no magnetic stray fields in the sample region, which allows us to image remanent domain structure in vanishing external field [70]. A magnetic objective lens would also rotate the polarization of the electrons. The SPLEEM microscope resides in a μ-metal shielding to prevent disturbances of the electron beam by the earth's magnetic field and by other external electromagnetic radiation sources. The pressure in the main chamber is always below 3×10^{-11} torr.

The NCEM SPLEEM is operated by changing the voltage of electrostatic lenses and the current trough the magnetic lenses and prisms with a control computer. Magnetic elements have hysteresis and must be changed with care: when we change the power of an magnetic lens, it is not possible to reproduce the previous configuration because the lens dynamics is governed by an hysteresis cycle. The only way trying to undo changes (if the configuration got worse) is to change the power of other lenses.

The sample holder (see Fig. 2.14) and the evaporators used are the same for the SNL LEEM and the NCEM SPLEEM. The output image is digitized by a commercial digital camera at 2 frames of 950×911 8-bit pixels per second. The regular LEEM data is recorded at up to 15 frames per second of the same resolution and 16-bit pixels.

Chapter 3

Ruthenium (0001): Surface Crystallography and Morphology

"No problem is too small or too trivial if we can really do something about it."
— *Letter to Koichi Mano*, Richard Feynman, 1918–1988

Ruthenium has attracted interest for its catalytic properties [71]. While a perfect hcp (0001) surface has three-fold symmetry, the diffraction patterns commonly obtained from the Ru(0001) surface are six-fold symmetric. This apparent change in symmetry occurs because on a stepped surface, the atomic layers on adjacent terraces are rotated by 180 degrees. Here we use a Low-Energy Electron Microscope (LEEM) to acquire the three-fold diffraction pattern (LEEM-LEED) from a single hcp Ru terrace and measure the intensity-vs-energy curves for several diffracted beams. By means of multiple scattering calculations (see section §A-i) fitted to the experimental data with a Pendry R-factor [72] of 0.077, we find that the surface is contracted by 3.5($\pm$0.9)% at 456 K. The Ru(0001) is the substrate used for all the thin films studied in this thesis.

3.1 Preparation and Cleaning of Ru(0001)

The Ru(0001) substrate was cleaned in-situ by repeated cycles of exposure to oxygen followed by heating to 1800 K. To further remove carbon a special procedure was followed. The sample was kept at 900 K until C islands started to appear on the crystal

surface. When the islands covered most of the surface, the sample, under observation in the LEEM, was exposed to 4×10^{-8} torr of O_2. The O_2 exposure was continued for a few minutes until the islands were removed. The sample was heated to 1300 K, and the procedure was repeated. After several cycles, the sample could be kept at 900 K for longer than 15 minutes without carbon reappearing.

3.2 Ru(0001): Surface Crystallography

The clean hcp Ru(0001) surface does not reconstruct. However, like most unreconstructed metal surfaces, the topmost layer of atoms relaxes inward towards the second layer. Both early LEED studies [73] and more recent ones [74] reported that the first interplanar spacing, d_1, was contracted by 2% relative to the bulk. However, *ab-initio* calculations by Feibelman [74, 75] and Xu *et al.* [76] found a much larger relaxation, between 3.5–4%. This experiment/theory disagreement prompted suggestions that the smaller experimental relaxation may result from hydrogen adsorption [74], although this possibility was disputed by others [60]. In a subsequent surface x-ray diffraction (SXRD) study, Baddorf *et al.* [77] found a somewhat larger interplanar spacing and only small changes in d_1 upon H adsorption. Given this history, the Ru(0001) surface serves as a model system to test the accuracy of both experimental techniques and *ab-initio* calculations.

As Fig. 3.1 illustrates, the perfect (step-free) Ru(0001) surface exhibits three-fold (*p3m*) symmetry. Thus, diffraction from a single terrace should give a 3-fold pattern. However, most diffraction techniques show six-fold symmetry (*p6*) in the corresponding diffraction pattern [61, 78]. This apparent change in symmetry results from the different stacking on neighbor terraces, with termination ...BABA and ...ABAB respectively (where A and B indicate the two possible stacking positions of the hcp crystal). As Fig. 3.1 also shows the surface terminations of adjacent terraces are rotated by 180° with respect to each other; therefore, diffraction from adjacent terraces yield 3-fold patterns that are rotated 180° with respect to each other. Thus, averaging over several terraces results in the commonly-observed six-fold symmetry.

In this thesis we revisit this surface to address the discrepancy between theory and experiment described above. We use the fine spatial resolution of low-energy electron microscopy (LEEM) [2, 41, 43] (see section 2.1) to obtain a new set of I-V curves from a single terrace on the Ru(0001) substrate. In contrast, in traditional LEED measure-

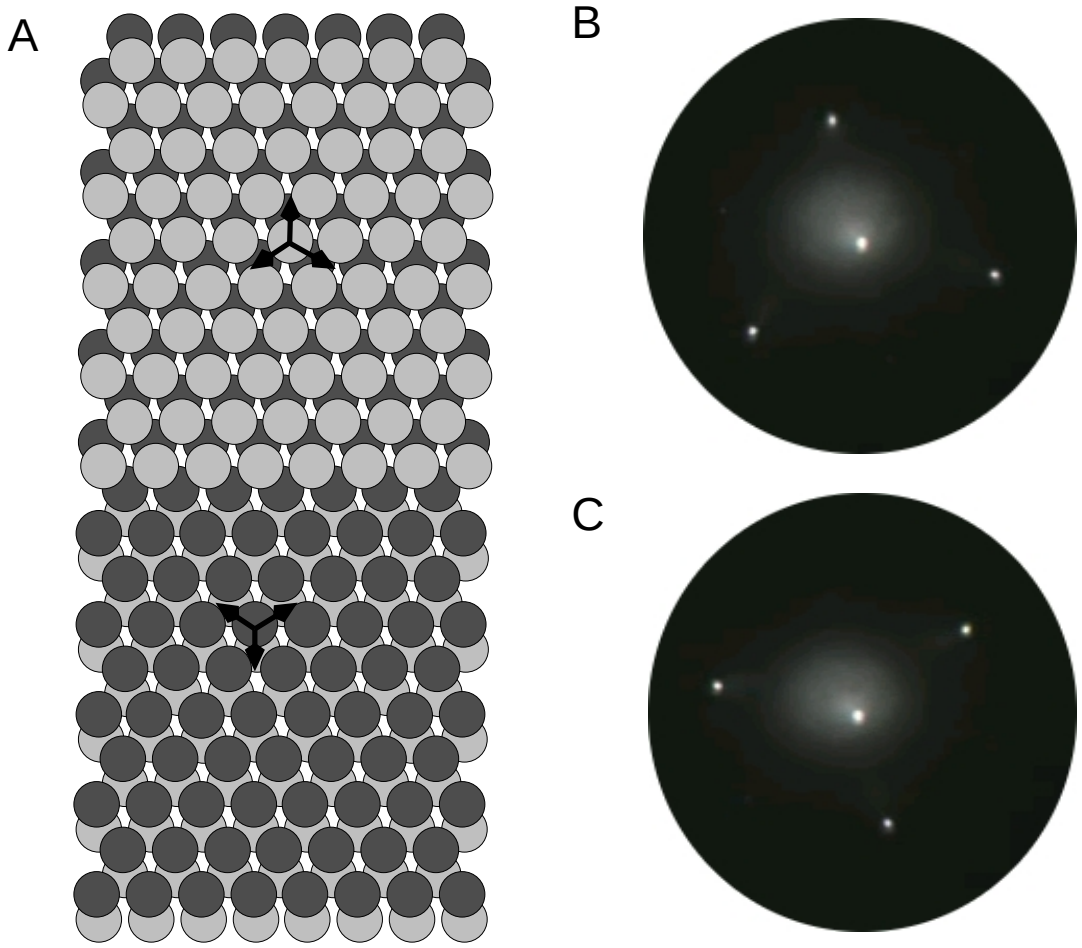

Figure 3.1: a) Schematic illustration of two adjacent terraces on the Ru hcp surface separated by an atomic step. The arrows point from a surface atom to its three closest neighbors in the layer below. Across adjacent terraces, the arrows are rotated by 180°. b)-c) LEED patterns at 32 eV acquired from two adjacent terraces showing the three-fold symmetry of the surface and the rotation upon crossing a monoatomic step. The observed spots correspond to the specular and the integer (10) beams.

ments, the electron beam illuminates large areas comprising many terraces. Obviously, avoiding symmetry averaging should enhance the reliability of the I-V analysis. Indeed, our best-fit structure gives a first interplanar spacing, d_1, that is in excellent agreement with theoretical predictions within the carefully determined experimental errors.

3.2.1 LEEM experiment details

A major advantage of LEEM is the ability to image a surface and then obtain diffraction information from selected and well-characterized areas [2, 41, 43] (see section 2.1.2). This capability is illustrated in Fig. 3.2. Two curved monoatomic steps, which appear dark because of a phase-contrast mechanism [2, 57], are observed within the field of view of the left image. An area about two microns wide is selectively illuminated by inserting a smaller aperture into the illumination beam (right image). By changing the power of the imaging lenses, the diffraction pattern from this small area is obtained (Fig. 3.1). Since this region contains only a single terrace (no steps), the LEED pattern is three-fold symmetric (Fig. 3.1b). The LEED pattern obtained from a region on an adjacent terrace is rotated by 180° (Fig. 3.1c), consistent with the change in stacking between adjacent layers in an hcp crystal. Another way to show the symmetry change when crossing substrate steps is to use an aperture [2] to selectively form an image from a non-specular diffraction spot [51]. In this dark-field imaging mode, only areas that diffract electrons into the selected spot are imaged bright in the real-space image. Thus, in an image (see Fig. 3.3) formed from an integer diffraction spot, adjacent terraces are alternately bright and dark. This dark-field contrast is similar to the one reported for würtize (0001) surfaces [79].

For diffraction measurements, a LEEM apparatus has several advantages over a conventional electron diffractometer as shown in section 2.1.2. The electron path is well shielded from external magnetic fields, making very low-energy measurements possible (VLEED [80]). Since there is no direct optical line of sight from sample to the detection screen, high-temperature measurements are straightforward. The LEEM geometry, where incoming and outgoing electrons are separated by a magnetic prism, allows measurement of the specularly reflected beam (i.e., the (00) beam) at normal incidence. The magnification of the LEED pattern can also be adjusted. Furthermore the spots do not move when the beam energy is changed. Unlike in conventional diffractometers, most current LEEM instruments do not perform energy filtering. Thus, secondary electrons are imaged together with the elastically scattered electrons. However, the sec-

ondary electrons can be easily removed by image processing because their contribution is spread out over a large area in reciprocal space, as described below.

The intensities of the (00), (01), (10) and (11) beams were obtained simultaneously by recording a sequence of images while changing the electron energy. The crystal was maintained at 456 K. To use the full dynamic range of the detection system and maximize the signal-to-noise ratio, the beam-energy range of 1 to 353 eV was split into three ranges (1-70 eV, 60-133 eV and 115-353 eV). Within each range, the electron current was adjusted to nearly saturate the image collection system at the most intense conditions. The different sections of the I-V curves were then rescaled with the same scaling factor for all the beams, by matching the intensity of overlapping scan regions. A plane was fit to the intensity of a box around the diffraction spot. This plane, which contains the secondary electron contribution, was then subtracted from the box. This procedure gives the same results as subtracting the average intensity along the box's perimeter, except where secondary electrons impose a large gradient on the background. The three (10) and (01) beams, as well as the six (11) beams, which are symmetry equivalent [81], where averaged together. Given that the (10) and (01) beams are not equivalent, we measured a total energy range of 1109 eV. The experimental I-V curves are shown in Fig. 3.4.

3.2.2 Results and discussion

The experimental I-V curves are shown in Fig. 3.4a. As is obvious from the data, the (01) and (10) beams are not equivalent. The best fit to the experimental data, shown on the same figure, was found for $d_1 = 2.065 \pm 0.02$ Å and $d_2 = 2.14 \pm 0.025$ Å. With respect to the room temperature bulk value, $d_b = 2.141$ Å, these interplanar spacings give relaxations of $\delta d_1 = -3.5(0.9)\%$ and $\delta d_2 = 0.0(1)\%$ (where the number in parenthesis indicates the error in percentage of the bulk value). The dependence of R_P on d_1 is presented in Fig. 3.4b. The agreement between the experimental and simulated I-V curves is excellent, as reflected by an R_P minimum value of $R_{P,min} = 0.077$. The interplanar spacing of the topmost two layers for the optimized structure is in excellent agreement with the *ab-initio* calculations. That is, we find that $\delta d_1 = -3.5(0.9)\%$ while theory finds 3.5-4% [74, 76]. However, our structure differs somewhat from the previous experimental structures, which found $\delta d_1 = -2\%$ [60, 73, 74] and $\delta d_1 = -2.4(0.4)\%$ [77].

We report results at 456 K. We investigated potential effects of this somewhat elevated temperature in two ways. First, we acquired a complete, independent I-V data

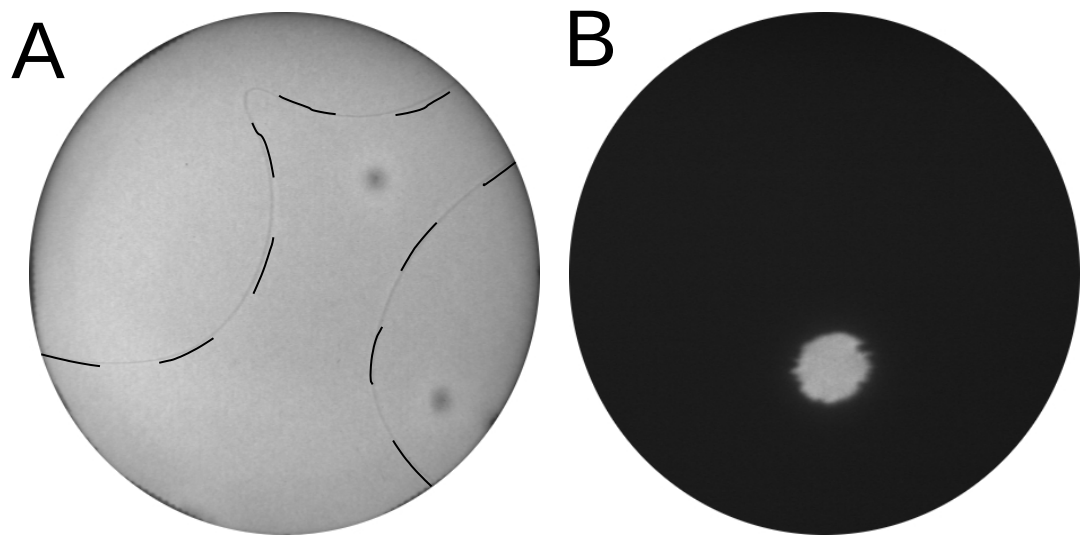

Figure 3.2: a) LEEM image of the Ru surface. The field of view is 15 μm, and the electron energy is 2.5 eV. The black dashed lines mark the two atomic steps present in the field of view (detected as faint grey lines). b) LEEM image of the same area where a small aperture limits the electron beam to a 2.1 μm diameter region on a single terrace. A diffraction pattern is formed from this selected area by changing the power of the microscope lenses.

set at room temperature. Analysis of this data (Fig. 3.5) produced the same structure as the best-fit structure at 456 K (Fig. 3.4 and Table 3.1). Therefore, we can safely rule out that the temperature plays any significant role on the first interlayer spacing contraction. Second, we optimized the bulk-Ru lattice constant in the R-factor analysis of the 456 K data. The minimum R_p occurred at the room-temperature Ru lattice constant (within $\pm 0.2\%$) and, again, the error bars were nearly the same as the analysis without this additional parameter. Thus, we conclude that the first interlayer spacing of Ru is contracted by 3.5% both at room temperature and at 456 K.

Experimentally we optimized the LEEM lenses by means of the sample tilt. In order to check any possible off-normal misalignment, we have performed another R-factor analysis considering off-normal incident angles (Θ) in the IV calculation. Fig. 3.6 left shows R_{Pendry} vs. Theta projected for d_1 and d_2 (as before, this graph corresponds to the best R_{Pendry} for a given Theta changing d_1 and d_2). The R-factor presents a clear minimum at normal incidence. Fig. 3.6 right, on the other hand, shows R_{Pendry} vs. d_1 projected for d_2 and Θ. Again, the optimized d_1 value is not changed. This analysis corroborates that the value of the d_1 contraction is not an artifact arising from any

Figure 3.3: Dark-field image of the Ru(0001) surface. The field of view is 15 μm. The electron energy is 40 eV. An aperture blocks all the diffracted electrons except those corresponding to one of the first-order diffraction spots: only areas that diffract electrons into the selected spot are imaged bright. Thus, the image intensity alternates between bright and dark when monoatomic steps are crossed.

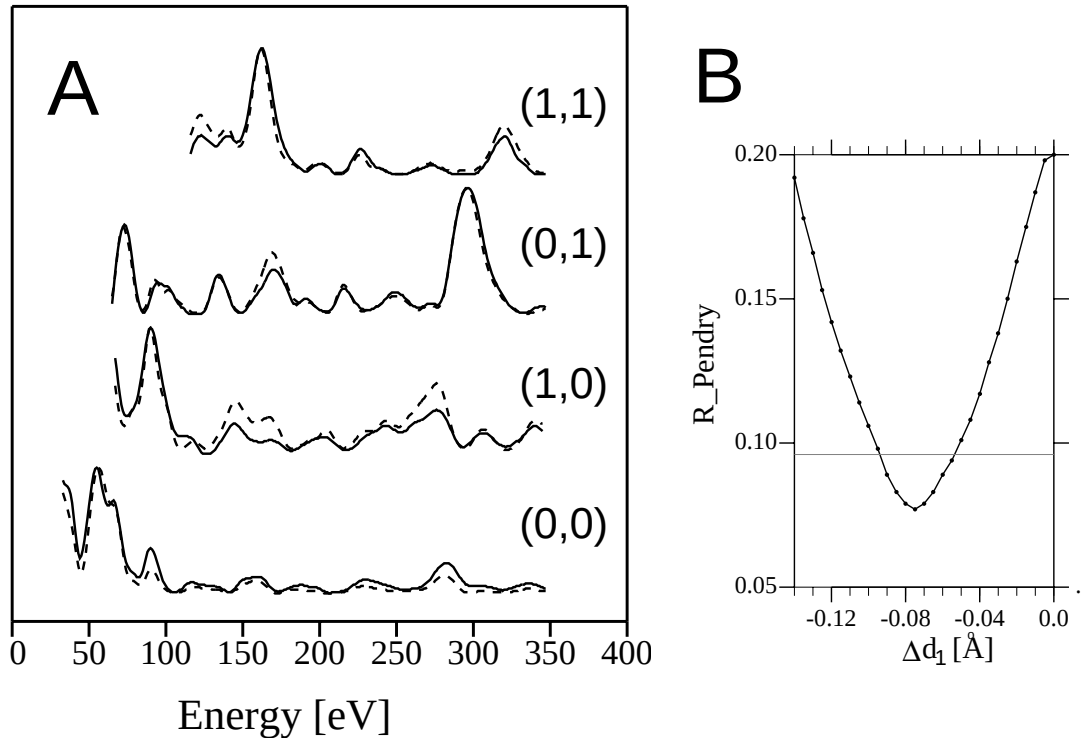

Figure 3.4: LEED data acquired at 456 K. a) Comparison between experimental (solid lines) and calculated (dashed lines) I-V curves for the Ru(0001) surface. The total incident-beam energies spans a range of 1109 eV. b) R_P vs. first interlayer spacing, d_1. For each fixed d_1 value in the graph, R_P has been minimized as a function of d_2, thus taking correlation effects into account. Gray horizontal line gives the R-factor variance, ΔR_P, from which the error bars are estimated.

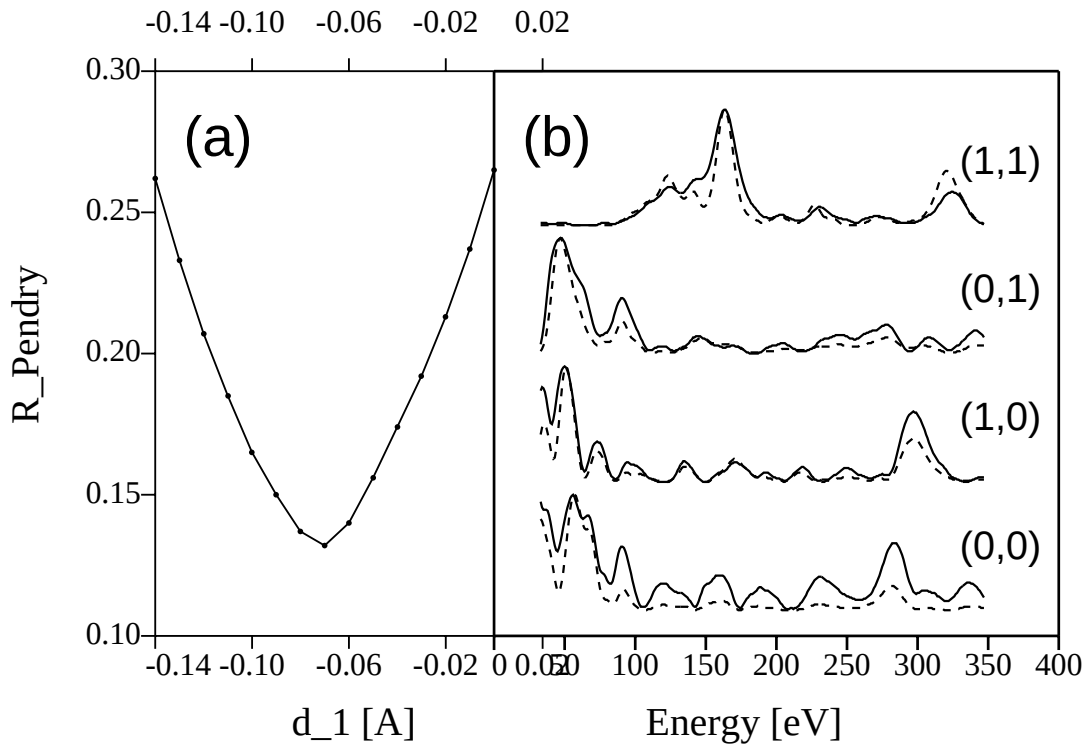

Figure 3.5: LEED data acquired at room temperature. a) R_P vs. first interlayer spacing, d_1. For each fixed d_1 value in the graph, R_P has been minimized as a function of d_2, thus taking correlation effects into account at room temperature. Gray horizontal line gives the R-factor variance, ΔR_P, from which the error bars are estimated. b) Comparison between experimental (solid lines) and calculated (dashed lines) I-V curves for the Ru(0001) surface at room temperature. The total incident-beam energies spans a range of 1109 eV.

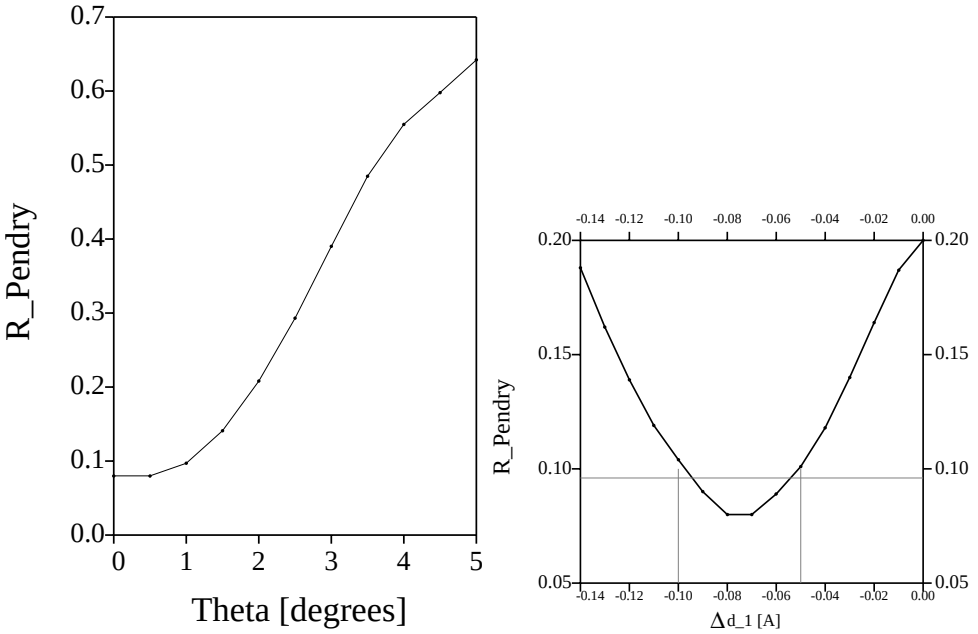

Figure 3.6: Left) R_P vs. Theta (the electron beam incidence angle) projected for d_1 and d_2. Right) R_p vs. d_1 projected for d_2 and Θ. Again, the optimized d_1 value is not changed.

off-normal misalignment

We next discuss the advantages of determining a surface structure from a single terrace instead of using multiple terraces. First, for single-terrace data a larger energy range, ΔE, can be obtained since symmetry-inequivalent beams are not averaged together. This larger energy range improves the reliability of the fit. Indeed, our energy range is larger than that used in previous LEED analysis [74]. To evaluate this potential error source, we performed an independent R-factor analysis of our experimental data where the experimental (10) and (01) beams were averaged. Compared to the single-terrace data set, the best fit for this symmetrized data set shows a slightly smaller interplanar contraction but a significantly larger error bar, $\delta d_1 = -3.3(1.4)\%$. With this larger error, this result would be compatible with the previous experimental results.

An additional uncertainty in multiple-terrace data is that the two terrace types are usually taken as being present in equal abundance. But this is not always the case. Ru(0001) has a marked tendency to form "double-steps," that is, one terrace type is considerably wider than the other terrace type. The narrow terrace type is bounded by two closely spaced ("double") steps. Which terrace type is more abundant depends upon the local orientation of the steps. Even for an averaging technique, such as obtained from

a traditional diffractometer, the two terraces types may not be in equal abundance, giving an extra parameter to fit and increasing the error bars. This effect might explain the experimental observation of three-fold patterns on Ru surfaces by X-ray photoelectron diffraction [82]. In fact, the change in symmetry has been employed to monitor the presence of double steps [78]. Double-steps may also introduce a non-negligible correction to the usual assumption of incoherent beam mixing in the theoretical I-V simulations, further reducing the reliability of the R-factor analysis.

Structural Parameters [Å]		Non-structural Parameters	
d_1	2.065 ± 0.02	r_m	2.00 bohr
d_2	2.140 ± 0.025	V_i	-2.6 $E^{1/3}$ [eV]
d_{bulk}	2.141	Θ_D^1	350 K
		Θ_D^2	400 K
		Θ_D^{bulk}	600 K

Table 3.1: Optimized structural and non-structural parameters deduced in this thesis. See text and section §A-i for further explanations.

The final point concerns the role of adsorbed hydrogen in the experimental structures[1]. We note that our structure, which was obtained from a crystal above room temperature, agrees extremely well with *ab-initio* calculations. Since there is no disagreement, we find no need to invoke impurity effects. To our knowledge, this is the only experimental result which corroborates the 3.5% contraction deduced from the hydrogen-free DFT calculations.

3.2.3 Summary

Using a LEEM instrument we have performed, for the first time, a LEED I-V analysis from a single atomic Ru(0001) terrace. The experimental I-V curves were excellently fit by full dynamical calculations. The best-fit parameters are shown in Table 3.1. In the best-fit structure, the topmost Ru layer is relaxed inward by about 3.5%, in excellent agreement with *ab-initio* calculations. We suggest that determining structures from

[1]The LEED analysis of Menzel *et al.* as well as the SXRD analysis of Baddorf *et al.* concluded that H adsorption was not responsible for the experimentally determined Ru(0001) first interlayer spacing [60, 77]. However, the calculations of Feibelman *et al.* [74] show that H adsorption significantly decreases the surface contraction.

small areas has clear advantages even for surfaces that consist of a single structure (phase), such as Ru.

3.3 Ru(0001): Surface Morphology

We use two different Ru(0001) crystals, one in each LEEM. Both crystals contain areas, at least 100 μm wide (see Fig. 3.7 and Fig. 2.5) , with a low density of atomic steps. In this regions, terraces more than 5 μm wide can routinely be found (Fig. 3.9). These are extremely flat regions rarely found in refractory metals. The flat regions on this two samples have been found for the first time by the author and his group. The LEEM fast operation have been crucial to map macroscopic regions of the surface with microscopic resolution, to find the flat regions.

Outside the flat regions, both samples have a small surrounding area with high density of steps (see Fig. 3.8). The rest of the surface have regular-sized terraces of thinner that $\sim$30 nm.

All our experiments have been carried out in the ultra-flat and defect free regions of the surface. These regions are ideal for a LEEM study, allow us to be sure of the thickness of the thin films grown on the Ru(0001) substrate and to avoid to average over consecutive terraces.

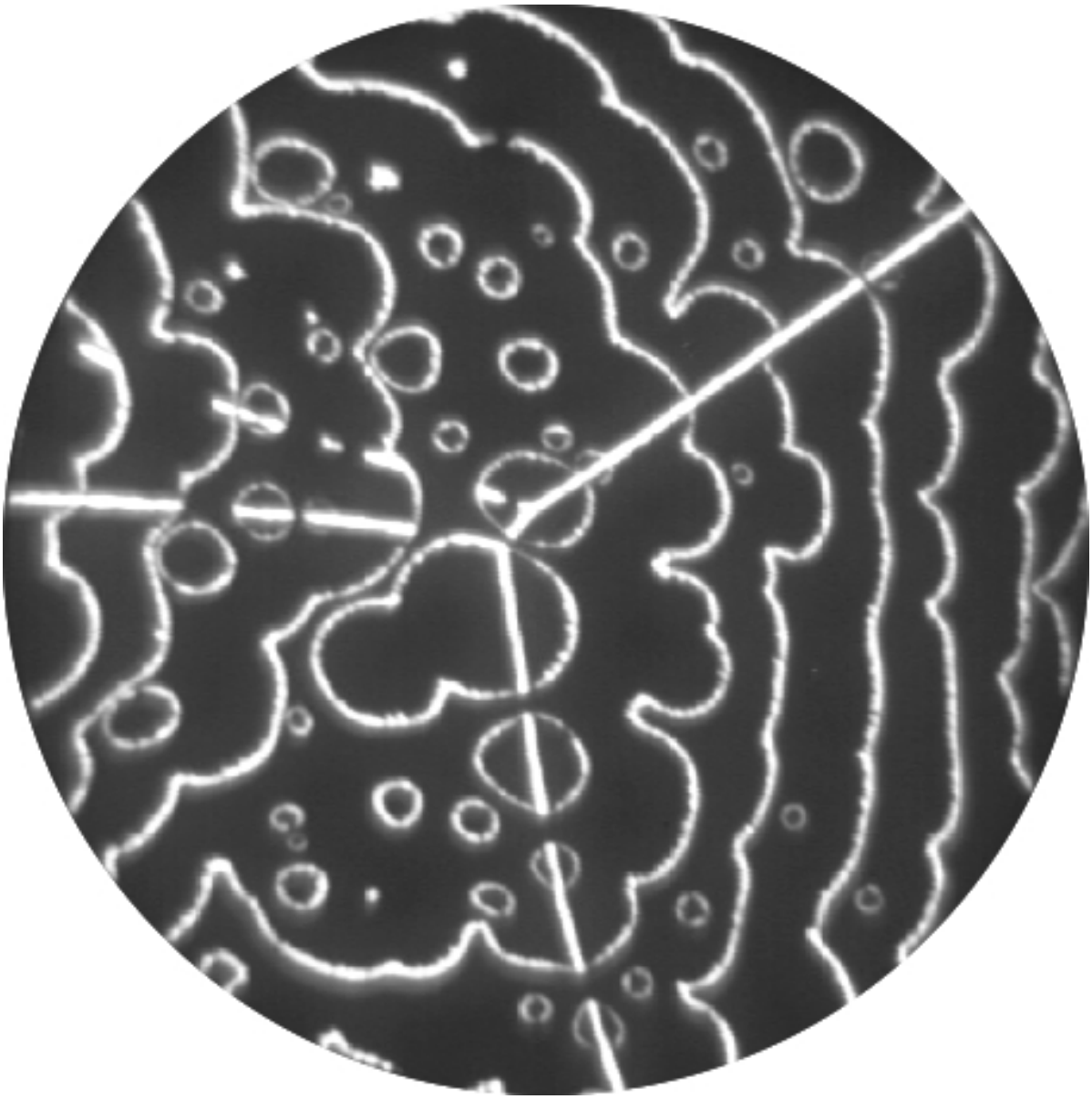

Figure 3.7: Photoemission Electron Microscopy (PEEM) image of one of the two Ru samples used in this thesis. In order to obtain a high-contrast and large-FOV image of the Ru(0001) surface was slightly covered with Ag and illuminated with an ultraviolet lamp inside a LEEM instrument. The photoemitted electrons are measured by the LEEM as if they were reflected electrons. The resulting image is called PEEM image. It has much less resolution than the LEEM but, in the other hand, give us chemical contrast. The deposited Ag enhances the contrast at the Ru(0001) steps. The image have a FOV of 100 μm, showing the extremely flat constitution of this surface, with only a dozen of monoatomic steps. The radial lines are low angle grain boundaries.

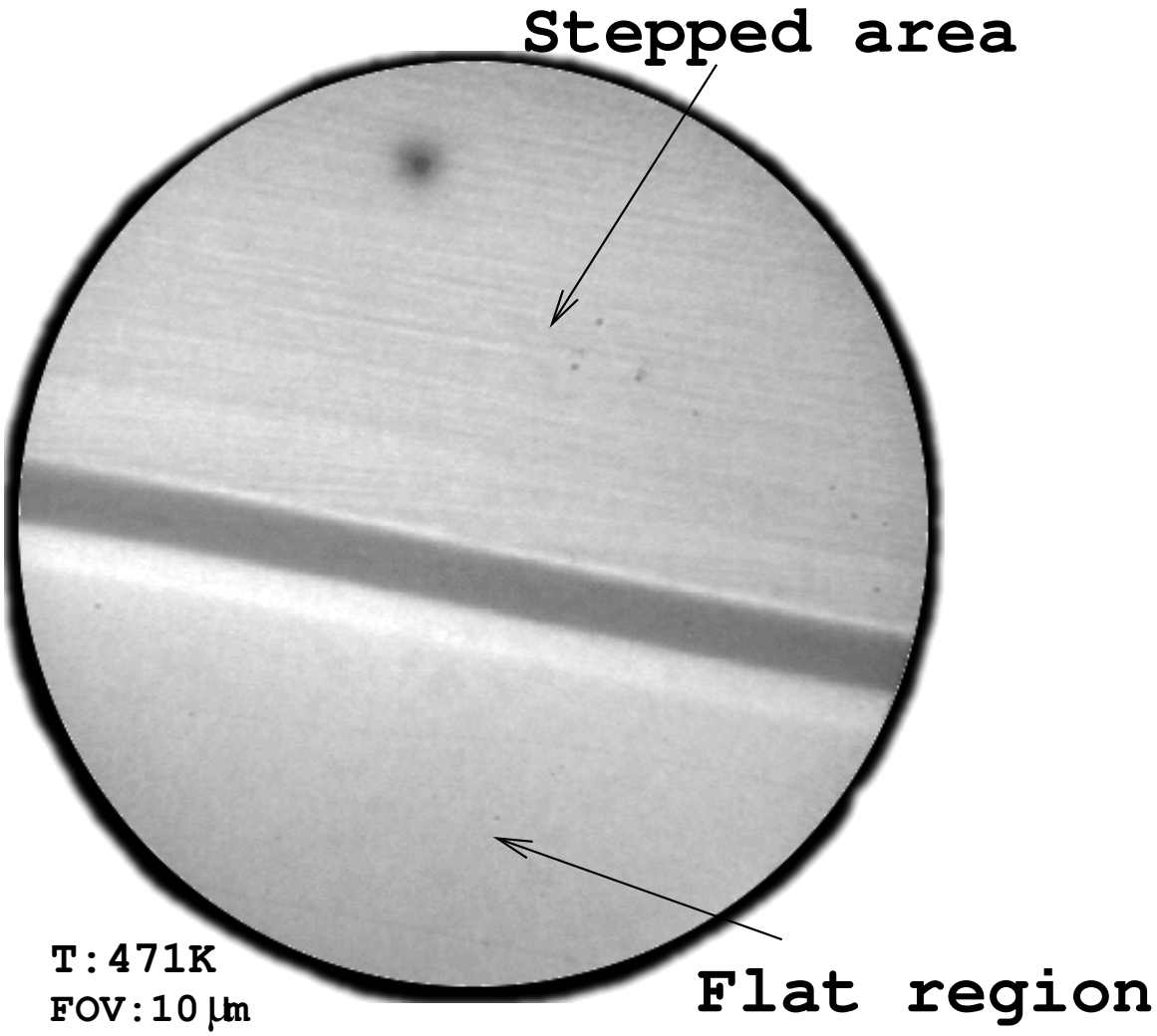

Figure 3.8: LEEM image of the clean Ru(0001) surface of one of the samples with an ultra-flat region. The image shows the flat region (lower part), with only two monoatomic steps, the border composed of a step-bunch (dark grey), and the regularly stepped area (upper part). The dark spot in the upper part is an artifact produced by a small burned region of the channel plates of the LEEM.

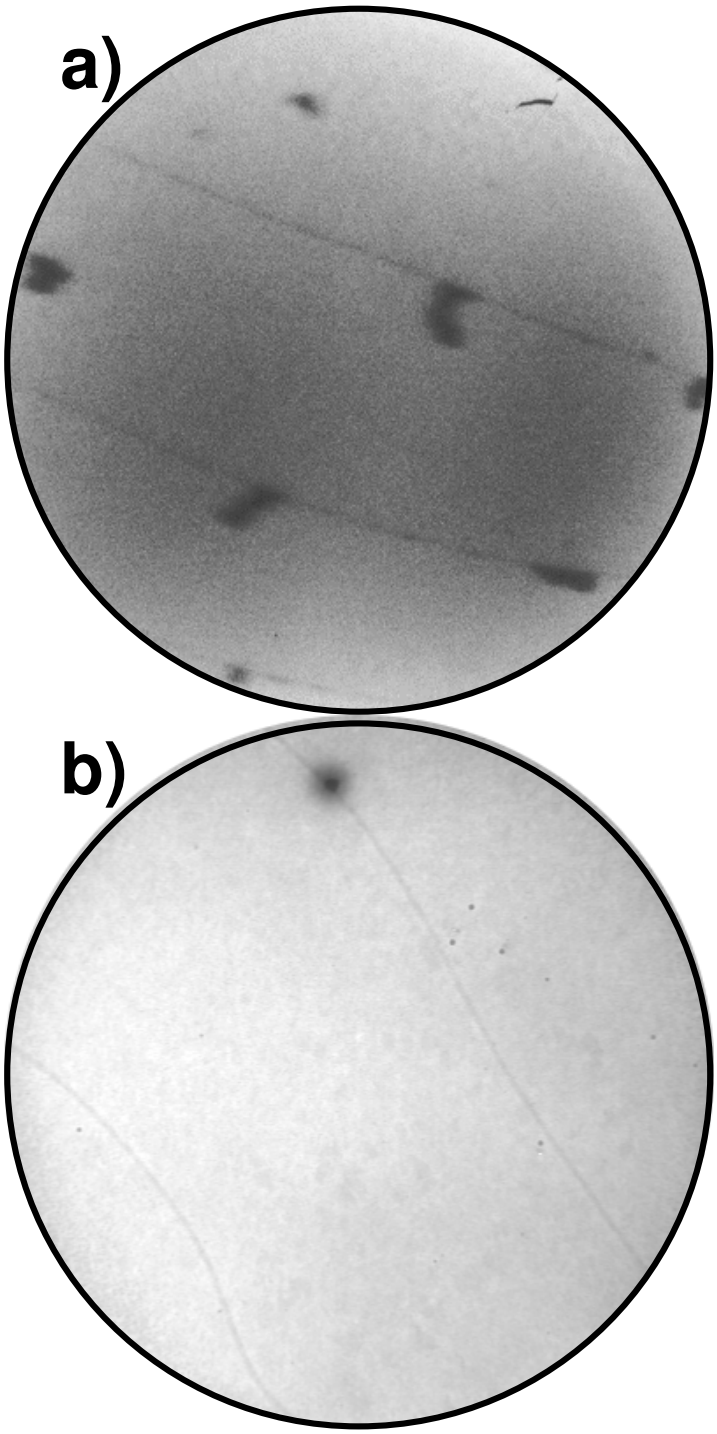

Figure 3.9: LEEM images of the typical flat regions founded in the two Ru(0001) samples used in this thesis. a) First stages of the Pd (black regions) growth on Ru(0001)(light grey) at NCEM SPLEEM. The FOV is 5 μm and shows only two monoatomic steps. b) Clean Ru surface measured at SNL LEEM. The FOV is 10 μm and shows only two monoatomic steps.

Chapter 4

Cobalt on Ruthenium (0001): Growth, Dynamics and Structure

"On the other side of the screen, it all looks so easy."
— *Tron*, Flynn, 1982

Many studies have shown that the magnetic properties of layered systems composed of cobalt and ruthenium are very interesting. This led to important applications, for example Ru spacer layers are used to induce an antiferromagnetic coupling between thin films of Co-alloys in both spin-valves and magnetic recording media [4]. Previous studies have shown that deposition of Co on Ru can result in the formation of three-dimensional islands in a Stranski-Krastanov growth mode [8–10]. Under appropriate conditions we have shown that Co can be grown layer-by-layer up to 10 monolayers (ML) [11]. In chapter 5, magnetization will be monitored as a function of film thickess, which revealed that the film magnetization easy-axis changes from an in-plane orientation for monolayer thick films, to perpendicular for bilayer islands or films, and back to in-plane again for thicker islands or films.

In this chapter we present a detailed characterization of the morphology and the structure of Co films grown on Ru(0001) up to 3 ML thick. We employ low-energy electron microscopy (LEEM [2, 41, 43]) to follow in real time the growth of the films. The films grow layer by layer, through the nucleation and growth of triangular-shaped islands in large substrate terraces. The orientation of the islands is expected to reflect the stacking sequence of the Co layers that form each island [83, 84] (see Fig. 4.1). We confirm

this hypothesis using low-energy electron diffraction (LEED [85, 86]) intensity-vs-energy (IV) curves acquired from a single terrace on the surface. The original demostration of the method is described in section 3.2 and in Ref. [87] where we successfully characterize a clean Ru terrace showing the expected three-fold symmetry instead of the commonly observed six-fold pattern due to averaging over the different surface terminations of clean Ru. We use multiple scattering calculations (see section §A-i) to fit the experimental LEEM-LEED data. The results are summarized in table 4.1, where Frank's notation for stacking sequences [88] will be shown to reflect the sequence of island shapes observed in the films.

4.1 Experimental Details

The Co films were grown on two different Ru(0001) crystals. The substrate cleaning procedure was described in chapter 3. Co was dosed in-situ from an electron-bombardment doser with a Co rod. Typical evaporation rates were between 1 ML/2 min and 1 ML/35 min. The pressure in the chamber remained below 4×10^{-10} torr.

We used the LEEM instrument to measure Intensity-vs-Energy (IV) curves [85, 86] by placing an aperture in the electron beam path to reduce the illuminating beam diameter on the sample to a few μm (see section 2.1.2). In this way LEED data can be measured from a micrometer-sized area of the film.

4.2 Results and Discussion

The growth on flat areas of the sample proceeds layer-by-layer up to at least 10 ML. In Fig. 4.1 we show frames from a representative movie of the film grown on terraces larger than 5 μm. Islands are nucleated on the terraces in addition to some material growing from the steps of the substrate. The shape of the islands is triangular. On a given substrate terrace, the islands point in one direction for 1 ML islands on Ru, and in the opposite direction for 2 ML islands on a 1 ML film. For 3 ML islands on a 2 ML film, two orientations can be detected on a single substrate terrace.

To understand more about the structure of the growing film, we perform selected area diffraction on areas of uniform thickness. The corresponding LEED patterns are shown in the right panel of Fig. 4.1. In 3 ML areas, correlated with the shape of the

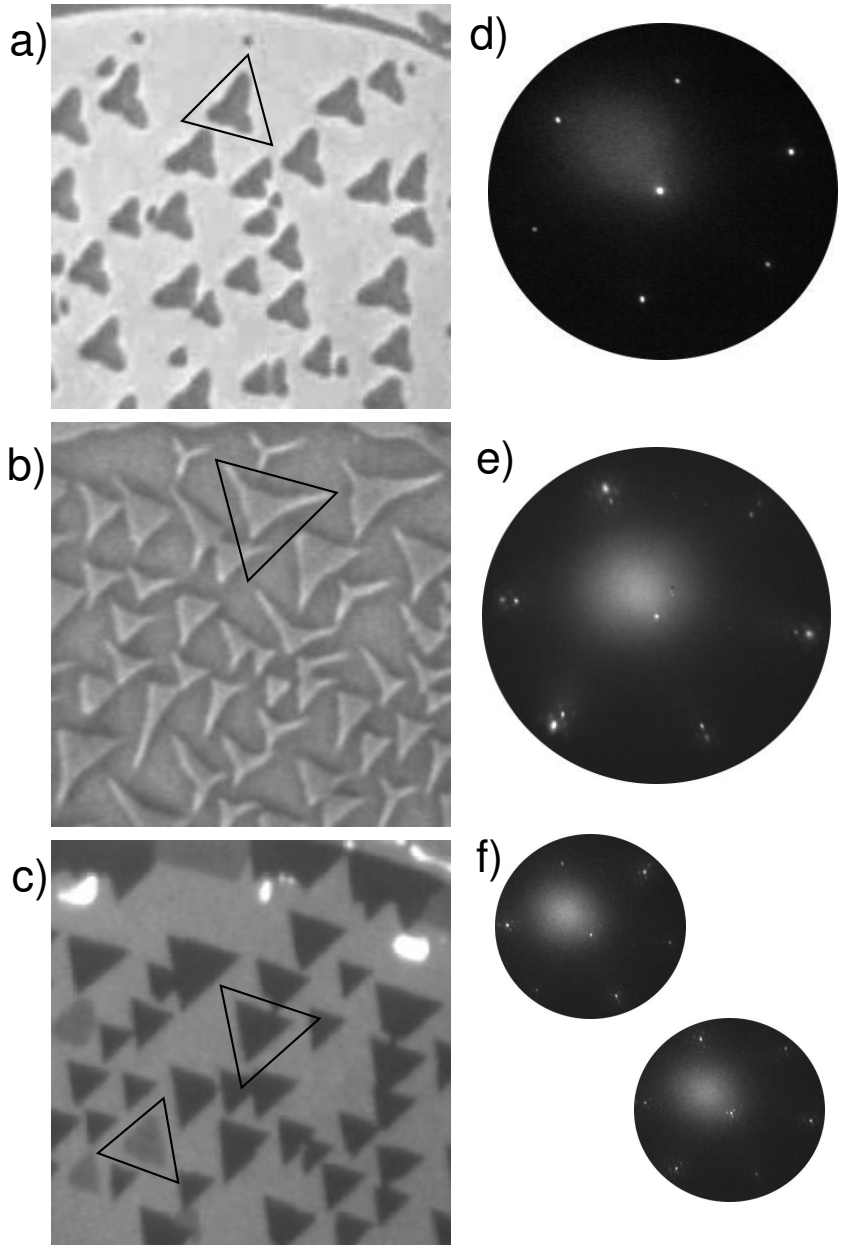

Figure 4.1: LEEM images of the same region of a Ru(0001) sample (left row) and LEED patterns measured in regions of the same thickness (right row). The LEEM images have a field of view (FOV) of 10 μm, and an electron Energy (eE) of 5 eV. The growth rate and temperature were 1 ML/220s and 515 K respectively. The LEED patterns have and energy of 60 eV (1 ML and 3 ML) and 37 eV (2 ML). The two LEED patterns for 3 ML areas were acquired on the same substrate terrace, on the two different regions that originated from islands with different orientation.

original islands, two LEED patterns are found. There is also a clear difference between the LEED patterns of different thickness films. One monolayer islands and films are pseudomorphic, presenting only 1×1 beams at the same position of the Ru substrate beams. 2 ML and thicker islands or films, on the contrary, present more complex LEED patterns with satellite beams around the substrate ones. In both cases (2 ML and 3 ML) the satellite beams around the specular beam appear close to hexagonal positions with the same orientation that the Ru integer beams (i.e. the superstructure beams are non-rotated relative to the substrate ones).

The observed LEED patterns for thicker films are typical of structures arising from a difference between the in-plane lattice parameter of the film and the substrate (as seen, for example, in Co/Pt(111) [89] or 4 ML Cu/Ru(0001) [90]). The simplest of such structures is a moiré pattern formed by the coincidence lattice between substrate and film. In principle, in a moiré pattern all relative positions between film and substrate atoms are present. But under strong film-substrate interaction, as expected for the CoRu system, most of the film atoms fall into three-fold hollow sites (either fcc or hcp adsorption sites) with a few remaining atoms close to bridge and on-top positions. This is easily observed in Frenkel-Kontorova models (see figure 1.2b of chapeter 1, or the Frenkel-Kontorova calculations in Fig. 10 of Ref. [91]): the commensurate supercell is split into two halves: one with predominant hcp stacking and the other one with predominant fcc stacking, separated by atoms in or close to bridge and on-top positions. In average, most of the film is expected to be in either fcc or hcp stacking relative to the substrate. Following this argument, we will perform simplified LEED fits to combinations of different stacking sequences.

The work shown here relies on the ability to grow Co films that are extremely flat. The resolution limit of current LEEM systems, as well as the limitations in the illumination spot size for selected-area LEED experiments, require flat films for a proper characterization using electron microscopy. A previous LEED and Auger Electron Spectroscopy (AES) work detected Stranski-Krastanov growth for Co on Ru(0001) [8]. It has been proposed and proved in particular cases [92] that in thin films with a significant misfit with the substrate, and consequently with a strong tendency to dewet from the surface, the presence of steps provides a kinetic pathway for three-dimensional growth. Hence, the lack of steps should prevent such growth for some range of growth conditions. The acquisition speed and large field of view of the LEEM make it possible to map large regions of the surface and locate extremely flat regions. Indeed, the samples used in the current experiments showed regions where terraces larger that 10 μm could be found.

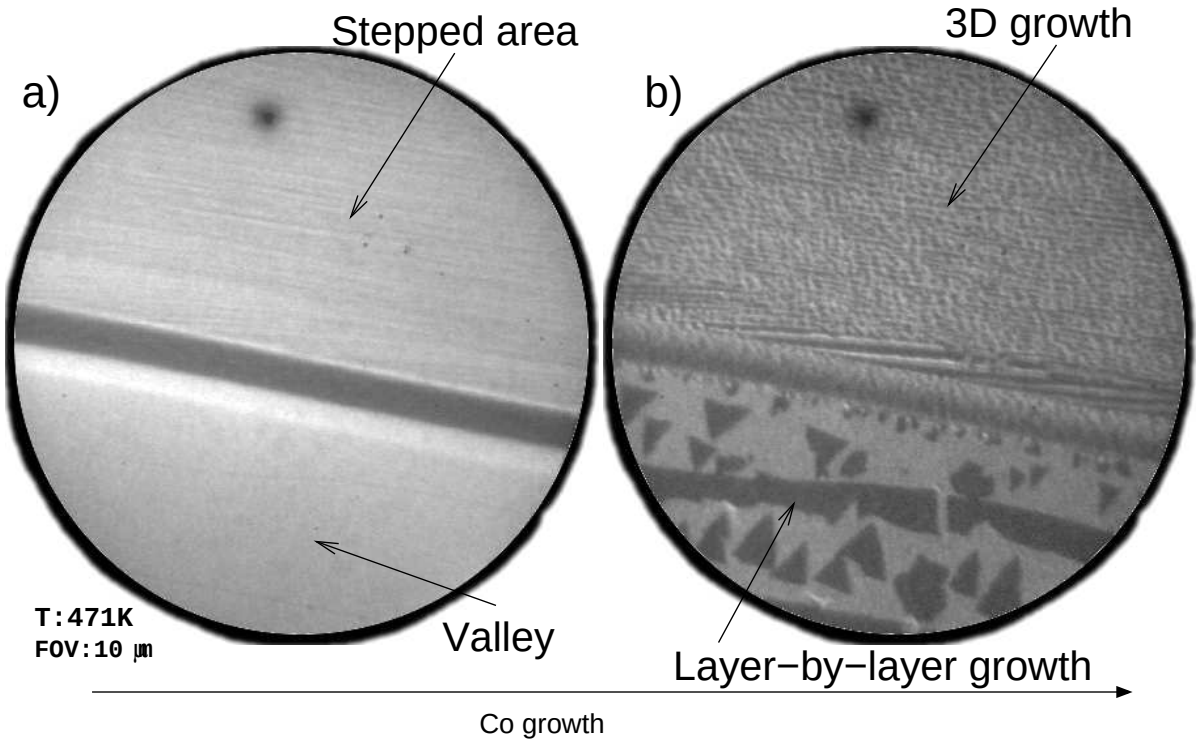

Figure 4.2: LEEM images of the same region of a Ru(0001) sample, with a field of view (FOV)=10 μm. a) Clean Ru. b) After growth of 2.5 ML of Co [T=471 K, flux=1ML/210 s, electron Energy (eE)=21.6 eV]. These images show the border of an extremely flat valley that is surrounded by a stepped region. The lower part of the images is a flat region with only three atomic steps. The dark grey band in the middle of the images is a step bunch. The upper part shows a stepped region of the Ru. After Co growth b), in the lower area there are 3 ML Co islands (dark grey) over a 2 ML complete film (medium grey) indicating layer-by-layer growth. In the stepped region the Co grows in Stranski-Krastanov mode.

On such flat areas (see Fig. 4.2), the growth proceeds layer-by-layer up to more that 10 ML. In contrast on more stepped areas 3D islands form during growth.

The growth temperatures employed were in the range of 440–520 K. At higher temperatures a LEED pattern ascribed to CoRu alloy (see Fig. 4.3) could be detected. At lower temperatures, the Co islands were too small to be properly detected by LEEM.

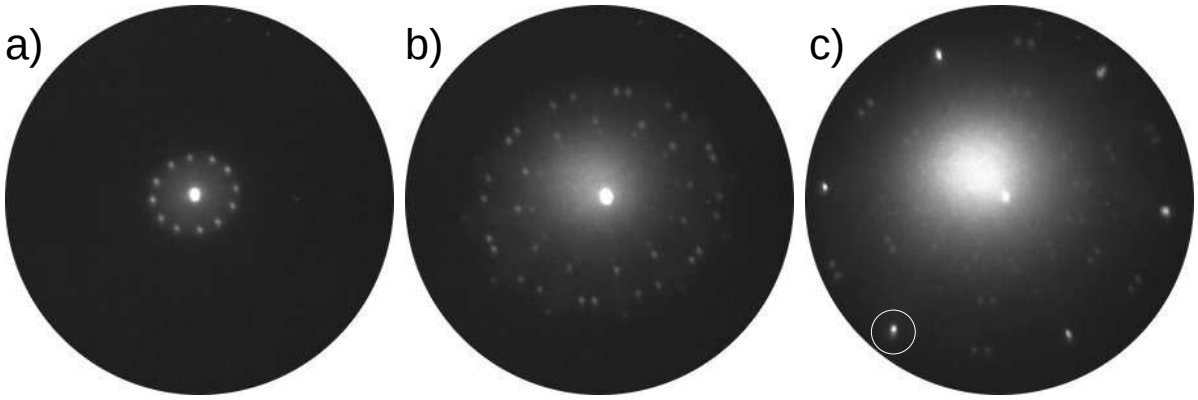

Figure 4.3: LEED snapshots at three energies (3.9 eV, 20 eV, 31 eV) of the CoRu LEED pattern obtained after heating Co monolayer film to 750 K. 31 eV pattern (one is circled). Hints of the same LEED pattern were also observed when the deposition was performed as low as 533 K and followed by annealing at that temperature for an hour. All images present the same magnification.

Coverage	Stacking (ABC)	Stacking (Frank's)	$a_{\parallel}$	d_1	d_2	d_3	d_{bulk}
1 ML	BA/B	$\bigtriangledown\bigtriangleup/\bigtriangledown$	2.70	2.05±0.05	2.10±0.02	2.14	2.14
2 ML	BA/(CB+BA)	$\bigtriangledown\bigtriangleup/(\bigtriangleup+\bigtriangledown)\bigtriangleup$	2.56±0.08	1.94±0.06	2.14±0.08	2.14	2.14
3 ML-I	BA/(CBA+BAC)	$\bigtriangledown\bigtriangleup/(\bigtriangleup+\bigtriangledown)\bigtriangleup\bigtriangleup$	2.54±0.08	1.99±0.06	2.06±0.08	2.14	2.14
3 ML-II	BA/(CBC+BAB)	$\bigtriangledown\bigtriangleup/(\bigtriangleup+\bigtriangledown)\bigtriangleup\bigtriangledown$	2.52±0.06	1.97±0.04	1.99±0.06	2.14	2.14

Table 4.1: Optimized structural parameters for the Ru(0001)-p(1×1)+Co system and for the three coverages studied in this work: 1, 2 and 3 MLs. For the 3 ML case, we provide the values for each phase. All distances are given in [Å]. Input records without error bars were not optimized in the IV analysis. See text for further explanations.

4.2.1 The first monolayer

The growth of monolayer thick islands (as well as thicker films) was followed in real time with LEEM. Good contrast conditions with a high intensity of backscattered electrons can be selected with an incoming electron energy of 5 eV. The monolayer islands appear dark on a light grey background corresponding to the Ru substrate, although contrast is strongly dependent on focus conditions.

A sequence of images of Co growth at different temperatures and rates are shown in Fig. 4.4 for coverages below 1 ML. There is no growth of the second layer until more than 90% of the Ru surface is covered.

The shape of the growing islands is triangular, as already reported in a previous STM study [93, 94]. All the islands present the same orientation within each substrate terrace and are oriented along compact directions of the substrate surface. When crossing from one terrace to the next, the islands change their orientation by 180°. This change is explained by the substrate hcp(0001) structure, where a rotation of the terrace structure by 180° occurs at the crossing of every atomic step [60, 87] -see also Fig. 4.5b. In order to describe the stacking sequence of the films, we will use two notation styles. The first is the classic labeling A,B or C for each possible hexagonal layer, with ABC... or BCA... indicating a fcc structure, and ABAB... an hcp one[1]. Additionally, it is helpful for summarizing and understanding our results concerning *the orientation* of the triangular-shaped islands to employ Frank's notation [88]. In it, the stacking of the layer relative to the one below is labeled. Transitions of one layer to the next following the sequence A→B→C→A are denoted by $\bigtriangledown$, while the opposite transitions, namely C→B→A→C are denoted by $\bigtriangleup$. An fcc structure is written down either $\bigtriangleup\,\bigtriangleup\,\bigtriangleup$ or $\bigtriangledown\,\bigtriangledown\,\bigtriangledown$. An hcp structure corresponds to $\bigtriangleup\,\bigtriangledown\,\bigtriangleup\bigtriangledown$.

An hexagonal island on an hexagonal substrate presents two types of symmetry inequivalent step edges (Fig.4.5a). Each step type exposes microfacets [95]. In principle the observed shape could either correspond to the equilibrium shape of bidimensional Co islands on Ruthenium, or be due to kinetic limitations in the diffusion of adatoms along the side of the islands. However, when islands coalesce the merged multisided shapes did not readily evolve into compact, equilibrium shapes implying that edge diffusion is too slow at our growth conditions to equilibrate the island shape. Thus, triangular

[1]The layers are named consecutively usually including the last two Ru layers followed by a slash to indicate substrate termination. One monolayer continuing the bulk hcp sequence in a given terrace will be thus denoted AB/A.

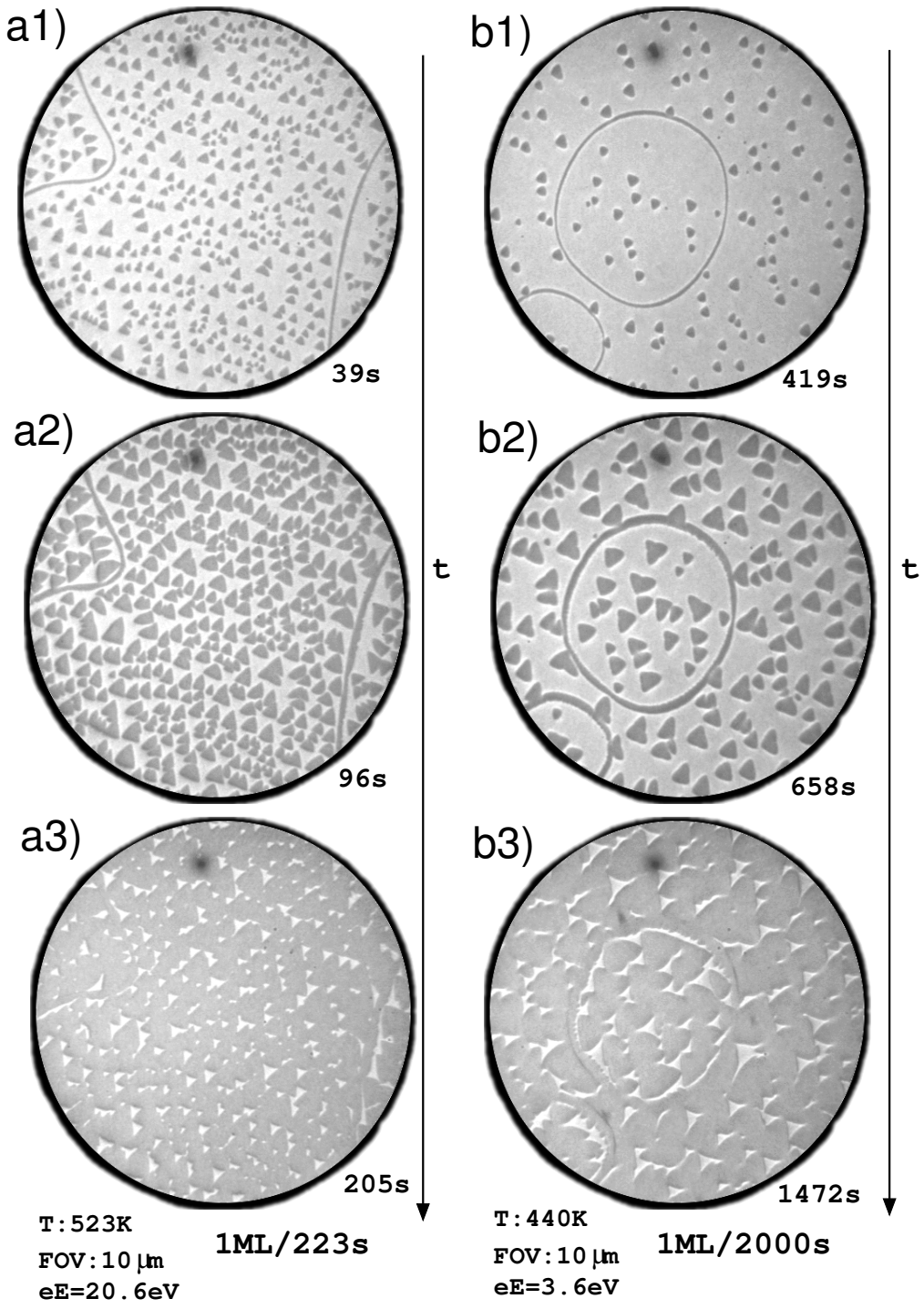

Figure 4.4: LEEM images taken while growing 1 ML of Co/Ru(0001). Co is dark grey and Ru is light grey. Three frames (n1, n2, n3) are shown in chronological order for each of the two experiments (a and b) represented.

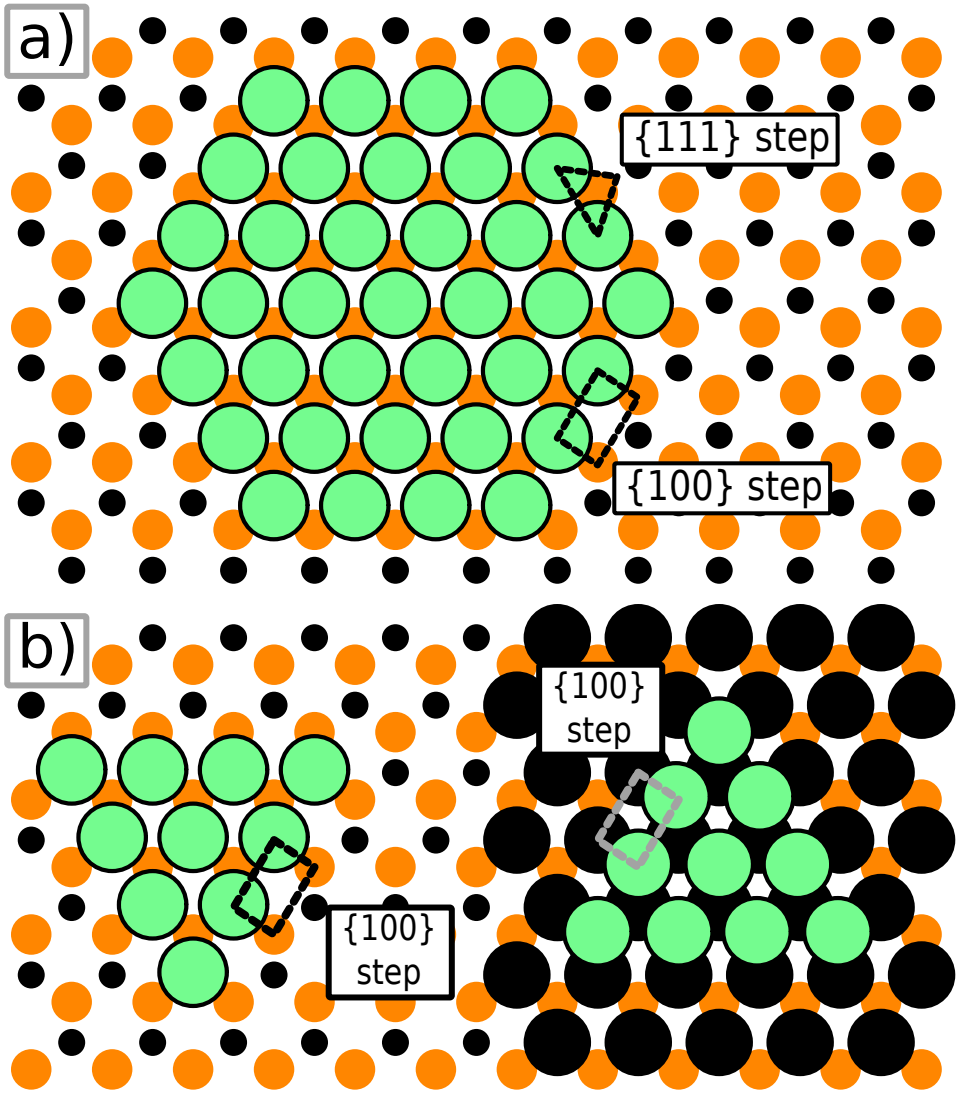

Figure 4.5: a) Schematic of an hexagonal island on an hexagonal substrate. There are two kind of step edges, the {100}-type and the {111}-type. The diffusion along the different types of steps is, in principle, different. b) Schematic of triangular islands bounded by 100-type steps and following the hcp stacking sequence. If the islands grow in consecutive terraces (left and right sides of the schematic) the triangles will point in opposite directions in order to expose the same step edge.

shape is dictated by kinetic limitations and it does not reflect the formation energies of the different step edges [96, 97]. The same conclusion was obtained from previous STM observations [93, 98].

The fact that all observed islands point in the same direction within each substrate terrace is a strong hint that there are no stacking faults (SF) within 1 ML islands [83, 84]; stacking fault islands would appear rotated by 180° in order to expose the same step edge (as discussed for the 3 ML case below, Fig. 4.12).

The selected-area LEED pattern from a cobalt-monolayer covered region only shows integer (1×1) spots (Fig.4.6a). Thus, the film is pseudomorphic with the substrate. The Co films were grown at 464 K and LEED IV curves were measured three hours later when the sample was at room temperature. The three (10) and (01) beams, as well as four symmetry-equivalent beams to the (11) were averaged, spanning a total energy range of 1164 eV. The experimental IV-curves are shown in Fig.4.6b -solid lines. For the structural analysis we considered both possible terminations for the Ru terrace: ABA/ or BAB/, together with the hcp and fcc stacking sequences for the Co layer. Thus, we explored four stacking sequences in total: BA/B, BA/C, AB/A and AB/C -rightmost (leftmost) letter refers to the Co (2nd Ru layer) stacking[2]. The R-factor analysis yields an acceptable agreement for the BA/B hcp sequence, $R_P^{BA/B}$=0.23, while the rest of cases may be ruled out given their poor fit to the experimental curves: $R_P^{BA/C}$=0.76, $R_P^{AB/A}$=0.66 and $R_P^{AB/C}$=0.59. In Frank's notation, the best fit structure corresponds to $\bigtriangledown\bigtriangleup/\bigtriangledown$. The advantage of Frank's notation is that the relative in-plane orientation of a one-layer thick triangular island exposing the same type of step edge on top of the previous layer is automatically indicated by the relative orientation of the symbols: hcp islands alternate their orientation from layer to layer, while fcc islands do not.

Therefore, our main conclusion for the 1 ML case is that Co grows on Ru keeping both the in-plane lattice parameter and the hcp stacking sequence. The above R_P values show, on the other hand, a strong sensitivity to the bulk Ru orientation, allowing us to establish unambiguously the BABA/ or $\bigtriangledown\bigtriangleup$/ termination of the Ru terrace where the LEED patterns were acquired. This fact will become relevant for the analysis of higher Co coverages since for those cases the Ru orientation cannot be otherwise determined (see next subsections).

[2]There are actually only two different stacking sequences, plus another two that correspond to the same ones exchanging the labeling of the experimental beams. Once the experimental beams are labelled for the 1 ML film, we will keep the same labelling for thicker films to relate films grown on the same substrate terrace.

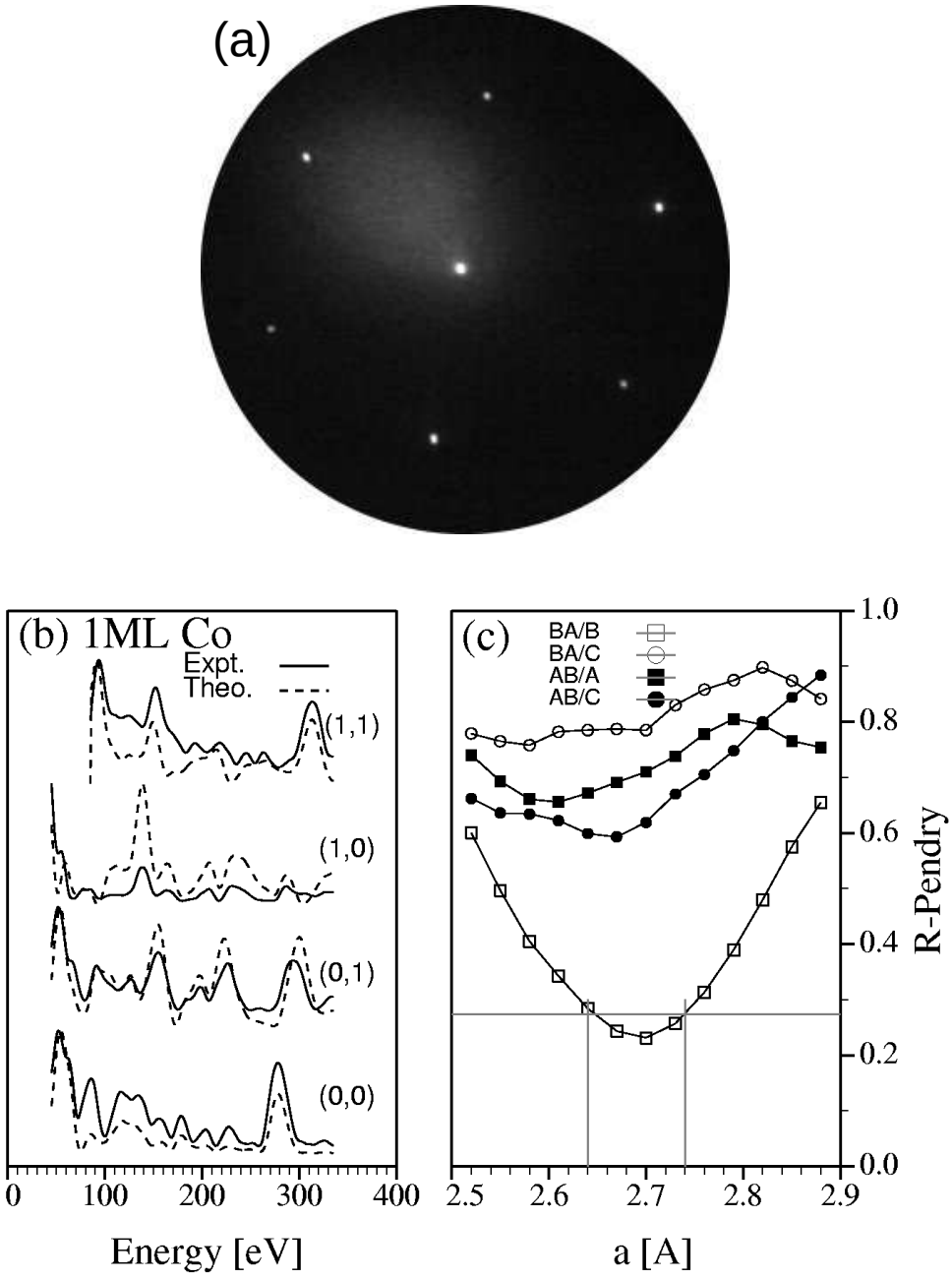

Figure 4.6: LEED of 1 ML Co/Ru. (a) LEED pattern at 60 eV b) Experimental and best fit calculated IV curves. c) Pendry's R-factor, R_P, vs. in-plane lattice parameter of the (1×1) cell, $a_{\|}$, for each of the four possible stacking sequences considered. For each sequence and $a_{\|}$ value, we plot the best R_P value among the rest of the structural parameters. The horizontal grey line corresponds to the R-factor variance for the best-fit stacking sequence, hcp, from which errors (vertical grey lines) on this parameter are estimated.

The associated interlayer spacings are reported in Table 4.1. Given the misfit of 7.3% between the in-plane lattice spacings of bulk Co and bulk Ru, the Co film is expected to be severely strained. This strain is reflected in the first Co-Ru interlayer spacing, d_1 =2.05 Å, which is 4% smaller than the bulk Ru-Ru normal distance, and leads to an interatomic distance d_{Co-Ru} =2.58 Å, which is in nice correspondence with the sum of their covalent radii, $r_{Co}+r_{Ru}$=1.25+1.34=2.59 Å. Finally, Figure 4.6c presents the R-factor behavior vs. $a_{\parallel}$ for all stacking sequences explored. The purpose of this fit is to check the sensitivity of the LEED IV curves the Ru in-plane lattice constant, $a_{\parallel}^{Ru}$=2.70 Å. the error estimation reveals a reasonably good lateral resolution of ±0.03 Å.

Once we know the structure of the 1 ML film, we proceed to determine the type of step edge of the islands. To such end we need to orient the diffraction pattern of a film of 1 ML of Co on a single Ru terrace relative to the triangular orientation of the growing islands. Given that the magnetic lenses of the LEEM system used for LEED measurements rotate the image when going from imaging the real-space surface to focussing the LEED pattern, the rotation between both lens settings is determined experimentally. By comparing the island shape and the LEED pattern *on the same substrate terrace* we determine that the step edge exposed is of type {100}.

When the Co islands are close to completing the monolayer a change in contrast is observed onto the monolayer film (Fig. 4.7). The new phase grows quickly until it covers nearly the entire 1 ML film. Second monolayer islands are nucleated very close in time to the appearance of the new phase in the ML areas. As the 2 ML islands grow, the new 1 ML phase starts to dissapear around them. If the growth is interrupted, the new phase disappears after half a minute at 523 K. A similar effect is observed in Cu/Ru(0001) [99] and Pt/Pt(111) [100] films, where the new phase corresponds to the nucleation of a metastable network of misfit dislocations in the monolayer areas, making the film about 5% denser than before. In those systems, the network of dislocations is only stable under a high concentration of adatoms on top of the film. This effect is explained by the difference in the energy required to incorporate an atom into the film depending on whether the atom is an adatom or whether it is incorporated from an step edge, as suggested by Frenkel-Kontorova modelling [91]. We propose that the new phase in the Co-monolayer areas also corresponds to a network of misfit dislocations. In support of our interpretation, we note that misfit dislocations have been observed in Co monolayer islands by STM [101]. The high concentration of adatoms on the 1 ML islands is only achieved when the islands cover most of the Ru surface (which otherwise acts a an adatom sink). Once 2 ML islands are nucleated the adatom concentration falls,

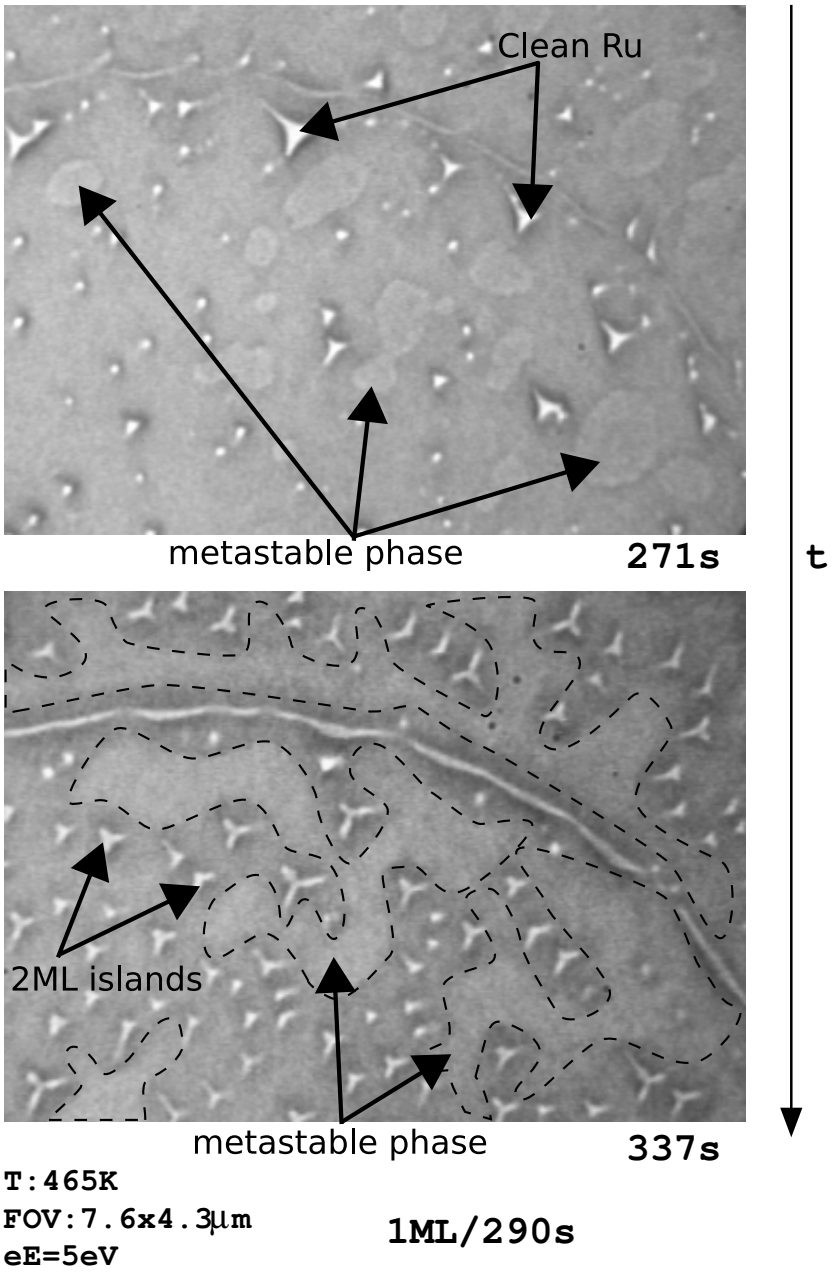

Figure 4.7: LEEM images as the first Co layer completes and the second layers nucleates, showing the appearance of a new phase. The growing conditions are indicated. The new phase fills up all the monolayer areas of the surface and it disappears when the second cobalt monolayer starts to grow. The time between frames is 66 sec. Dashed lines frame the light-grey metastable phase when it coalesces

explaining the appearance and subsequent dissappearance of the phase at the onset of the 1 ML Co completion.

4.2.2 The second monolayer

The growth of the second layer is shown in Fig. 4.8. There exist many similarities with the 1 ML case. The shape of the islands is triangular with a single orientation within each terrace, suggesting that there are no differences in stacking sequence between 2 ML islands on the same substrate terrace. The orientation of the triangles changes from terrace to terrace while the orientation of the islands of the 2 ML relative to the 1 ML in the same terrace is also changed by 180°(compare Fig. 4.8a1 with Fig. 4.4a1). All this evidence suggests that the 2 ML islands grow keeping the Ru bulk hcp stacking sequence.

The detailed atomic structure is, however, more intricate. The LEED pattern shows satellite spots around the specular and the Ru integer-beams (Fig. 4.9a), aligned in the same directions as the Ru beams. Thus, the in-plane lattice spacing of the 2 ML Co islands differs from the lattice spacing of the Ru substrate. The spacing of the satellite spots is 5.4±2% where the error bar is due in part to distorsions of the LEEM imaging optics. The decrease of the intensity of the satellite spots along the lines joining the specular beam and the first order Ru beams suggests an inconmensurate structure.

The LEED pattern confirms previous STM experiments [94] that observed a periodic pattern ascribed to the different lattice parameters of the Co film and the underlying Ru substrate. The reported size of the unit-cell was close to an 13x13 Ru unit-cell [94, 101]. Such an film structure, present also in Co/Pt(111) [89] or 4 ML Cu/Ru(0001) [90], could in principle have all possible stacking positions of the overlayer atoms relative to the substrate atoms. Nevertheless, as discussed before, in the presence of substantial film-substrate interaction, most of the film atoms are expected to be positioned close to three-fold hollow sites, either fcc or hcp stacking positions, with a small fraction of atoms close to bridge or on-top positions.

We have attempted a LEED IV structural analysis similar to the 1 ML case. Taking into account the reported STM observations and with the goal of determining the stacking sequences present in the films, we have made the following simplifications: we only considered combinations of perfect stacking sequences of atoms (A,B, or C stacking positions, not bridge nor on-top positions), and the Co layers plus the bulk Ru have been

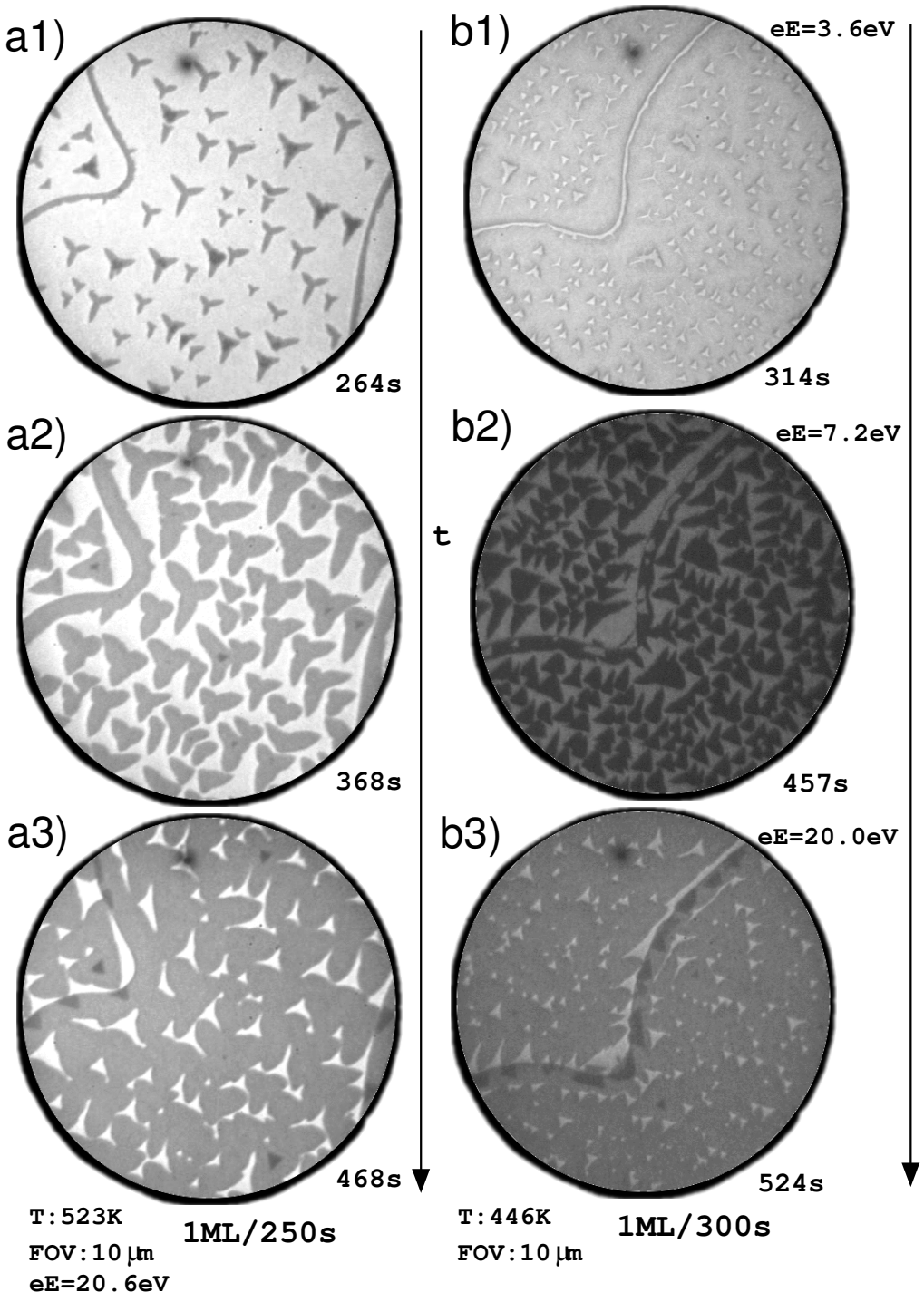

Figure 4.8: LEEM snapshots from movies of the growth of the second layer of Co/Ru. Three frames (n1, n2, n3) are shown in chronological order for each of the two experiments (a and b) represented. Frames a1-a3 are part of the same movie represented in Fig.4.4a. (a1,a2,a3) The 2 ML Co is dark grey and the 1 ML light grey; (b1) The 2 ML Co islands are a little bit brighter than the 1 ML due to different focus conditions; (b2) and (b3) The 2 ML Co is dark grey and the 1 ML medium lighter grey. Note that the electron energy was changed during the movie.

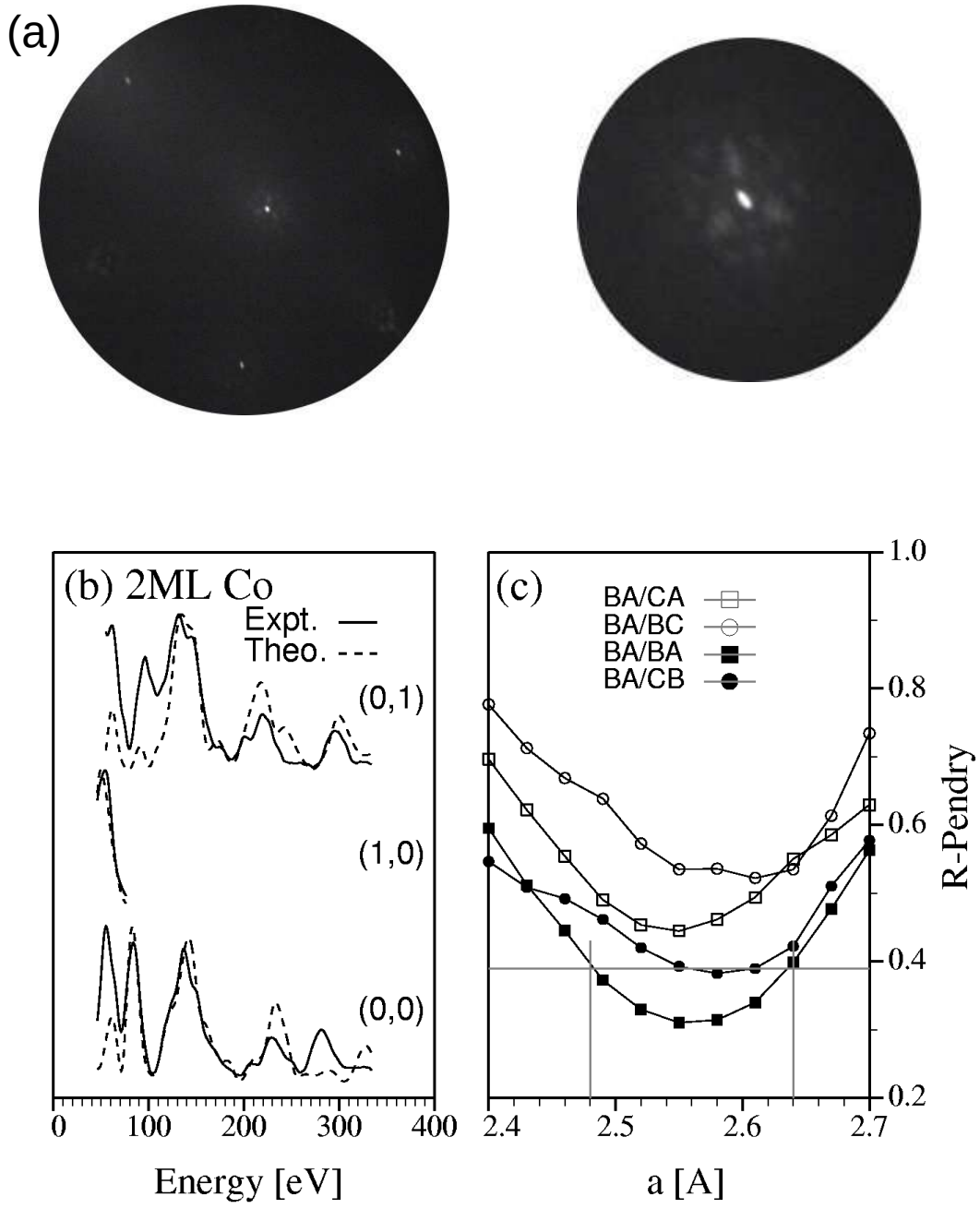

Figure 4.9: LEED of 2 ML Co/Ru. a) Left: pattern at 157 eV showing the integer beams. Right: zoom of the specular spot at 132 eV. b) Experimental and best-fit calculated IV curves. c) Pendry's R-factor, R_P, vs. in-plane lattice parameter of the (1×1) cell, $a_{\|}$, for each of the four possible stacking sequences considered. For each sequence and $a_{\|}$ value, we plot the best R_P value among the rest of the structural parameters. The horizontal grey line corresponds to the R-factor variance for the best-fit stacking sequence, BA/BA or hcp, from which errors on each parameter are estimated.

modelled assuming a common p(1×1) cell. In order to account for the Co/Ru misfit, we let the lattice in-plane parameter vary between the Ru bulk constant ($a_{\parallel}^{Ru}$=2.70 Å) and that of Co-hcp ($a_{\parallel}^{Co}$=2.50 Å). The goal of our fit is not a full simulation of the complete structure, but rather to identify the main stacking sequences present in the film. We have only fit the integer beams (0,0), (1,0) and (0,1) in the analysis. The integration box around each beam was set large enough to include the satellite spots[3].

We note that given the scarce sensitivity of the analysis to the buried Ru, the orientation of the Ru crystal, or more precisely, the actual termination of the Ru terrace: BAB/ or ABA/- could not be determined from the analysis; rotating the Ru crystal but maintaining the same stacking for the Co layers lead to very similar R_P values. Fortunately, the previous 1 ML analysis allows us to determine the terrace termination by also measuring the IV-curves for 1 ML coverage on the same terrace where the data for the 2 ML islands was acquired, and then simply comparing them against the 1 ML curves depicted in Fig. 4.6. Thus, knowing that the Ru surface ends with a BA/ stacking sequence, we explored all four possible registries for the two Co layers: BA/BA, /BC, /CA and /CB. The first two interlayer spacings, d_1 and d_2, were then optimized for each sequence. As stated in section §A-i.2, varying d_3 and d_{bulk} hardly improved the final agreement.

We obtained clearly a better fit for the hcp-type stacking ($R_P^{BA/BA}$=0.31). But we also note from the graph that the fcc BA/CB stacking cannot be discarded; its R-factor is relatively close to the hcp-stacking. Since the Ru terrace termination is common to both minima, one may speculate about the presence of both stackings on the same terrace. In order to simulate such scenario, we have performed weighted mixtures of the IV-curves corresponding to each stacking. For the IV analysis, we set d_1 and d_2 common to both phases, and optimized these two parameters plus the relative weight of each phase, three parameters in total. The best R-factor drops to R_P=0.27 for 70% hcp (30% fcc), suggesting that the hcp stacking coexist with fcc stacking, as expected from the presence of satellite beams in as well as the reported STM observations [94].

The diversity of adsorption sites should be reflected in a large atomic corrugation for this buried Co layer and, accordingly, one would expect a larger averaged d_2 value than the Co bulk distance, d_2=2.04 Å, as it is indeed the case —see Table 4.1. That a larger weight is found for the hcp vs. fcc stackings sequences relative to the underlying Ru can be understood if one assumes hcp stacking to be energetically more favorable than fcc.

[3]For reasons not yet clear to us, the (0,1) beam presented a very attenuated signal for energies above 100 eV and, therefore, we suppressed this range from the analysis

expect a distortion of each moiré pattern, so that the hcp the fcc region. as depicted in

The structural parameters corresponding to the best fit are given in Table 4.1, while the IV-curve experiment-theory comparison is presented in Fig. 4.9b. We feel the agreement is reasonable given the strong approximations involved, which are anyhow reflected in the rather large error bars appearing in the table. We further show in Fig. 4.9c the R_P behavior as a function of $a_{\|}$. The minimum is now attained at $a_{\|}$=2.56 Å. This value is clearly shifted away from the in-plane spacing of 1 ML Co (2.70 Å) but it is approaching the bulk Co in-plane constant, $a_{\|}^{Co}$=2.50 Å. This results show that the Co layer is gradually adopting its own lattice constant. Furthermore, a lateral spacing within the interval $a_{\|} = 2.56 \pm 0.08$ Å is consistent with the observation of a unit cell of 14x14 Co atoms 35 Å in size as reported by STM [94]. That the minimum value is shifted towards a larger lattice spacing can be understood because by design the fit is trying to use a uniform lattice spacing within the film together with a combination of fixed stacking sequences. In a moiré-like pattern, there is an expected change in the lattice spacing from the perfectly substrate-matched fcc or hcp areas of the first Co layer, which should locally present the Ru lattice spacing, towards a more uniform lattice spacing within consecutive layers. An average of such spacings should be between the moiré spacing detected from STM or the LEED satellite spots and the Ru lattice spacing, as obtained in the fit.

The second interlayer spacing, d_2=2.14 Å does not seem compatible with a non-relaxed buried Co layer, for which interlayer spacings of the order of d_2=2.05 Å should be expected in order to conserve the Co atomic volume, as found for the 1 ML case. Therefore, and although not conclusive due to the large error bars involved, the IV analysis also seems to support the picture where the reconstruction for the 2 ML islands involves both Co layers, which then should have the same density. Detailed STM studies for the Cu/Ru system [90] have shown that indeed the case in this related system. By comparison of the Co and Ru binding energies and lattice parameters, and following the argument presented in Ref. [102], one would expect also that both layers are relaxed in Co films. Finally, the appearance of the metastable dislocation network phase for the 1 ML film suggests as well that it can be easily reconstructed.

The result of 2 ML islands is that a combination of stacking sequences are present at the Co/Ru interface, in agreement with the STM reports [94] of a moiré pattern. Within the Co film itself there is only one stacking sequence, within the errors of the fit. This is more obvious in Frank's notation of the determined sequences from the LEED fit, indicating that the termination of the Co film is unique: $\bigtriangledown \bigtriangleup /(\bigtriangledown + \bigtriangleup)\bigtriangleup$.

It is interesting to note that the 2 ML (relaxed) islands are sourrounded by non-relaxed 1 ML film. This implies that the step edge of 2 ML islands is more complicated that a simple type {100} or type {111} step. Although STM experiments would be needed to determine the step edge structure in detail, the experimental result is that the shape of the islands *is* roughly triangular, with the opposite orientation to that of the single monolayer islands grown on the same terrace.

The initial stage of 2 ML island growth presents another structure. At the initial nucleation sites of the 2 ML islands, dark areas can be observed with electron energies between 4 and 5 eV, as shown in Fig. 4.10a. The dark patches get consumed as the growth continues. The number of 2 ML islands with dark patches at their centers is related to the presence of carbon on the surface; islands grown on a more throughly cleaned substrate to remove carbon have fewer 2 ML islands that start with a dark patch, up to the point where it is difficult to find any. To check that those initial regions correspond to 2 ML thick films, we measure electron-reflectivity curves for low energy electrons. Fig. 4.10b shows results from three different surface types: 1 ML film, 2 ML (-regular triangular island), and a patch of dark region at the center of a 2 ML island. The reflectivity curve for each area is shown in Fig. 4.10c. The dark region 2 ML-area IV curve is identical in shape, albeit with less overall intensity, to the triangular 2 ML island. In contrast, the 1 ML area is different. This indicates that the thickness of the dark patch is the same as the rest of the 2 ML islands. The difference in contrast could be due to a different stacking sequence, or to a different structure. The ideal way to distinguish between those possibilities would be to measure the LEED pattern of each region. The dark areas, though, are too small to obtain LEED patterns from them (the minimum spot size for a full LEED pattern in our instrument is close to 2 μm). A different way of obtaining diffraction information is to perform dark-field imaging: using a very small aperture located at the back-focal plane of the objective to block all electrons but those of a given diffracted beam from which the real space image is formed [51] (dark-field). In this way we determine that the dark patches present no intensity at the superstructure satellite beams. This rules out that the dark areas present the same structure as the rest of the 2 ML islands. Our tentative conclusion is that they are pseudomorphic areas, probably stabilized by segregated carbon. Nevertheless, they could correspond to another structure that does not present diffraction spots at the location of the satellite spots from the rest of the 2 ML Co islands. The 2 ML dark regions become smaller as the 2 ML islands continue to grow. If the growth is stopped, they are not removed. In 2 ML islands that have dark patches, the dark regions serve as nucleation centers for the third Co layer.

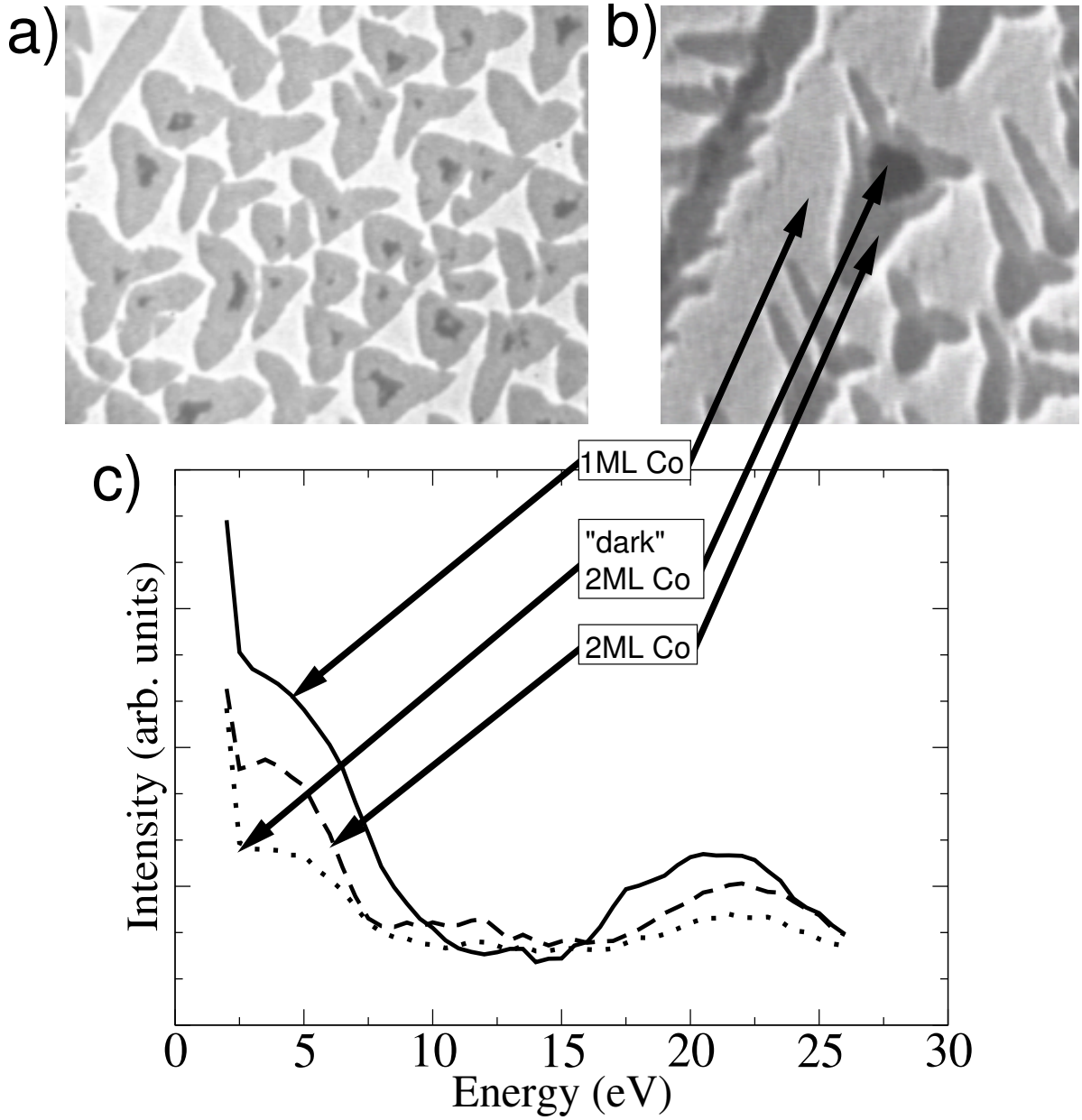

Figure 4.10: a) LEEM image of 2 ML islands of Co onto one complete monolayer of Co on Ru. The growing conditions are: a) FOV=4.8x4.3 μm, T=363 K, flux=1ML/360 s, eE=4.2 eV, deposition time 490 s. 2 ML Co is medium (and dark) grey and 1 ML appears light grey. We suggest that the dark grey regions are pseudomorphic 2 ML Co. The rest of the islands (medium grey) is relaxed 2 ML Co. b) Higher magnification LEEM image. c) Plot of the reflectivity versus energy of the regions indicated in b).

4.2.3 The third monolayer

The third monolayer also grows in triangular islands (Fig. 4.11). The sides of the islands are now mostly straight. Unlike in previous films, triangle-shaped islands with two (opposite) orientations are now simultaneously present on each terrace (Fig. 4.12a). The presence of both orientations on a given terrace is naturally explained by assigning each orientation to a different stacking sequence. That is, exposing the same step edge —type {100}— requires islands with different orientation depending on the stacking (see Fig. 4.12c,d) This effect has been used as a fingerprint of stacking fault presence in other systems such as Co on Cu(111) [84], or Ir/Ir(111) [103].

We also note that for films which are three layers thick we can describe univocally their stacking sequence as fcc or hcp, independently of their registry with the Ru substrate. Not taking into account the presence of a moiré-like structure at the Co/Ru interface, we would naively assign one island population to the hcp stacking sequence, as that population inverted their orientation relative to islands one layer thinner (as suggested by Frank's notation of a hcp stacking sequence $\triangle \bigtriangledown$ ...). The rest of the islands would be assigned an fcc stacking by the same argument. Surprisingly enough, this guess of the stacking sequence within the Co film is actually confirmed by selected-area LEED measurements, as described below.

At particular electron energies, like 20 eV and 48 eV, the specular reflectivity of islands with opposite orientations differs. For example, in the images taken at 20 eV all the islands with one orientation appear dark grey, while islands in the opposite orientation appear light grey (Fig. 4.12b). The difference in contrast allows the local evolution of the stacking type to be followed from isolated islands to a continuous film. The persistence of this difference reveals the presence of the two types of regions - with different stacking sequence- even in areas where the material grows from steps (step-flow, lower part of Fig. 4.12ab). The contrast difference is neither removed when the islands coalesce nor when heating the sample below the alloy-formation temperature. It arises from differences in intensity for the specular beam between both types of regions. The same effect was found between stacking-sequence domains at the second layer of Cu on Ru(0001) [51]. An enhanced contrast may be achieved by inspecting the non-specular integer spots. We note that at 40 eV the (01) beams are much more intense than the (10) in islands of one orientation. The reverse is true for the other opposite oriented islands, giving strong contrast in dark-field imaging similar to the one observed between twins in systems such as Au on mica by transmission electron microscopy (TEM [104]).

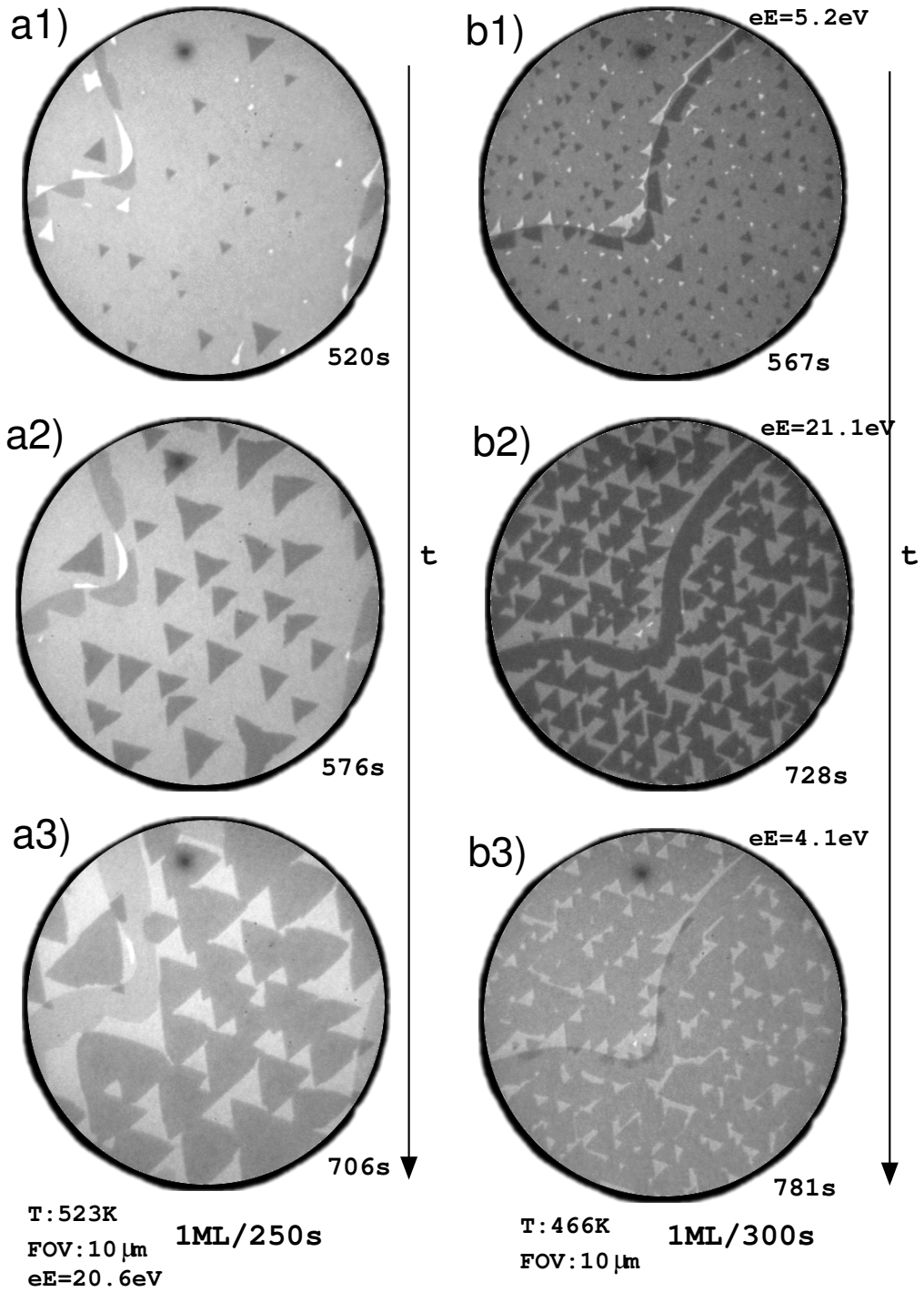

Figure 4.11: LEEM images from movies of the growth of the third layer of Co/Ru. Three frames (n1, n2, n3) are shown in chronological order for each of the two experiments (a and b) represented. Both a) and b) are part of the same movie represented in Fig. 4.8a,b. Experiment a) also appears in Fig. 4.4a. a) 3 ML Co is dark grey and 2 ML is medium grey. Note that the two grey levels in the 3 ML areas is attributed to different stacking sequences. White regions are 1 ML Co; (b1,b2,b3) 3 ML Co islands are dark grey and 2 ML areas are medium grey.

Note that this dark-field contrast is reversed when going from one substrate terrace to the next in line with the orientation reversal of the island shape at consecutive terraces as shown in Fig. 4.12f. On the other hand, in the specular beam contrast there is no reversal from terrace to terrace (compare Fig.4.12e and f).

To confirm the stacking-fault origin of the contrast between islands oriented in opposite directions in the same terrace, we measured LEED patterns and IV curves from each type of region when the film is close to three complete monolayers. The diffraction patterns show, as in 2 ML areas, satellite spots indicating that the film is relaxed in-plane - i.e., reconstructed. Following the same procedure used for 2 ML islands, the integer beam IV-curves were obtained integrating the intensity within a box large enough to include the satellite beams. We again found, for both phases, unexpected attenuated experimental intensities for the (01) and (10) beams for energies above 100 eV.

We then simulated the IV spectra for a 3 ML thick Co film on top of the Ru(0001), again assuming a common p(1×1) cell for all layers. We explored the eight possible stackings for the three Co layers: BA/BAB, /BAC, /BCA, /BCB, /CAB, /CAC, /CBA, /CBC, varying the in-plane lattice parameter, $a_{\parallel}$, and the first two interlayer spacings. The Ru terrace termination was again fixed to that determined from the 1 ML case. The results of the R-factor analysis performed independently for each region are presented in Fig. 4.13d,f as a function of $a_{\parallel}$. Two very similar minima well below the rest appear in each graph: $R_P^{BA/CBA}$=0.32 and $R_P^{BA/BAC}$=0.37 for region I and $R_P^{BA/CBC}$=0.29 and $R_P^{BA/BAB}$=0.30 for region II. Using Frank's notation region I is $\bigtriangledown\bigtriangleup/(\bigtriangleup+\bigtriangledown)\bigtriangleup\bigtriangleup$ and region II is $\bigtriangledown\bigtriangleup/(\bigtriangleup+\bigtriangledown)\bigtriangleup\bigtriangledown$. By noting that each pair of minima correspond to very similar $a_{\parallel}$ values, and that they share the same relative registries among the the three Co layers -i.e., they only differ in the relative stacking of the film with respect to the Ru (as it is highlighted by Frank's notation), we can assign fcc stacking to region I and hcp stacking to region II, confirming the island shape argument. Thus, a keypoint is that the two regions differ in how the third Co layer is stacked on the second layer: a stacking fault occurs between the second and the third layers. The existence of two minima per region suggests that each 3 ML region presents two stacking sequences relative to the underlying Ru, as expected from the moiré-like LEED pattern. Mixing the two minima led to marginal improvements at both regions: R_P=0.31 for I and R_P=0.28 for II.

We provide in Table 4.1 the optimized structural parameters for the BA/CBA and BA/BAB stackings, while their corresponding IV-curves are shown in Fig. 4.13c-d. The parameter values corresponding to the other two minima, BA/CBA and BA/CBC are basically coincident with the former. The optimized $a_{\parallel}$ values, $a_{\parallel}^{BA/CBA}$=2.54 Å and

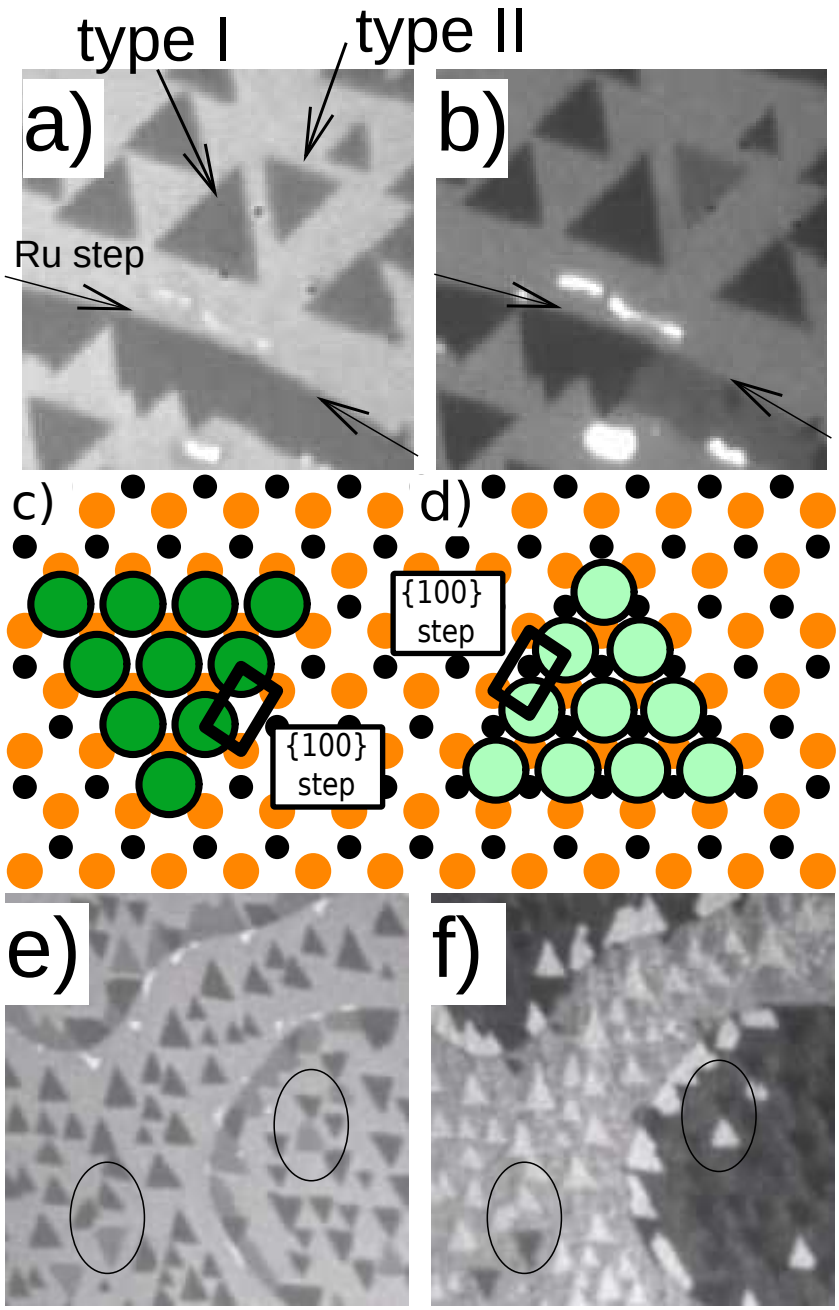

Figure 4.12: a)-b): Experimental observations of triangular islands with opposite orientation on 3 ML Co. The size is 2.1μm×1.7μm. eE is 5 eV and 20 eV respectively. c)-d) Schematic of two triangular islands on an hexagonal substrate. c) The substrate and the island are hcp and the favored microfacet is {100}. d) If the island has an stacking fault, i.e. the atoms are located at fcc adsorption sites, to expose the same step edge the shape will have to be inverted. e)-f) Same area observed in bright field e), i.e. using the specular beam, and in dark-field using one of the first order Co beams f). The contrast in dark-field e) and the orientation of the same type of island reverses when crossing a substrate step. The contrast does not reverse in bright field f).

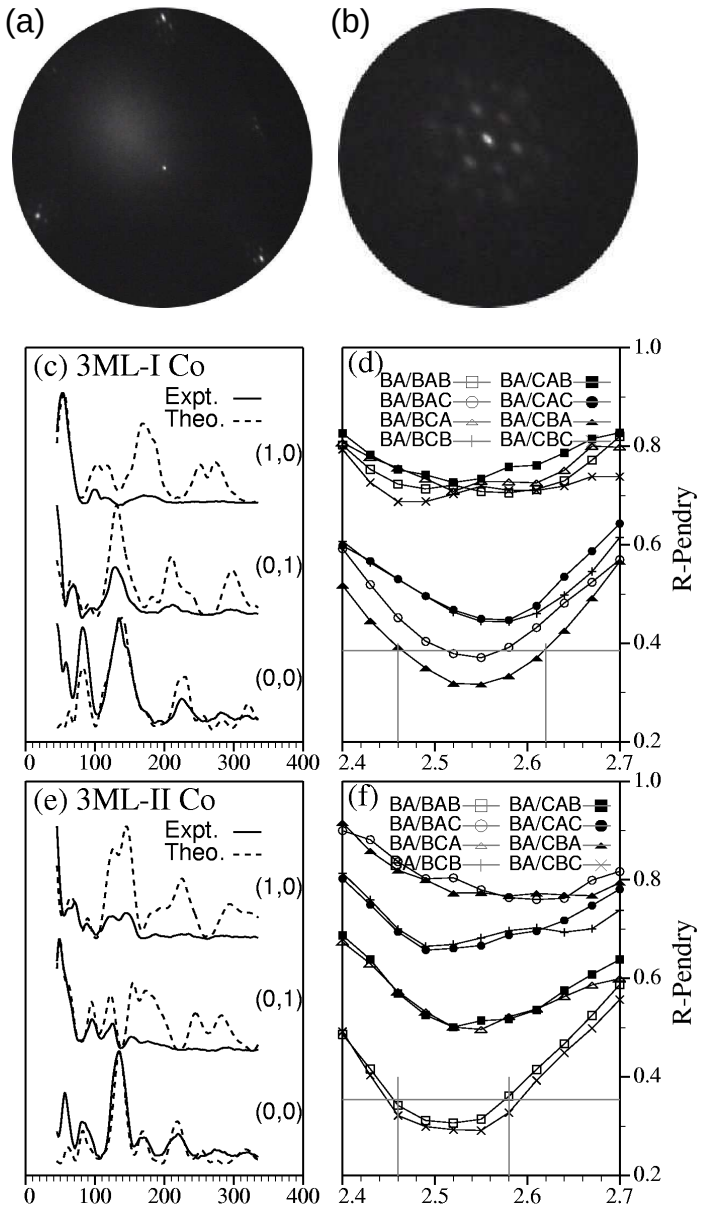

Figure 4.13: LEED of 3 ML Co/Ru. a) 55 eV LEED pattern of the domain pattern of the islands that appear dark grey (region I) in Fig.4.12a. b) Zoom of the specular beam of the same domain, at 132 eV. c) and e) Experimental and best fit calculated IV curves for region I (BA/BCA or fcc stacking) and region II (BA/BAB or hcp stacking), respectively. d) and f) Pendry's R-factor, R_P, vs. in-plane lattice parameter of the (1×1) cell, $a_{\|}$, for region I and region II, respectively. We include in each graph the eight possible stacking sequences considered. For each sequence and $a_{\|}$ value, we plot the best R_P value among the rest of the structural parameters. The horizontal grey line corresponds to the R-factor variance for the stacking sequences, BA/CBA and BA/CBC, from which errors on each parameter are estimated.

$a_{\parallel}^{BA/BAB}$=2.52 Å, confirm the evolution towards the bulk Co(0001)-p(1×1) spacing. If we again invoke conservation of the Co atomic volume, the structural parameters reported in Table 4.1 are consistent with a fully reconstructed film; the second interlayer spacings, d_2, are clearly smaller than that found for the 2 ML coverage, attaining values consistent with the ideal bulk Co stacking. Hence, it is likely that *all* Co layers in films thicker than 1 ML are reconstructed, i.e., no layers are pseudomorphic with the substrate.

Below the alloying temperature we have not observed any change in the stacking structure of a complete 3 ML film as monitored by the reflectivity of the specular beam. This is true even after growing additional material. This lack of evolution of the two populations with different third layer stacking sequence is in contrast to other reported systems such as Cu/Ru(0001) [51], Ir/Ir(111) [105, 106], or Ag/Ru(0001) [107] where stacking faults were observed to heal out either by themselves through activated processes, or through further growth of additional layers (Ag/Ru).

We next address the origin of the coexistence of two types of regions. The ratio of both type of islands depends very clearly on whether the islands grew from underlying Ru step edges by step-flow, or they nucleated in the middle of terraces. Fig. 4.12 shows both types of areas. A suggestion to explain this difference is that the presence of the step replicated from the Ru-substrate in the growing film favors an hcp stacking sequence that can match the step-edge without additional dislocations. STM experiments will be required to confirm this idea. Fig. 4.14 shows two growth experiments of Co films on Ru at 471 K (a) and 438 K (b). The proportion of both kinds of islands is summarized in Table 4.2. At 471 K half of the Co that grow in step-flow fashion is fcc (lower part of Fig. 4.14a) and the other half is hcp; at 435 K all the step-flow Co is hcp (Fig. 4.14b). The

The ratio of fcc to hcp islands nucleated away of the substrates steps, on a terrace, is very sensitive to the overall cleanliness of the experiment. If the Co-deposition and the LEEM measurements are done at total pressures below 5×11^{-11} torr the 3 ML islands grow mostly with an hcp stacking— i.e. opposite orientation in 3ML islands compared to 2 ML islands that appeared before on the same terrace, as can be seen in Fig. 4.15c,d. 4 ML island-triangles in turn point mostly in the same direction as 3 ML islands —fcc stacking. If the pressure during deposition is higher the orientation of most of the 3 ML islands is the same as for 2 ML islands, and the same happens for thicker films (Fig. 4.15a,b), implying fcc stacking above 2 ML. These findings suggest that the transition from hcp to fcc occurs at 3 ML, unless the film is extremely clean, in which

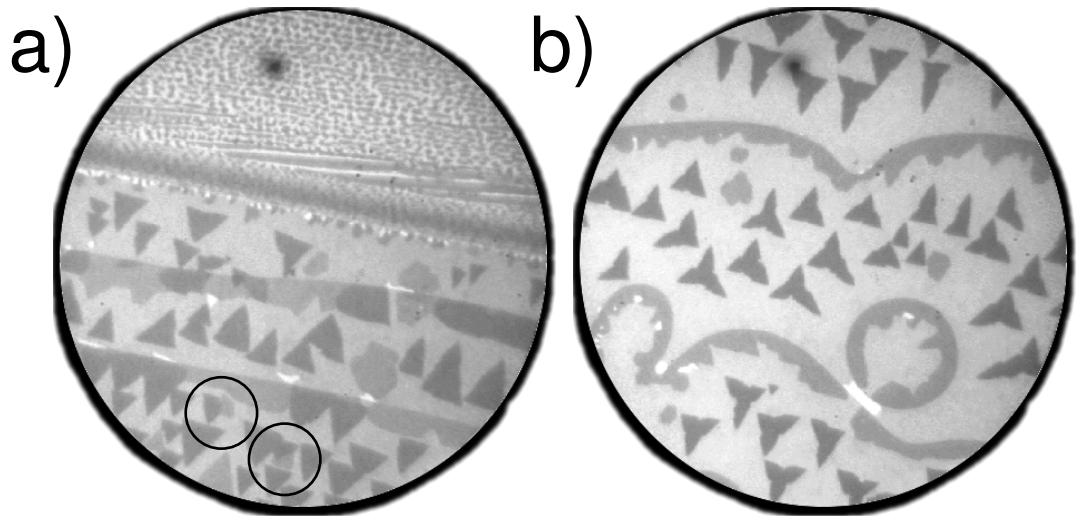

Figure 4.14: LEEM images of 3 ML Co islands on 2 ML Co/Ru. a) FOV=10 μm, T=471 K, flux=1ML/210 s, eE=21.6 eV. The 3 ML Co is dark grey for SF (majority), medium grey for regular hcp islands (minority), light grey for 2 ML and white for 1 ML. The total coverage is 2.47 ML. This image shows the border of a extremely flat valley, that is surrounded by steps with common density. In the stepped region the Co growth in Stranski-krastanov mode. We can see in the image that this region have only 1 and 3 ML of Co (dark grey islands on white layer). On the other hand, the flat region have only two monoatomic steps in more than 5 μm distance. The black circles indicate the two cases in which SF and regular islands have coalesce. b) FOV=10 μm, T=438 K, flux=1ML/210 s, eE=20.5 eV. The brightness legend is the same than in a). The coverage is 2.37 ML.

T (K)	Coverage[4] (ML)	Islands founded	Search area (μm^2)	fcc islands	hcp islands
471	2.47±0.05	1934	5340	1776(91,8%)	158(8.2%)
471	2.47±0.05	step-flow	-	(∼50%)	(∼50%)
438	2.37±0.05	819	5969	670(81,8%)	149(18.2%)
438	2.37±0.05	step-flow	-	(∼0%)	(∼100%)

Table 4.2: Regular (hcp) and SF (fcc) islands statistics for 3 ML Co islands on 2 ML Co/Ru(0001) at two temperatures.

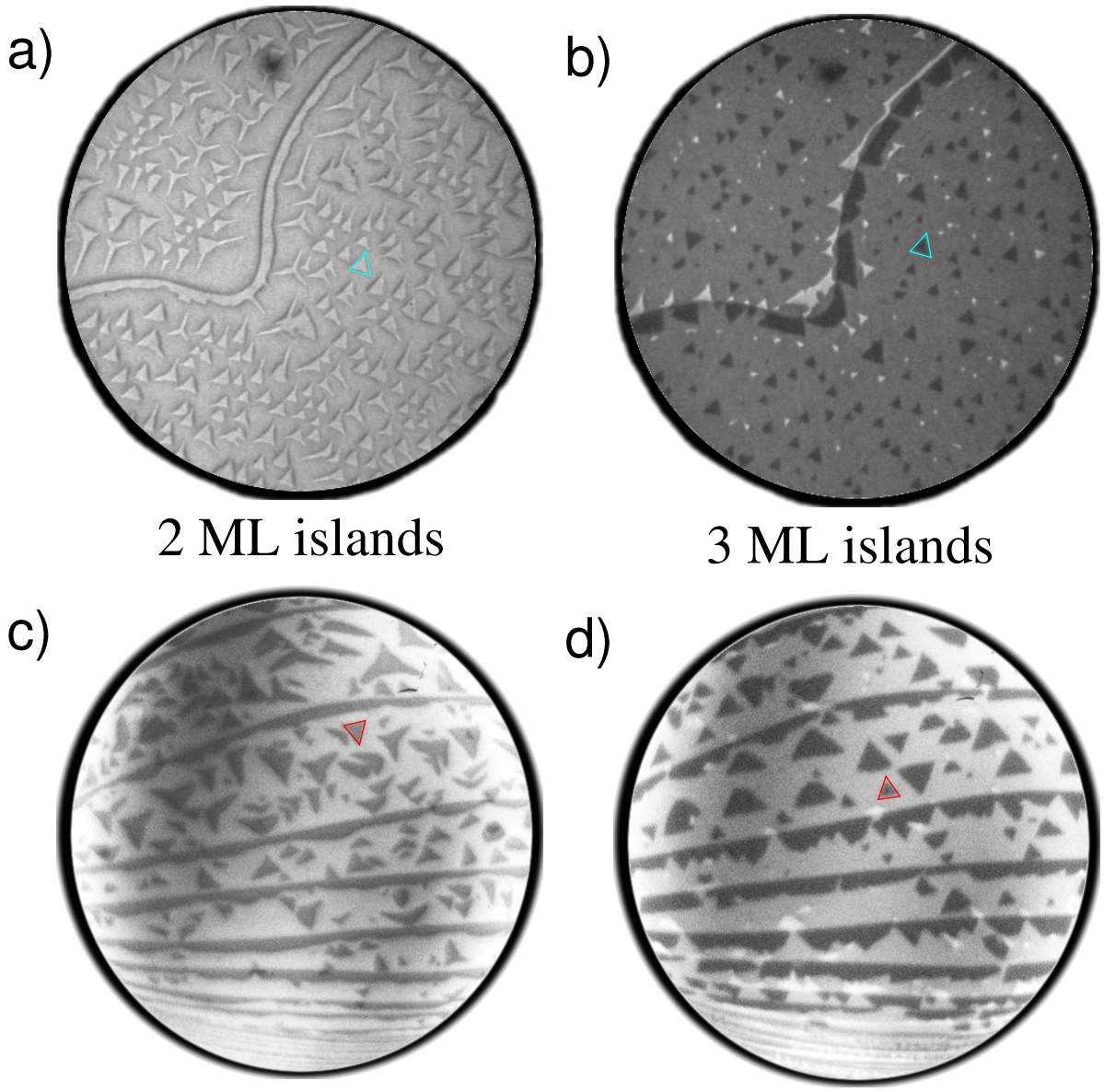

Figure 4.15: Comparison of triangle orientation with different background pressures and similar conditions (growth rate and temperature are 1 ML/220s and 515 K respectively). Color triangles mark the most common orientation. a)-b) Background pressure 4×10^{-10}torr (FOV 10 μm, eE=20 eV). c)-d) Background pressure in the 10^{-11} torr range (FOV 7 μm, eE=7 eV).

case the transition is delayed until 4 ML. This observation hightlights the strong effect that even minute amounts of adsorbates can have on the stacking fault probability.

That Co fcc is preferred for thicker films is surprising given that the most stable bulk-Co structure below 690 K is hcp. Nevertheless we note that the same result, i.e. mostly fcc films, was reported on the growth of Co on Pt(111) [89, 108].

4.3 Conclusions

In summary, we have studied the growth of the first few layers of Co on Ru(0001) by means of LEEM, LEED and dynamical IV calculations. The large terraces found in the Ru substrate allow Co to grow layer-by-layer despite the large difference in in-plane lattice parameters. We show in Figure 4.16a an schematic of the structures derived in the present work. The first layer grows pseudomorphically and continues the hcp stacking sequence of the Ru(0001) substrate. The shape of the islands is triangular, exposing {100}-type steps, and the orientation rotates 180° in consecutive terraces, as expected from the hcp substrate. Thicker films reconstruct in order to recover the Co bulk in-plane lattice constant, yielding satellite spots in the diffraction patterns. For these coverages, and although at the limit of our sensitivity, best IV fits are always obtained for weighted mixtures of hcp and fcc stackings between the bottommost Co layer and the topmost Ru layer. The coexistence of two such stacking sequences may be rationalized after the STM observations of Co films [94] where, after taking the substrate-adatoms interactions into account, we expect to predominantly have both atoms with hcp and with fcc stacking. The second layer of Co also forms triangular-like islands. The orientation now is inverted with respect to the 1 ML, and there is only one stacking sequence within the film itself. The third layer grows again in triangular islands, but this time present islands with two orientations. By selected area LEED IV-analysis, we confirm the correspondence between island orientation and stacking-sequence in the 3 ML islands: the two regions experimentally detected correspond to the two possible stacking sequences of the 3^{rd} layer on top of the 2 ML film. The knowledge of the stacking and island shape structure revealed here, along with the interesting magnetic properties [11] of the first layers and the limited intermixing, makes the Co/Ru system an excellent combination for basic and applied material research studies. In the future we expect to complement the data presented here with full IV analysis, including satellite spots, of the thicker films.

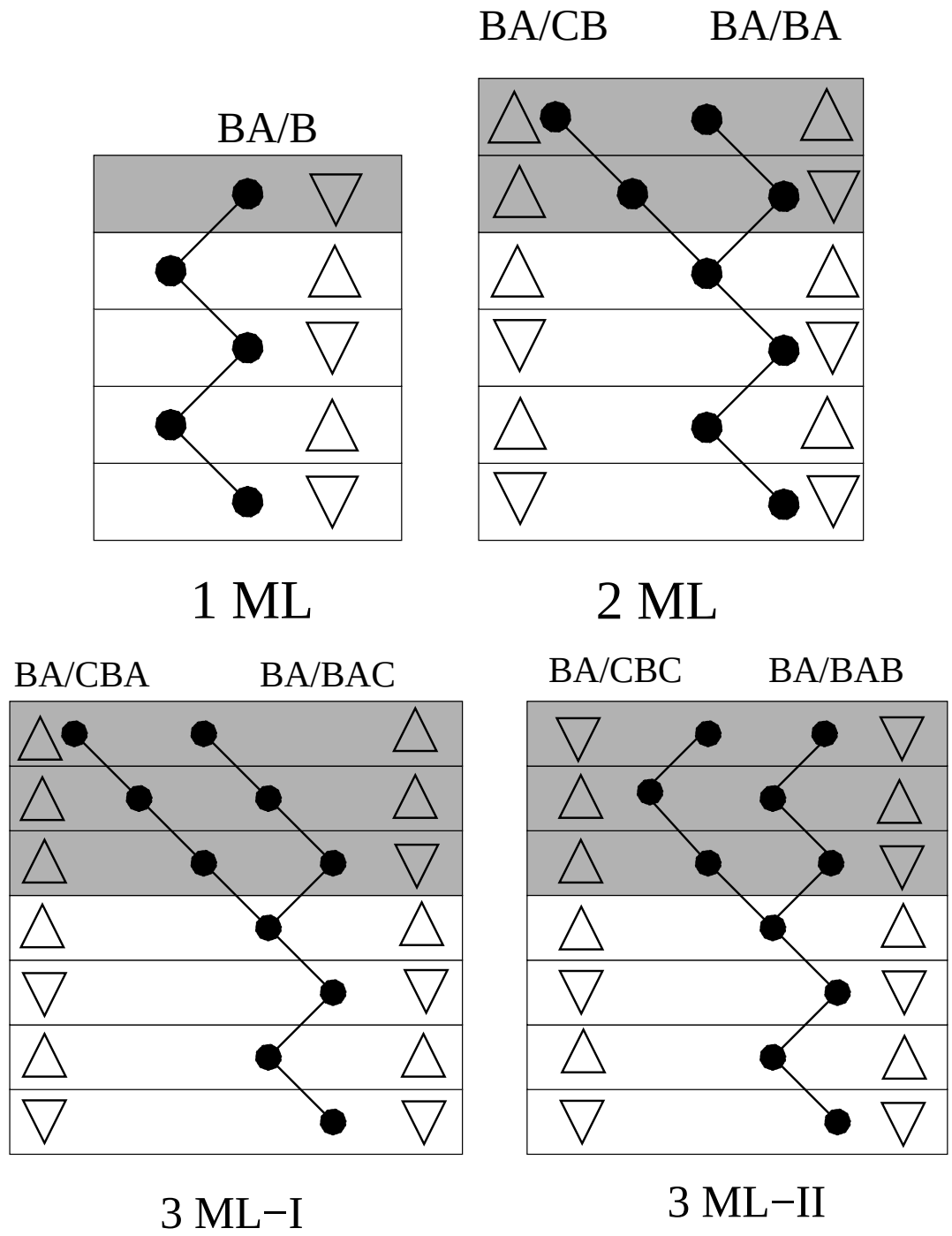

Figure 4.16: a) Cross sections of the stacking sequences, both in ABC and Frank's notations as derived from the IV-LEED analysis. For coverages above 1 ML, the film is reconstructed and two relative registries between the deepest Co layer and the first Ru layer coexist. Note that the orientation of the triangles in Frank's notation follows that experimentally found for the triangular islands. In 3 ML films, regions I and II differ only in the stacking of the third Co layer. coexistence of both split into two hcp stacking for the hcp edges of the stacking

Chapter 5

Cobalt on Ruthenium (0001): Imaging the Magnetic Structure

"In the future,... people will live twice as long, computers will die twice as fast."
— Futurama website

By means of spin-polarized low-energy electron microscopy (SPLEEM), we show that the magnetic easy-axis of one to three atomic-layer thick cobalt films on ruthenium crystals changes its orientation twice during deposition: one-monolayer and three-monolayer thick films are magnetized in-plane, while two-monolayer films are magnetized perpendicular. The Curie temperatures of films thicker that one monolayer are well above room temperature. Fully-relativistic calculations based on the Screened Korringa-Kohn-Rostoker (SKKR) method demonstrate that only for two-monolayer cobalt films the interplay between strain, surface and interface effects leads to perpendicular magnetization.

5.1 Introduction

Applications of ferromagnetic films depend on understanding and controlling the direction of the easy-axis of magnetization. In particular, magnetization perpendicular to the film plane [18, 109, 110] holds promise for novel information-processing technologies [111]. Two important features of ultra-thin films underlie this technological achievement: the

large Curie temperature of transition metal films and the ability to control their microstructure. To provide deeper understanding, we study thin-film magnetism in a system whose components do not intermix, Co and Ru. Previous work [5, 6] has shown that the easy axis of magnetization in Co/Ru multilayers changes from perpendicular at low Co thickness to in-plane for films thicker than 7 ML [7]. Because the Co films did not grow layer-by-layer [8, 9], the films contained islands of varying thickness. Under these conditions, determining precisely how the magnetization changes as a function of film thickness is quite problematic.

Here we deposit Co films under conditions of perfect layer-by-layer growth. Then we use in-situ spin-polarized low-energy electron microscopy (SPLEEM) [2, 3, 66] to locally determine the magnetization orientation of one-, two-, and three-monolayer thick Co films. We observe that the easy axis of magnetization changes after the completion of each atomic layer. By combining structural, morphological and microscopic magnetic measurements with fully relativistic ab-initio calculations based on the screened Korringa-Kohn-Rostoker (SKKR) [112] method, we explain the origin of the magnetization changes. Our results highlight that the magnetic anisotropy of ultra-thin films is not necessarily simply assigned to strain or interface effects.

5.2 Growth and Structure of the First Co Layers onto Ru(0001): Summary

The films are grown in two different ultra-high vacuum low-energy electron microscopes (LEEM and SPLEEM) [2] by physical vapor deposition from calibrated dosers at rates of 0.3 ML/min. Perfect layer-by-layer Co growth occurs up to at least 7 ML when the Ru substrate has a low density of atomic steps (summary on Fig.5.1a-c, full details on chapter 4). Because substrate steps enable a kinetic pathway to the nucleation of new film layers, three-dimensional growth [7, 8] occurs after the first monolayer if substrate steps are present at even moderate density [92]. The film structure is determined by selected-area low-energy electron diffraction (μLEED), i.e., the diffraction patterns were acquired with diffracted electrons coming from areas of the film with uniform thickness. One-monolayer films always present a 1×1 LEED pattern indicating pseudomorphic growth, that is, the film has the same in-plane lattice parameter as the substrate (Fig. 5.1d). Since the in-plane lattice parameter of bulk Co is 7.9 % smaller than that of Ru, both measured within the hexagonal-close-packed (hcp) basal plane, the first monolayer of

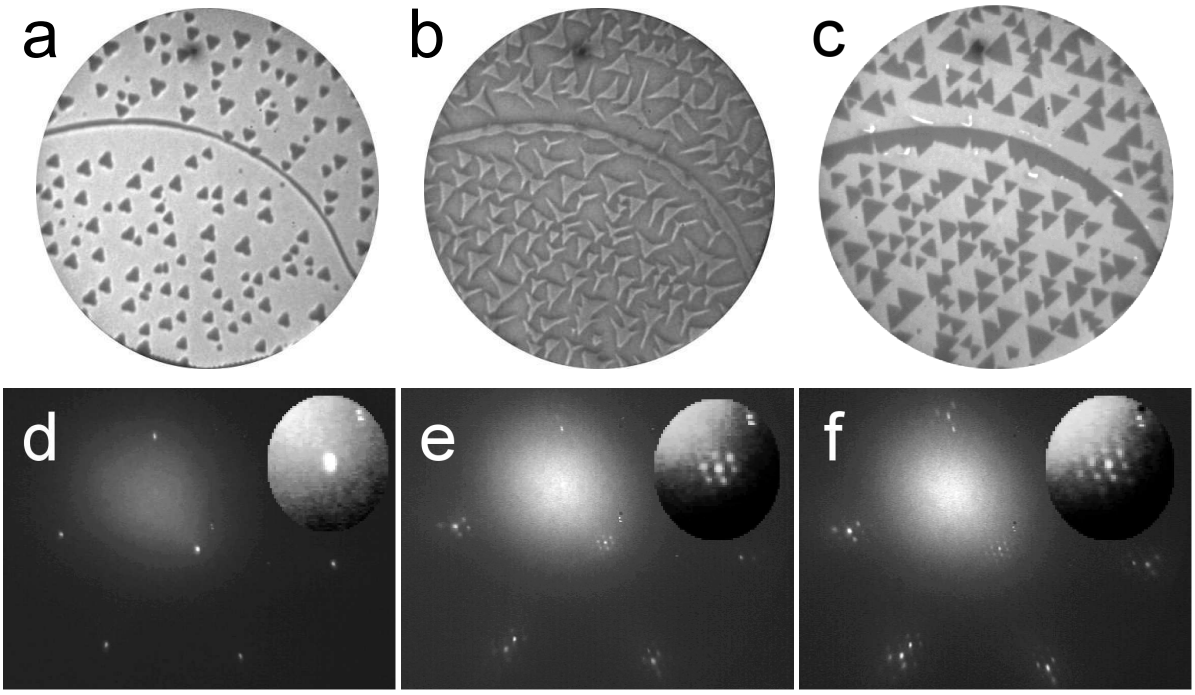

Figure 5.1: LEEM images and diffraction patterns of a Co film growing on Ru(0001). a)-c): LEEM images show the morphology of the growing film. Field of view is 10 μm, electron energy is 5 eV, and growth temperature is 460 K. One single, curved Ru step crosses the images. a) 1 ML Co islands (dark) on Ru (light grey background). b) 2 ML islands (light grey) on a complete 1 ML film (dark grey). c) 3 ML islands (dark grey) on a nearly complete 2 ML film (light grey). d)-f) LEED patterns (70 eV) obtained from selected film areas of uniform thickness. Insets show magnified views of the specular beam. d) 1 ML , e) 2 ML and f) 3 ML of Co/Ru(0001).

Co is under pronounced tensile strain. Analysis of the intensity versus energy curves of the specular and integer diffraction spots establishes that the Co film continues the hcp stacking [93] (Chap. 4) of the substrate, with a Co-Ru interplanar separation estimated to be contracted 4% relative to the Ru-Ru interplanar spacing. For films thicker than 1 ML, satellite spots appear around the bulk diffraction beams (Fig. 5.1e-f), i.e., the thicker films are no longer pseudomorphic. The in-plane spacing of 2 ML and 3 ML Co films is 5±1 % less than the Ru spacing, leaving the film strained only by 3 % relative to the bulk-Co value. At intermediate coverages between 1 ML and 2 ML, the 1 ML areas are still pseudomorphic, as detected by dark-field imaging, while 2 ML islands are relaxed and 3 ML films grow mainly in a face-centered-cubic structure.

5.3 Growth of the First Co Layers with Magnetic Contrast

To study the magnetization during the growth of Co films on Ru(0001) we measured the process in real time with the SPLEEM. As explained in section 2.2.1 it is necessary to make an electron energy scan in order to optimize the magnetic contrast of the SPLEEM for an specific film. Fig 5.2 shows the reflectivities obtained in an SPLEEM energy scan performed at perpendicular polarization for 2 ML Co/Ru(0001). The dashed line shows the difference between reflectivities, i.e the contrast. The maximum contrast for the Co/Ru system is at $\sim$7 eV.

We have grown up to 3.5 ML of Co on Ru(0001) at 511 K. At this temperature Co grows layer-by-layer by means of coalescing triangular shaped islands and some step flow material, as we already show from chapter 4. All the changes in the structure and in the in-plane magnetization during growth where recorded in real time with the SPLEEM. Fig. 5.3 shows an image sequence of the process, composed of couples of LEEM and in-plane polarization SPLEEM images[1]. The time since the start of the Co deposition is indicated at the right of each SPLEEM image. LEEM images (left row) show the topography of the surface during Co growth. Different contrast regions correspond to different thicknesses and/or composition of that region (indicated by arrows in the LEEM images). SPLEEM images (right row) show the in-plane magnetization of the surface. White regions are magnetized 13° off a compact-direction. Black regions are magnetized also in-plane but pointing in the opposite direction.

In Fig. 5.3, the SPLEEM images measured at 144 and 693 s from the start of Co deposition show that there is no in-plane magnetic contrast at 511 K for 1 and 2 ML Co/Ru. The SPLEEM image taken at 1073 s shows that the islands of 3 ML Co/Ru(0001) are magnetized in-plane at 511 K. The SPLEEM image taken at 1529 s shows that a film composed of 3 complete monolayers of Co plus some 4 ML islands is completely magnetized in-plane at 511 K.

In the following experiments, in order to study in depth the magnetic structure of the first tree monolayers, we will stop the growth at the desired film thickness and measure three orthogonal components of the magnetization to completely resolve it in space. We will cool down the sample (110 K) when needed in order to measure the magnetization direction of films with a Curie temperature bellow room temperature.

[1] In-plane and 13° off a compact-direction.

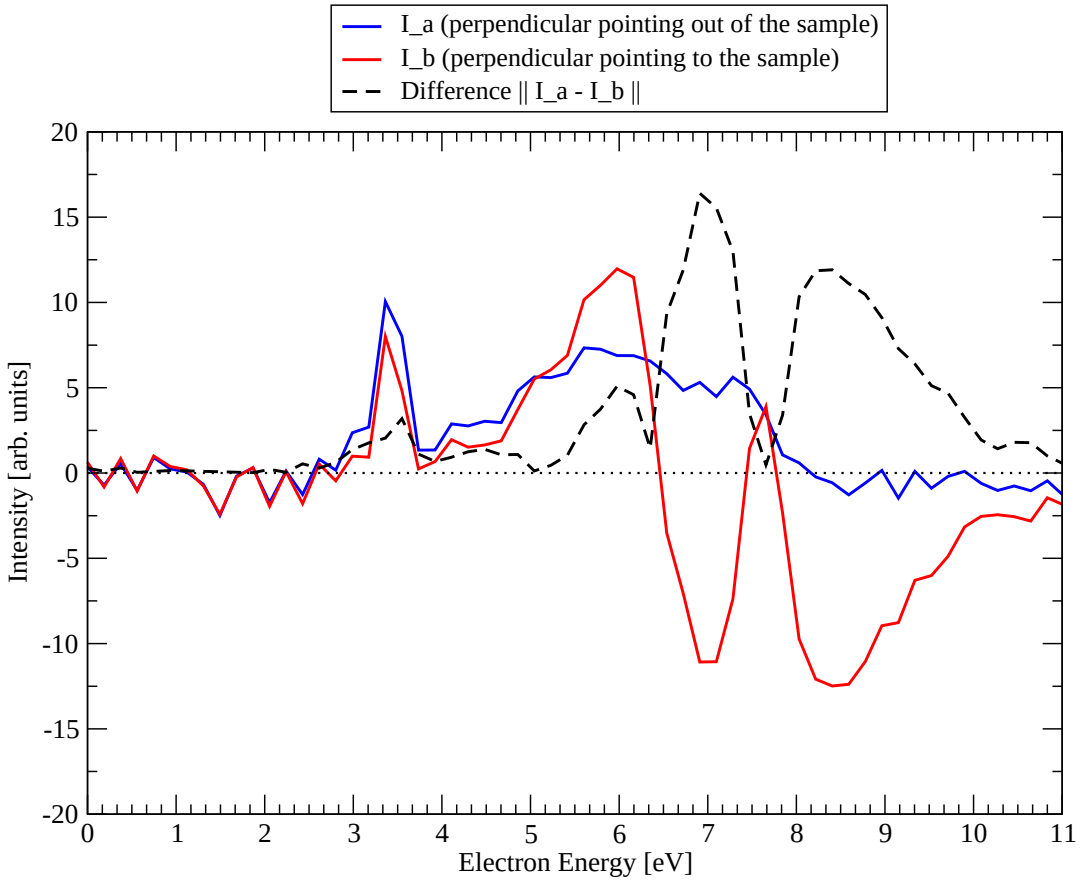

Figure 5.2: Reflectivity versus electron energy (eE) curve for perpendicular magnetization for a film composed of 2 ML Co/Ru(0001) at room temperature. Blue (red) curve represents the reflectivity of a region of the surface with the magnetization perpendicular pointing out of (to the) the sample. Dashed line represent the difference between both reflectivities (i.e. the contrast). The electron energy scan was measured from 0 to 11 eV in 0.2 eV steps. Below 3 eV the SPLEEM is in MEM mode and there is no magnetic contrast. The strongest contrast is obtained around 7 eV, where the difference between both reflectivities is maximum.

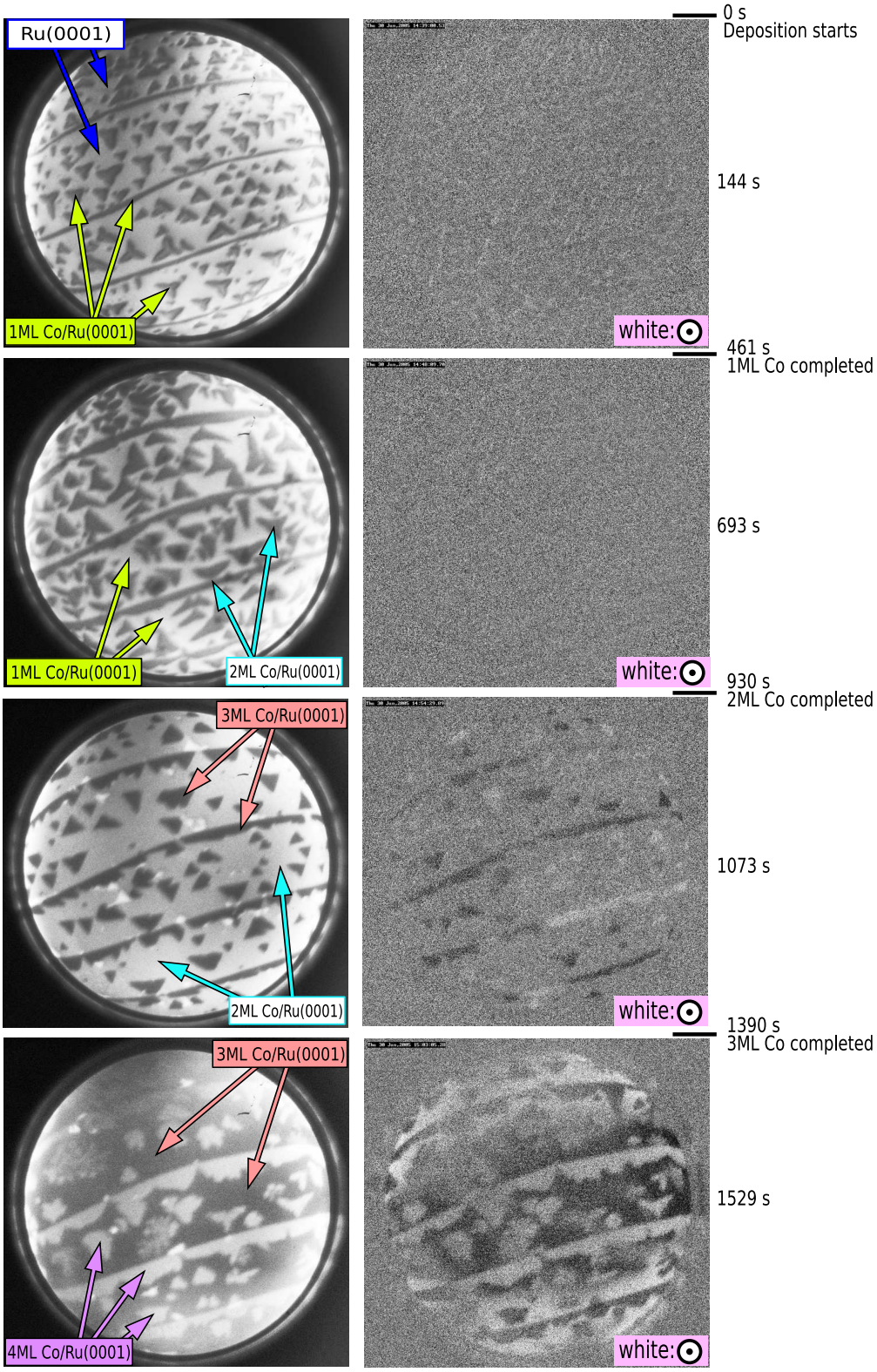

Figure 5.3: LEEM and in-plane SPLEEM image sequence of the growth of 3.5 ML of Co on Ru(0001). FOV is 7 μm, eE is 5.3 eV and the temperature 511 K. The Co deposition ratio is around 1 ML/460 s. (See text for further details).

5.4 From 1 ML to 3 ML: the Spin Reorientation Transitions

In Fig. 5.5 we show LEEM and SPLEEM images of a film that consists of a complete monolayer of Co plus some second layer islands (Fig. 5.5a), both in the middle of the substrate terraces and at the bottom of the ruthenium substrate steps. The SPLEEM images taken at 110 K show the spatially resolved component of the magnetization in three orthogonal directions: two in-plane (Fig. 5.5b-c) and one perpendicular (Fig. 5.5d). In one-monolayer areas the magnetization is oriented in the plane of the film, while for two layer islands the magnetization is perpendicular. For a complete 2 ML film with additional 3 ML islands (Fig. 5.6), the magnetization of the 2 ML areas is perpendicular. In contrast, 3 ML thick islands and thicker films (not shown) are magnetized in-plane. To summarize, two magnetization easy-axis reorientation transitions are found in three consecutive atomic layers: at the crossover between 1 and 2 ML, and between 2 and 3 ML. This behavior has also been confirmed in films devoid of islands. The Curie temperature of the films changes dramatically from the first layer to the second. The first layer has a Curie temperature close to 170 K, as detected by the loss of magnetic contrast in the 1 ML areas. The Curie temperature of the 2 ML islands, which are magnetized perpendicular, is well above room temperature, about 470 K (Fig. 5.4). Thicker films exhibit Curie temperatures above 470 K. Iron films on W(110) [113, 114] also present a double spin reorientation transition, but with a Curie temperature well below room temperature for perpendicular magnetization [115].

Fig. 5.6 shows fcc and hcp islands of 3 ML Co/Ru(0001). We can resolve the stacking by simply looking to the island orientation in a single terrace (see section 4.2.3). For example, in the left half of Fig. 5.6b there is a big white triangle pointing in certain direction, and a small one above it pointing in the opposite direction. All the step flow material is always hcp below 438 K (see Table 4.2). The big white triangle points in the opposite direction: it has fcc stacking. The small one above has hcp stacking. Both stackings are perpendicularly magnetized with equivalent magnetic contrast.

5.5 *Ab-initio* Calculations

To understand the effects that give rise to the observed changes in the orientation of the Co magnetization, we perform ab-initio calculations in terms of the SKKR method [112]

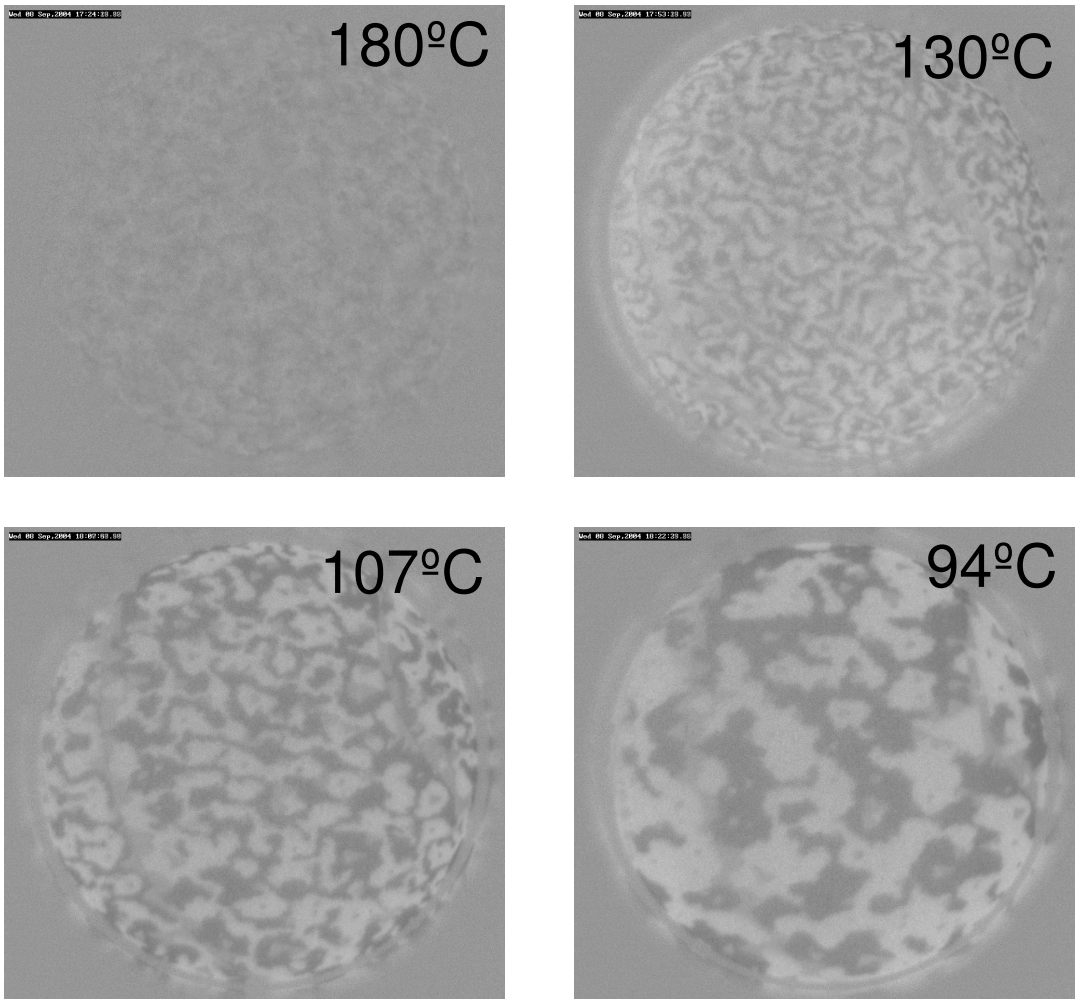

Figure 5.4: Perpendicular magnetization SPLEEM images of a 2 ML Co/Ru(0001) film. FOV is 7 μm and eE is 7 eV. a)-d) SPLEEM images at different temperatures. Magnetic contrast disappears at ∼200°C (470 K). Domains become smaller with increasing temperature.

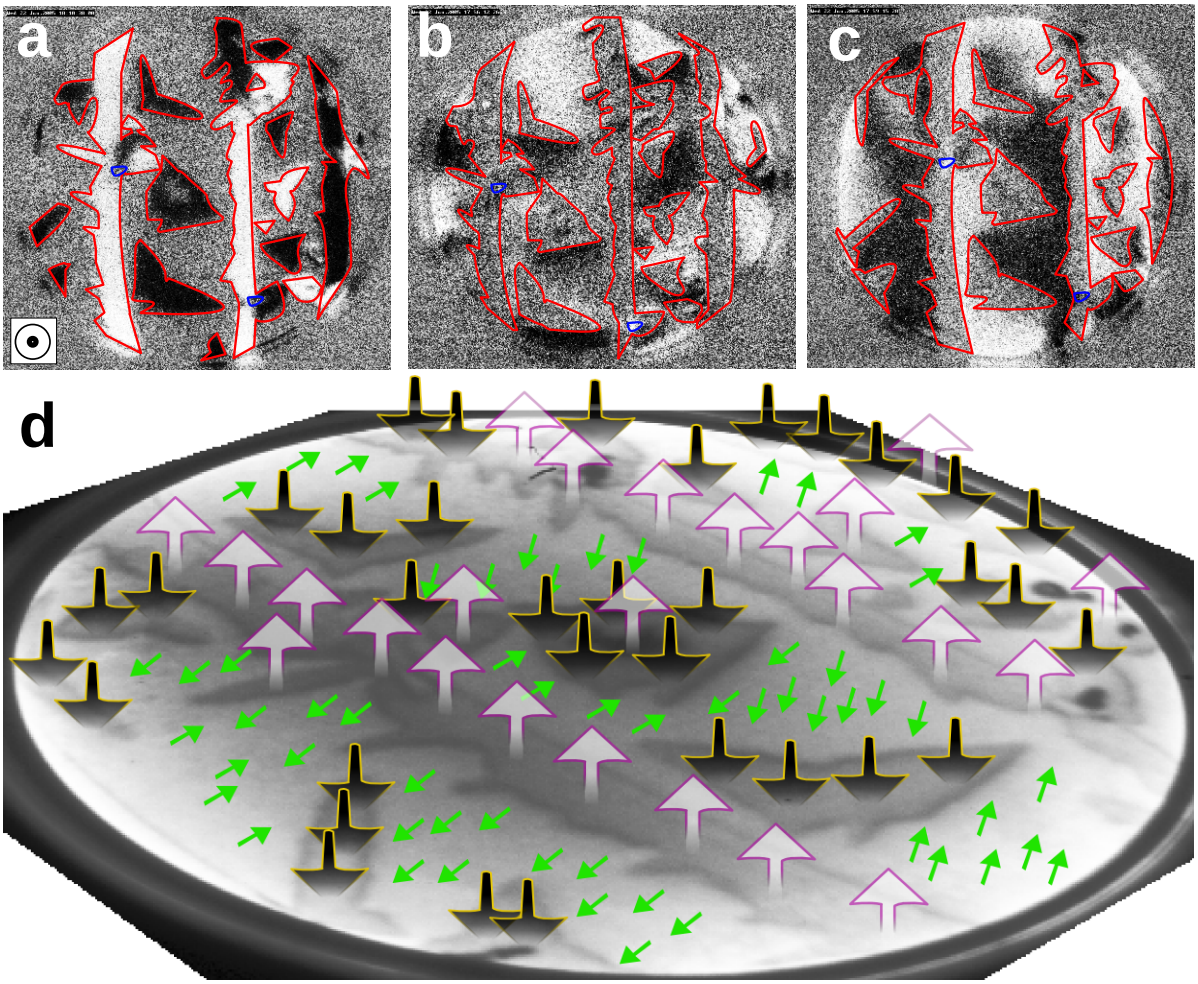

Figure 5.5: Images of topography and magnetization of one region of a 1.5 ML Co/Ru(0001) film. Images were taken at 110 K. Field of view is 2.8 μm and electron energy is 7 eV. a)-c) SPLEEM images with electron-polarization oriented: a) perpendicular; b) in-plane and 13° off a compact-direction; c) in-plane and 103° off a compact-direction. 2 ML islands are framed in red (two small 3 ML islands are framed in blue). d) LEEM image of the surface with the deduced magnetization direction indicated by arrows (black and white arrows mean perpendicular magnetization, green arrows mean in-plane magnetization). Dark grey indicates 2 ML islands, light grey 1 ML film.

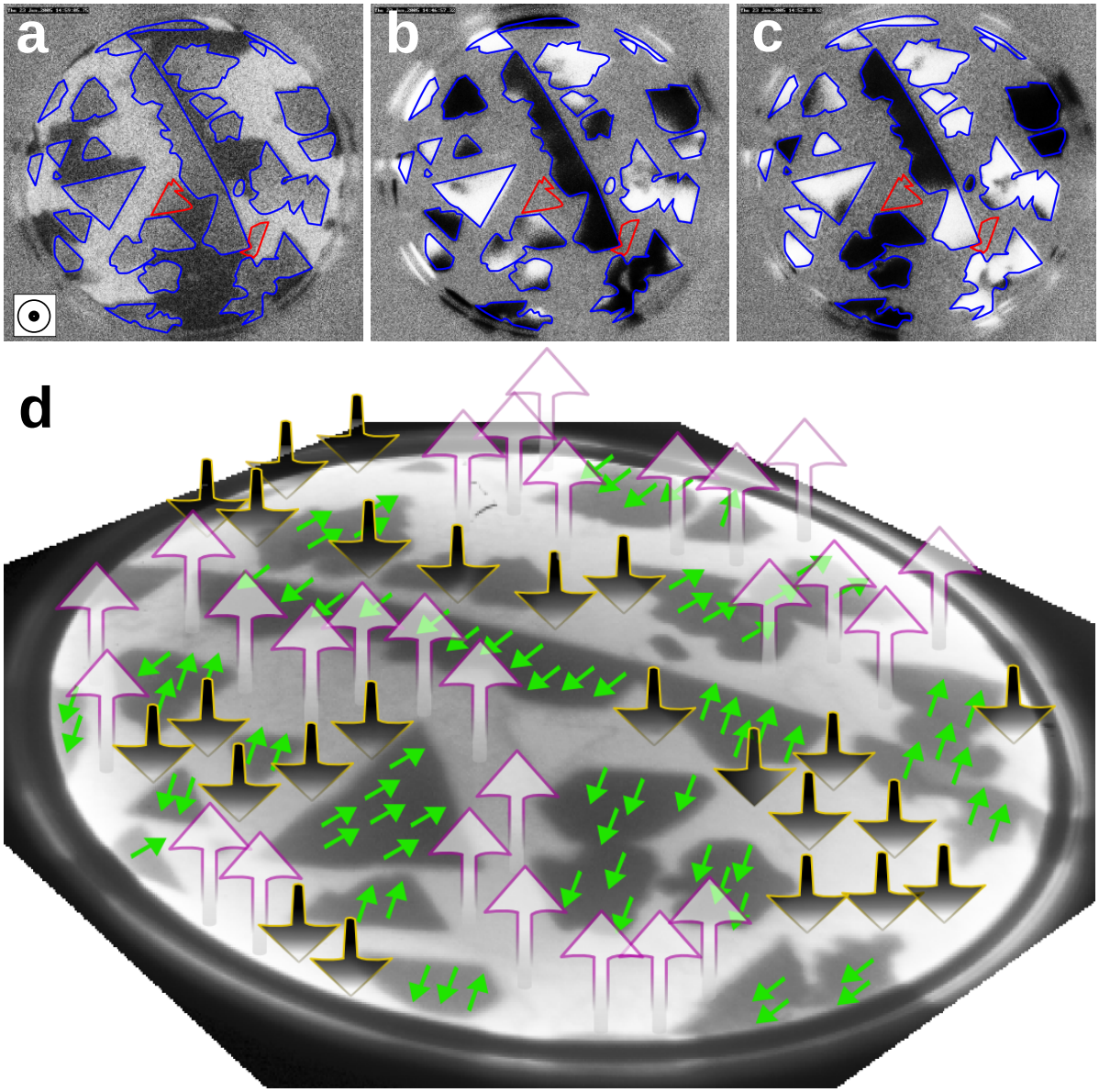

Figure 5.6: Images of topography and magnetization of one region of a 2.5 ML Co/Ru(0001) film. Images were taken at room temperature. Field of view is 2.8 μm and electron energy is 7 eV. a)-c) SPLEEM images with electron-polarization oriented: a) perpendicular; b) in-plane and 13° off a compact-direction; c) in-plane and 103° off a compact-direction. 3 ML islands are framed in blue. Two vacancy-islands in the 2 ML area, where Co is 1 ML thick, are framed in red. d) LEEM image of the surface with the deduced magnetization direction indicated by arrows (black and white arrows mean perpendicular magnetization, green arrows mean in-plane magnetization). Dark grey indicates 3 ML islands, light grey 2 ML film.

(for details see section §A-ii). Changing the lattice parameters in the calculations allows us to determine how strain influences the magnetic anisotropy. The magnetic anisotropy energy (MAE) is calculated as the difference of the total energy for an in-plane and an perpendicular magnetization. A positive MAE corresponds to an perpendicular magnetization. By employing the force theorem [116], the MAE is defined as a sum of a band energy, ΔE_b, and a magnetic dipole-dipole energy, ΔE_{dd} term. The band-energy term can further be resolved into contributions with respect to atomic layers that enable us to define surface and interface anisotropies.

First, we calculate the anisotropy of the pseudomorphic one-monolayer Co films, taking into account contractions of the Co-Ru interlayer distance (d). As summarized in Fig. 5.7a, the value of ΔE_b increases as the interplanar spacing decreases; however, due to the negative ΔE_{dd}, the preferred orientation of the magnetization remains always in-plane. Interestingly, the change in MAE is not proportional to the strain and, therefore, simple magnetoelastic arguments do not apply. Furthermore, we also tested the effect of contracting the in-plane lattice parameter of substrate and film. In that case, the MAE does not change significantly (result not shown in the figure). We conclude that the magnetization of the monolayer remains in-plane regardless of strain.

For two-monolayer and thicker films, the in-plane separation of the Co atoms is contracted by $\sim 5\%$ with respect to the Ru structure. We model the in-plane relaxation by contracting the supporting Ru substrate together with the Co film. Under this assumption, taking the same contraction for the Co-Co and Co-Ru interlayer spacing d from 0 to 7% relative to the substrate interlayer distance leads to a positive value of ΔE_b (Fig.5.7b) that, however, does not compensate the negative ΔE_{dd}. For the bilayer, the observed positive sign of the MAE occurs when different values for the Co-Co and Co-Ru interlayer distances are considered. In order to estimate the preferred relaxation of the interlayer distances we assume that atoms try to maintain the nearest-neighbors (NN) distances of their bulk materials, with Co-Ru distances being an average of the preferred Co-Co and Ru-Ru interlayer distances. This leads to contractions of 7% for the Co-Co interlayer distances and a nearly unrelaxed Co-Ru spacing. As shown in Fig. 5.7b, such a lattice distortion considerably increases ΔE_b resulting in a total positive MAE. A positive MAE is also obtained for an ideal Ru lattice with Co interlayer distances contracted by more than 4% (not shown). In 3 ML thick films, non-uniform contractions of the Co layers lead also to an enhancement of the positive ΔE_b (Fig.5.7c). Nevertheless, the decrease in the ΔE_{dd} term associated with thicker films drives the magnetization in-plane. A summary of our calculations of the MAE for the Co films of different thickness,

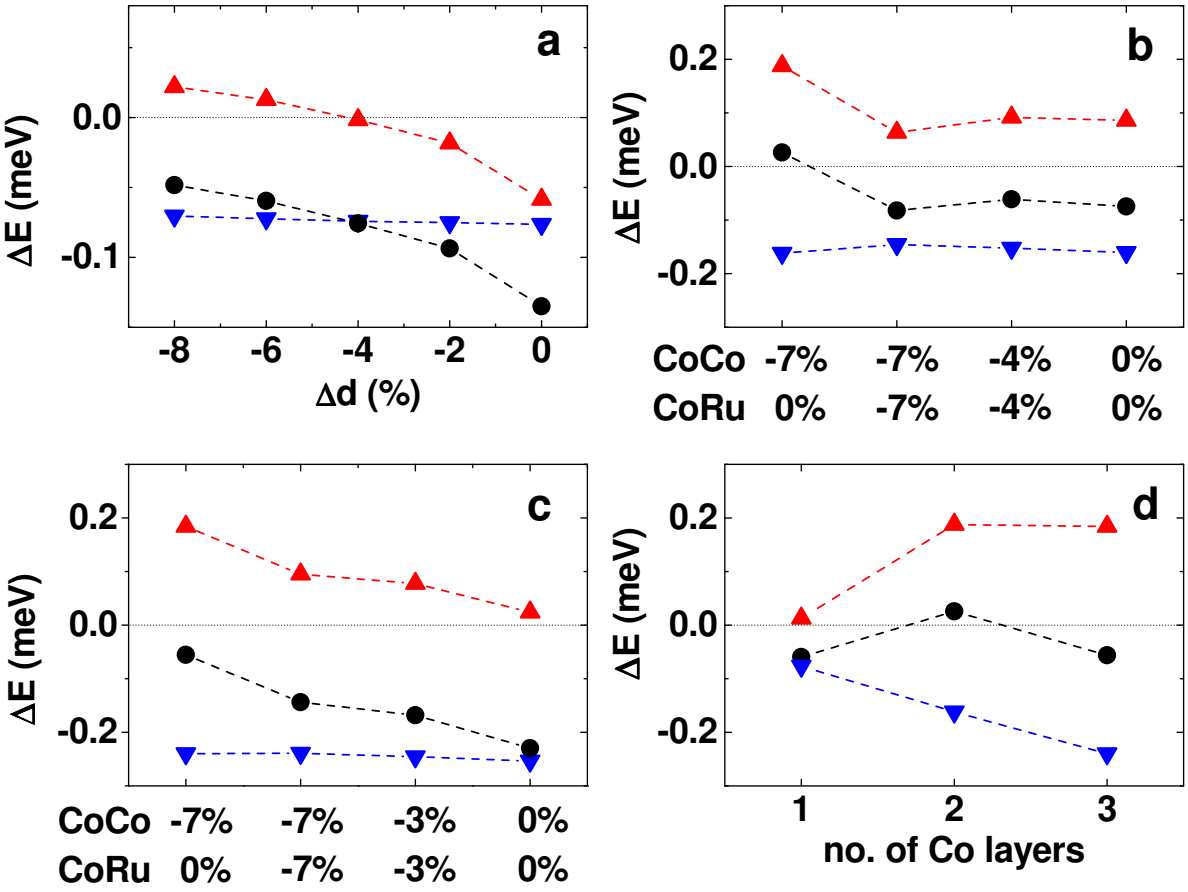

Figure 5.7: Calculated magnetic anisotropy energies of the different Co films on Ru. a)-c) Dependence of the calculated MAE on the interlayer distance referred to the substrate interlayer spacing. MAE (black circle) and its components, ΔE_b (red up-triangle) and ΔE_{dd} (blue down-triangle) for: a) a pseudomorphic 1 ML Co/Ru(0001) film under different contractions of the Co-Ru interlayer distance; in-plane strained b) 2 ML Co/Ru(0001) and c) 3 ML Co/Ru(0001) films with either the same or different (data points labelled by CoCo -7% and CoRu 0%) Co-Co and Co-Ru interlayer separations. d) MAE and its components in the most realistic geometry for the 1, 2 and 3 ML Co films on Ru(0001), displaying the double reorientation transition.

each at the most likely geometry, is shown in Fig. 5.7d. As a function of thickness the MAE changes sign twice, as observed experimentally.

Our calculations show that the double spin-reorientation transition is the result of a complicated interplay of structural and interface/surface electronic effects. All contributions to ΔE_b are strongly influenced by structural modifications. For 2 ML thick

films with the same Co-Co and Co-Ru interlayer separation, the dominant term is ΔE_b related to the interface Co. However, when Co-Co and Co-Ru separations are allowed to be different, the contribution of thesurface Co layer is remarkably enhanced resulting in a positive value of the MAE (perpendicular magnetization).

5.6 Summary and Conclusions

In conclusion, we deposited films of Co onto Ru(0001) in the thickness range of up to 3 atomic monolayers and find that the Curie temperature is well above room temperature provided the thickness is more than a single atomic monolayer. We observe two sharp reorientation transitions of the magnetization: 1 ML as well as 3 ML or thicker Co films have an in-plane easy axis, while only 2 ML thick films are magnetized in the perpendicular direction. The first transition is associated with a structural transformation from laterally strained, pseudomorphic 1 ML thick films to relaxed 2 ML thick films. Our first principles calculations show that the in-plane easy-axis of one- and three-monolayer films is stable with respect to variations of the strain conditions. Only for two-monolayer films, the combination of strain with additional interface and surface effects drives the magnetic easy-axis into the perpendicular direction.

Chapter 6

Copper on Cobalt on Ruthenium (0001): Magnetic structure

"Nothing shocks me. I'm a scientist."
— *Indiana Jones and the Temple of Doom*, Indiana Jones, 1984

This chapter describes the experiments of growth and magnetic measurements of Cu capping layers on top the previously studied system Co/Ru(0001). Cu films have been gown layer by layer (for up to 3 layers) on top of 1 to 6 ML of Co on Ru(0001). The growth process have been followed by LEEM.

We report in this chapter the spin-reorientation transition that takes place on three and four cobalt layers on Ru(0001) upon copper deposition. The bare films present an in-plane magnetization in remanence. By means of SPLEEM we observe in real space and real time with nanometer resolution how the magnetization changes to out-of-plane when depositing a single copper atomic layer. Deposition of an additional copper layer drives the magnetization in-plane. No further changes were observed. No other thicknesses below six cobalt layer show such behavior.

6.1 Introduction

Ultra-thin films of transition metals oxidize in air. Capping the films with non-magnetic material such as gold or copper has become standard practice for measuring the mag-

netic properties ex-situ. This raises the concern of the possible effect of the capping layer on the properties of the magnetic film. The role of non-magnetic layers has been highlighted by the discovery of oscillatory magnetic coupling [117, 118]. The capping layers have also been observed to influence the magnetic anisotropy. Interface effects, a term that includes from modifications of the electronic structure to changes in the strain of the magnetic film, have been frequently observed [119, 120]. Deposition of gas adsorbates on Fe/W changes the magnetization easy axis from perpendicular to in-plane orientation [121]. And the deposition of minute amounts of copper [122] can rotate within the plane the extremely weak in-plane magnetization direction in cobalt films. But no consecutive reorientation of the magnetization, such as observed with thickness of the magnetic film itself (see chapter 5), has been reported. Specially interesting would be such a SRT to or from perpendicular magnetization.

We report in this work the surprising observation that one copper layer drives the magnetization from in-plane to perpendicular in films of three or four atomic cobalt layers on Ru(0001). And two copper layers drive the magnetization in-plane as in the bare cobalt films. We followed the SRT in real-time during copper growth by SPLEEM.

6.2 The Spin Reorientation Transitions

We grow one and two monolayers of Cu in systems with 1 to 6 ML of Co on Ru(0001). All the films were studied in-situ with LEEM and SPLEEM.

6.2.1 1 ML Cu/1, 2, and 3 ML Co/Ru(0001): first SRT evidence

Fig. 6.1 shows a LEEM image of a Ru(0001) surface covered with regions of 1, 2, and 3 ML of Co with 1 ML of Cu. SPLEEM images b) and c) present no magnetic contrast. This can be easily verified comparing the grey inside the circular FOV area with the grey tone at the corners of the image (noise). Regions with 1 ML Cu/1 ML Co/Ru(0001) present no magnetic contrast (see sec. 6.2.2). The slight contrast in image c) (slightly darker and brighter in regions of 1 ML Cu/3 ML Co/Ru(0001)) is an artifact produced by a non perfectly perpendicular polarization of the incident electron beam together with a long image-intensity integration time (2 s). The Cu induces a SRT from in-plane (3 ML Co/Ru(0001)) to perpendicular (1 ML Cu/3 ML Co/Ru(0001)). For a schematic

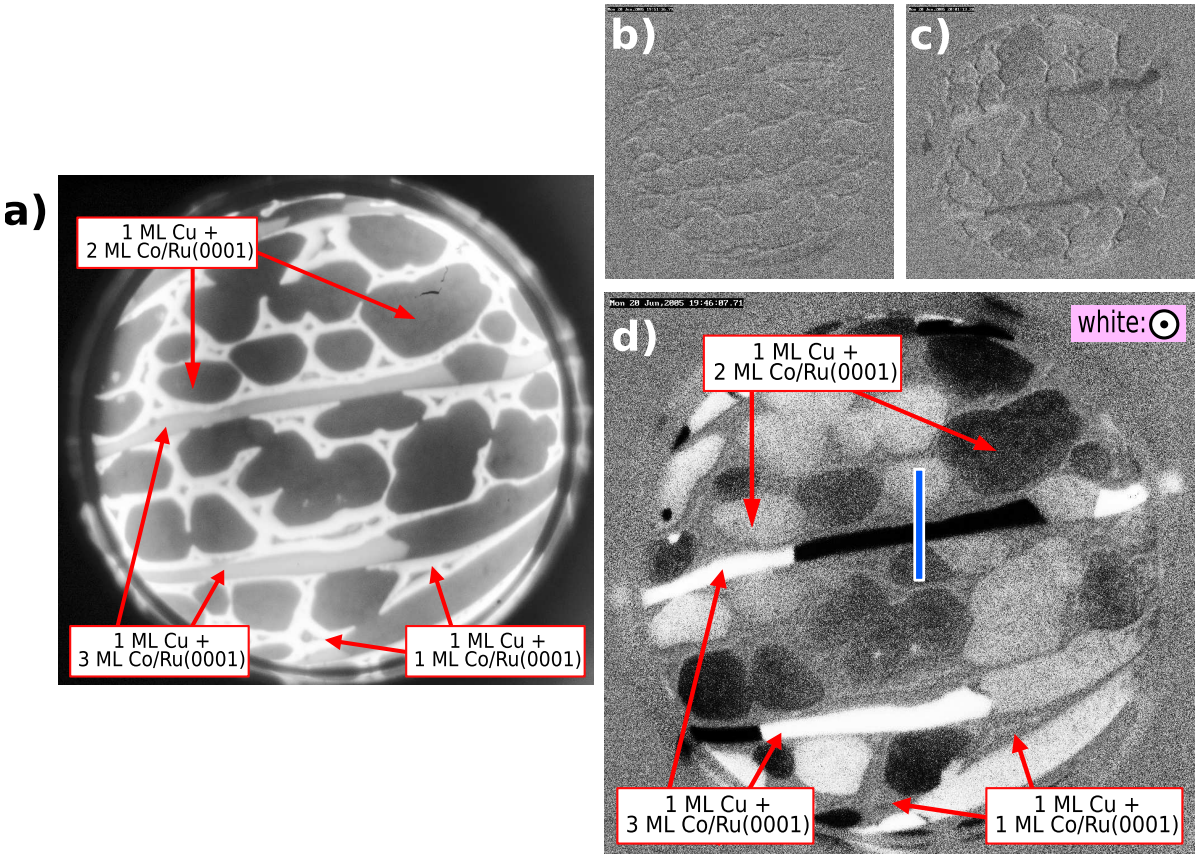

Figure 6.1: LEEM and SPLEEM images of the same area of the surface with 1 ML Cu over regions of 1, 2 and 3 ML of Co over Ru(0001). The experiment parameters are: FOV is 7 μm, electron energy (eE) is 7.6 eV and the temperature is 110 K. a) LEEM image of the surface. The Co thickness is indicated in the picture. b)-d) SPLEEM images with electron-polarization oriented: b) in-plane and 13° off a compact-direction; c) in-plane and 103° off a compact-direction; d) perpendicular. (See text for further details).

of the cross section at the position of the blue line shown in panel d) see Fig. 6.2.

Fig. 6.1d present two levels of magnetic contrast: light grey (dark grey) and white (black). Medium grey indicates no magnetic contrast in the perpendicular direction. Light grey and white domains are magnetized perpendicular to the surface pointing outside the sample. Dark grey and black domains are magnetized also perpendicular to the surface but pointing inside the sample. The black and white regions are composed of 1 ML Cu/3 ML Co/Ru. The magnetization of those regions is stronger than that of the regions with 1 ML Cu/2 ML Co/Ru. The integration time needed to measure the weak magnetization regions (2 s/image) saturates the contrast in the strong magnetization

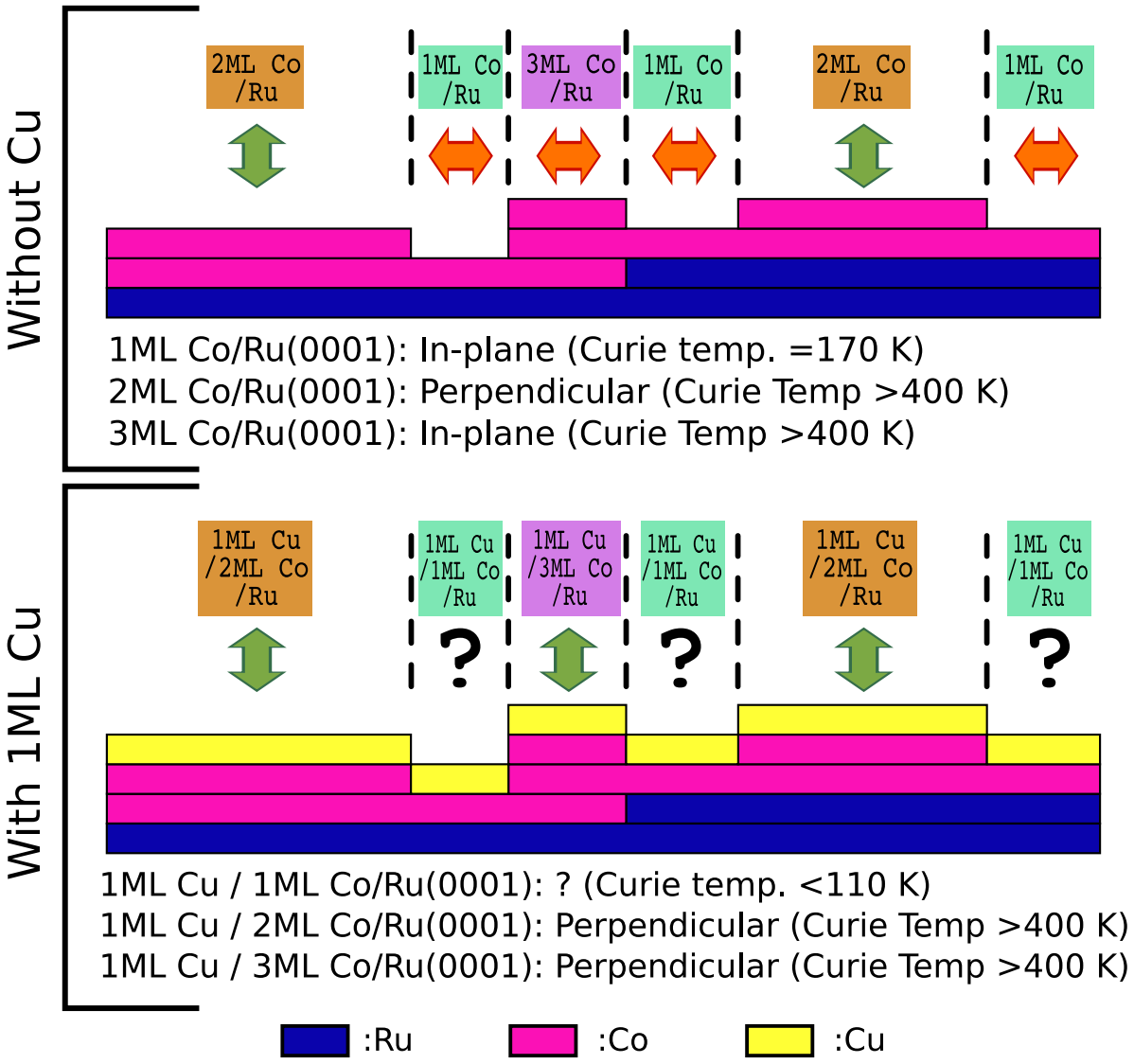

Figure 6.2: Schematic of the experiment presented in Fig. 6.1 showing the thickness and the magnetization direction before (up) and after (down) the deposition of one Cu capping layer.

regions.

6.2.2 1 ML Cu/1 and 2 ML Co/Ru(0001)

Fig. 6.3 shows a LEEM and a complete set of SPLEEM images of the surface of a film composed of 1 ML Cu/1.1 ML Co/Ru(0001). A summary of the measured magnetization for each region is as follows: regions with 1 ML Cu/1 ML Co/Ru(0001) present no magnetic contrast; regions with 1 ML Cu/2 ML Co/Ru(0001) are perpendicularly magnetized; regions with 2 ML Co/Ru(0001) are also perpendicularly magnetized (as we already know) but with much weaker magnetic contrast.

The Curie temperature of 1 ML Co/Ru(0001) is ∼170 K. The growth of a Cu capping layer has been shown to reduce the Curie temperature by about 100 K for Co films over Cu(001) [119], leaving it below the lowest temperature achievable by the cooling system of our SPLEEM. In section 6.2.1 we measured 1 ML Cu/1 ML Co/Ru(0001) at 110 K with SPLEEM and did not found magnetic contrast. Then, one possibility is that the Curie temperature of the films with 1 ML of Co/Ru(0001) decreases below 110 K with the addition of 1 ML of Cu. Another effect that can be responsible of the absence of magnetic contrast is the interdiffusion of Cu in the first monolayer of Co. It is known that Co and Cu are partially miscible as monolayers [123–125].

6.2.3 1 and 2 ML Cu/3 and 4 ML Co/Ru(0001): the SRTs in detail

We grow a new film of 3.5 ML of Co on a clean Ru(0001) surface and measure it with SPLEEM. We already know from chapter 5 that 3 and 4 ML of Co on Ru(0001) are magnetized in-plane. As a summary we show Co films on Ru without the Cu capping layer. Fig. 6.4 shows LEEM and SPLEEM images of 3.5 ML Co/Ru(0001): 3 and 4 ML regions of Co on Ru(0001) are completely magnetized in-plane.

After confirming the in-plane magnetization for this film, we start to grow the Cu capping layers. All the changes in the structure and in the perpendicular magnetization during growth where recorded in real time with the SPLEEM. Fig. 6.5 and Fig. 6.6 shows an image sequence of the process, composed of couples of LEEM and perpendicular-polarization SPLEEM images. The time since the start of the Cu deposition is indicated at the right of each SPLEEM image. LEEM images (left row) show the topography

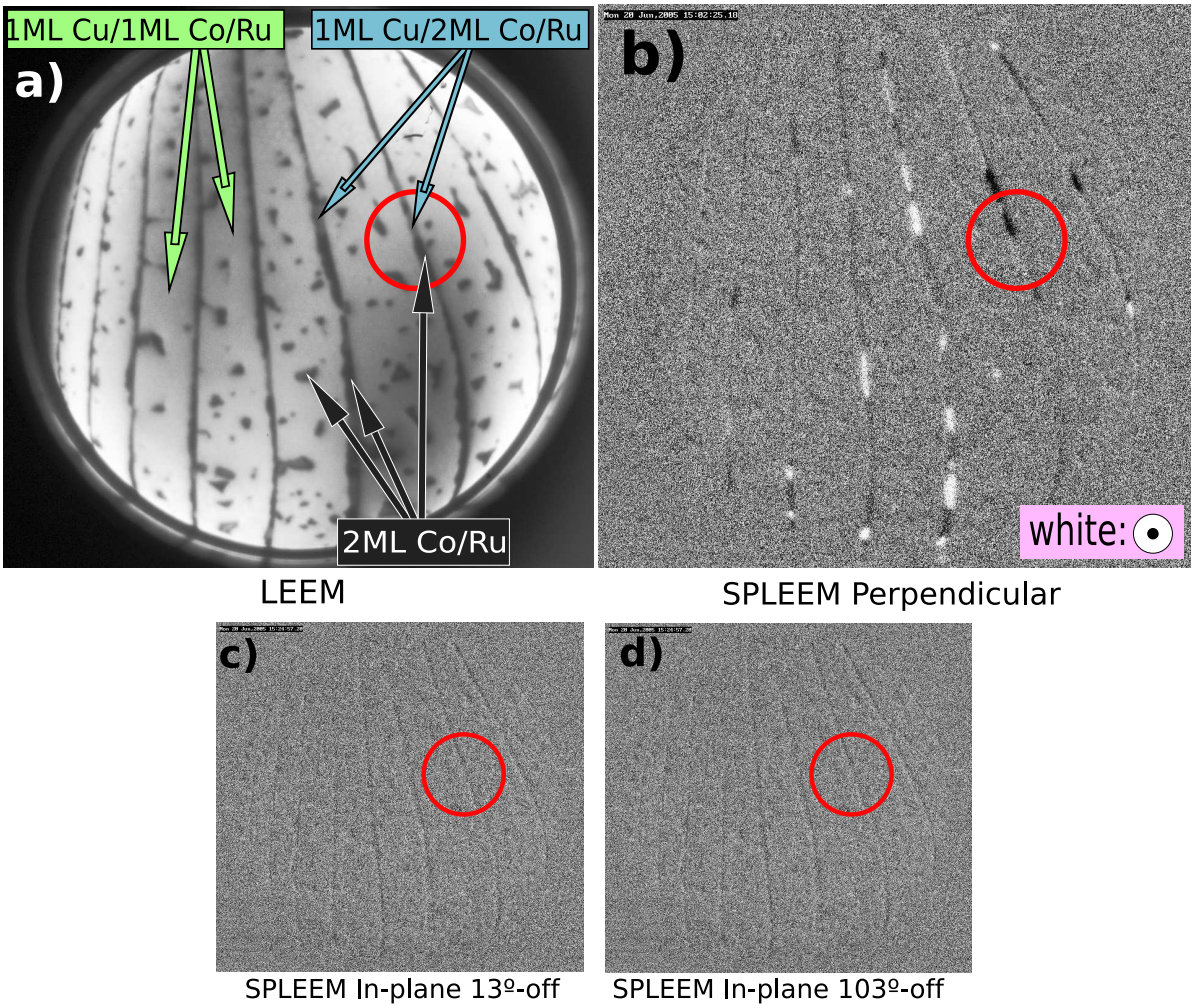

Figure 6.3: LEEM and SPLEEM images of the same area of the surface with regions of 1 and 2 ML of Co over Ru(0001) covered with 1 ML Cu. The experiment parameters are: FOV is 7 μm, eE is 7.6 eV; measured at room temperature. a) LEEM image of the surface. The Cu and Co thickness are indicated by arrows. b)-d) SPLEEM images with electron-polarization oriented: b) perpendicular to the surface; c) in-plane and 13° off a compact-direction; d) in-plane and 103° off a compact-direction. The red circle frames the same region in the four panels. Regions with 1 ML Cu/1 ML Co/Ru(0001) (light grey) present no magnetic contrast. There are some small dark grey regions (in particular part of the step flow material and all the islands) composed of 2 ML Co/Ru(0001). Those regions are perpendicularly magnetized, but present less magnetic contrast than the regions with 1 ML Cu/1 ML Co/Ru(0001) (medium grey), also perpendicularly magnetized.

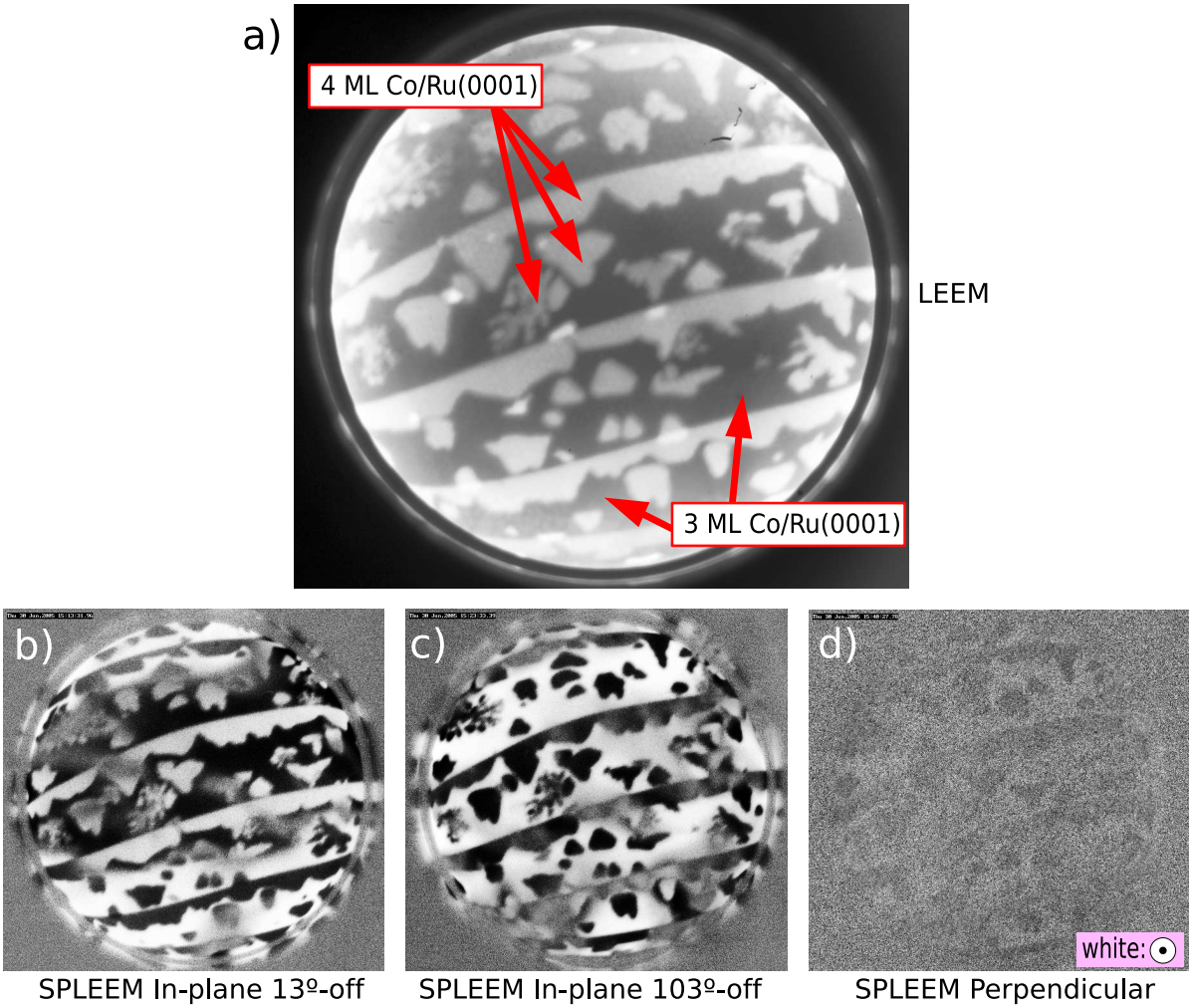

Figure 6.4: LEEM and SPLEEM images of the same area of the surface with regions of 3 and 4 ML of Co over Ru(0001). The experiment parameters are: FOV is 7 μm, eE is 7 eV and the temperature is 511 K. a) LEEM image of the surface. The Co thickness is indicated in the picture. b)-d) SPLEEM images with electron-polarization oriented: b) in-plane and 13° off a compact-direction; c) in-plane and 103° off a compact-direction; d) perpendicular. Images b)- d) shows that 3 and 4 ML of Co/Ru(0001) are completely magnetized in-plane, with no perpendicular magnetic contrast (this can be easily check comparing the FOV region grey with the grey at the corners of the image).

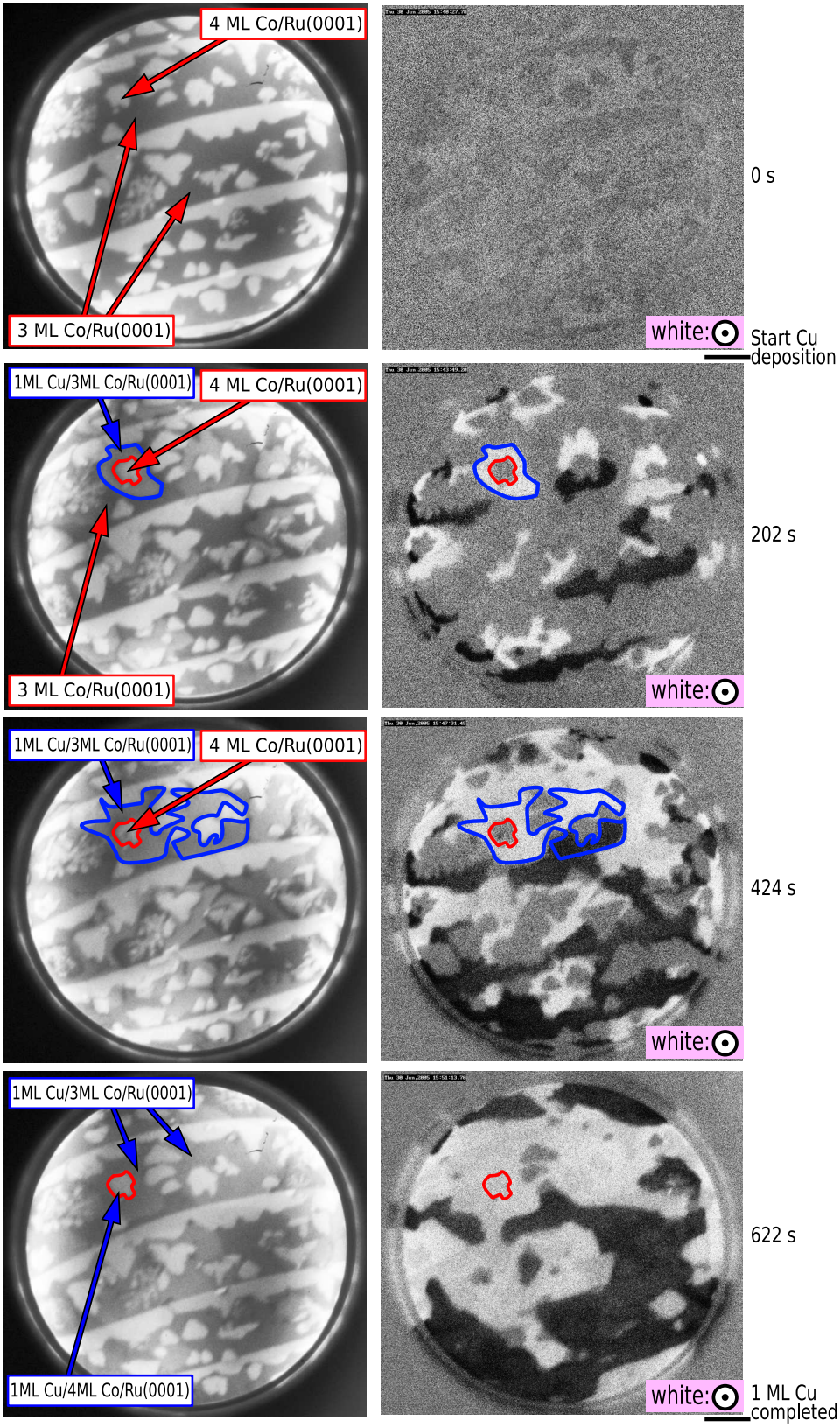

Figure 6.5: LEEM and perpendicular SPLEEM image sequence of the growth of 1ML Cu over 3.5 ML Co/Ru(0001). FOV is 7 μm, eE is 7 eV and the temperature 513 K. (See text for further details).

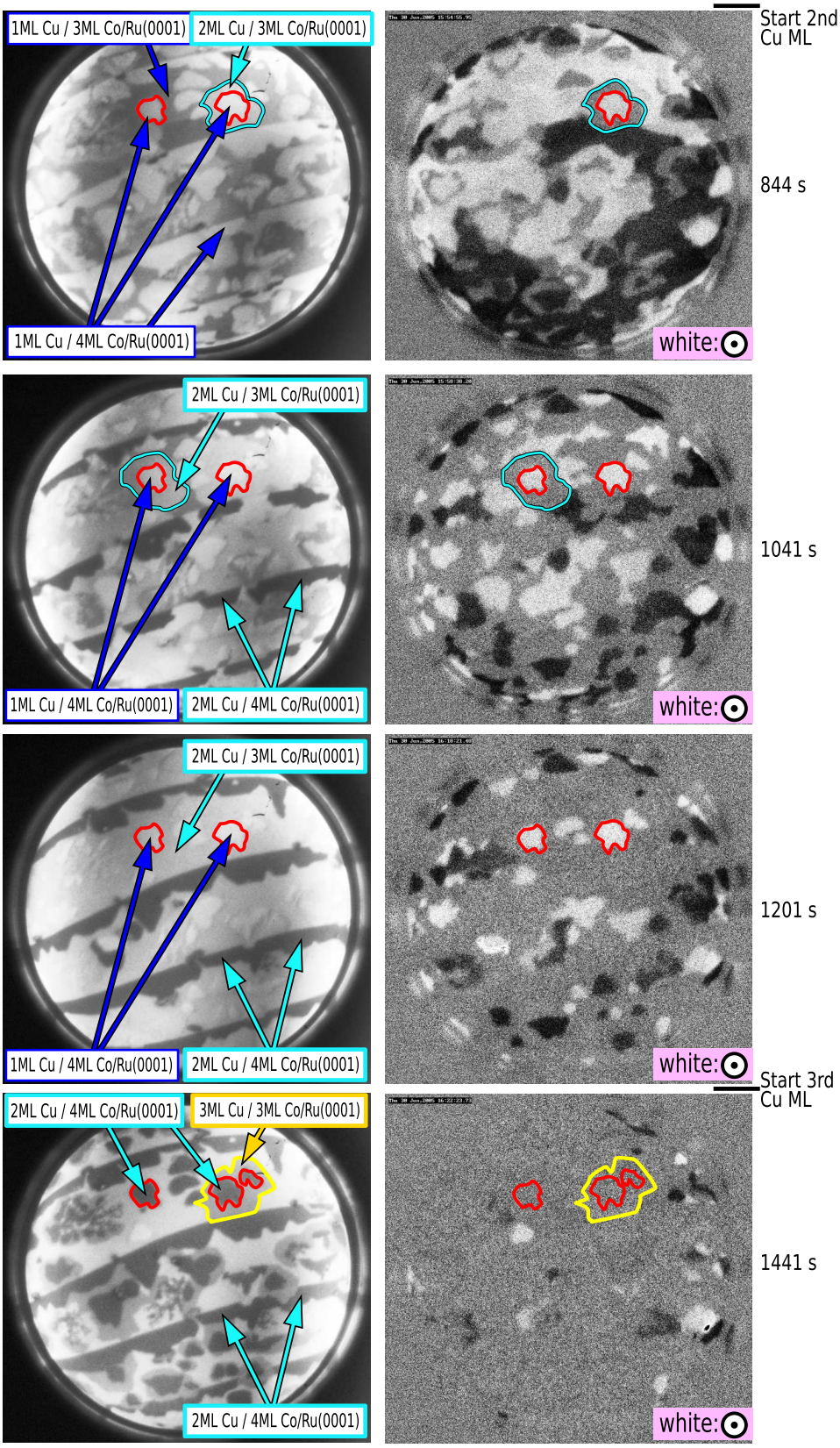

Figure 6.6: LEEM and perpendicular SPLEEM image sequence of the growth of 1ML Cu over 1ML of Cu/3.5 ML Co/Ru(0001). FOV is 7 μm, eE is 7 eV and the temperature 513 K. This sequence is continuation of the sequence presented in Fig. 6.5. (See text for further details).

of the surface during Cu growth. Different contrast regions correspond to different thicknesses and/or composition of that region (indicated by arrows in the LEEM images). SPLEEM images (right row) show the perpendicular magnetization of the surface. White regions are magnetized perpendicular to the surface pointing outside the sample. Black regions are magnetized also perpendicular to the surface but pointing inside the sample. Some arbitrary regions are framed in colors to help the comparison between LEEM and SPLEEM images. The sequence continues for another monolayer of Cu in Fig. 6.6. The magnetization of this system switches from in-plane to perpendicular with the first Cu monolayer and back to in-plane with the second Cu capping layer.

Fig. 6.5 and Fig. 6.6 shows another interesting process during the Cu growth over a system with 3 and 4 ML Co/Ru(0001). The first Cu layer do not start to cover the islands of 4 ML Co until the 3 ML Co is completely covered. This means that the Cu can easily (at 513 K) come down the steps between 4 and 3 ML Co when it is deposited on top of a 4 ML Co island. When the 3 ML film is completely covered with 1 ML of Cu, Cu starts to cover the fourth monolayer. The second Cu monolayer does not start to appear until the whole surface is covered with 1 ML of Cu. The second Cu layer grows in the same fashion: it first covers the 1 ML Cu/3 ML Co/Ru film and then it covers the 1 ML Cu/4 ML Co/Ru films.

Fig. 6.7 shows a complete set of SPLEEM images of the surface of 1.5 ML of Cu over 3.5 ML Co/Ru(0001). This figure shows four different LEEM contrast regions and its respective magnetization:

i) 1 ML Cu over 3 ML Co/Ru(0001), perpendicular

ii) 1 ML Cu over 4 ML Co/Ru(0001), perpendicular

iii) 2 ML Cu over 3 ML Co/Ru(0001), in-plane

iv) 2 ML Cu over 4 ML Co/Ru(0001), in-plane

A technologically promising system is shown in Fig. 6.8. It is composed of 1 ML Cu over 3 and 4 ML of Co/Ru(0001). The system magnetization is completely perpendicular. The perpendicular domains extends over the whole surface without distinguishing between the two different thicknesses. The Curie temperature of this film is above 510 K[1]

[1]We decide not to heat the film above 520 K to avoid the possible CoRu alloy formation (see section 4.2).

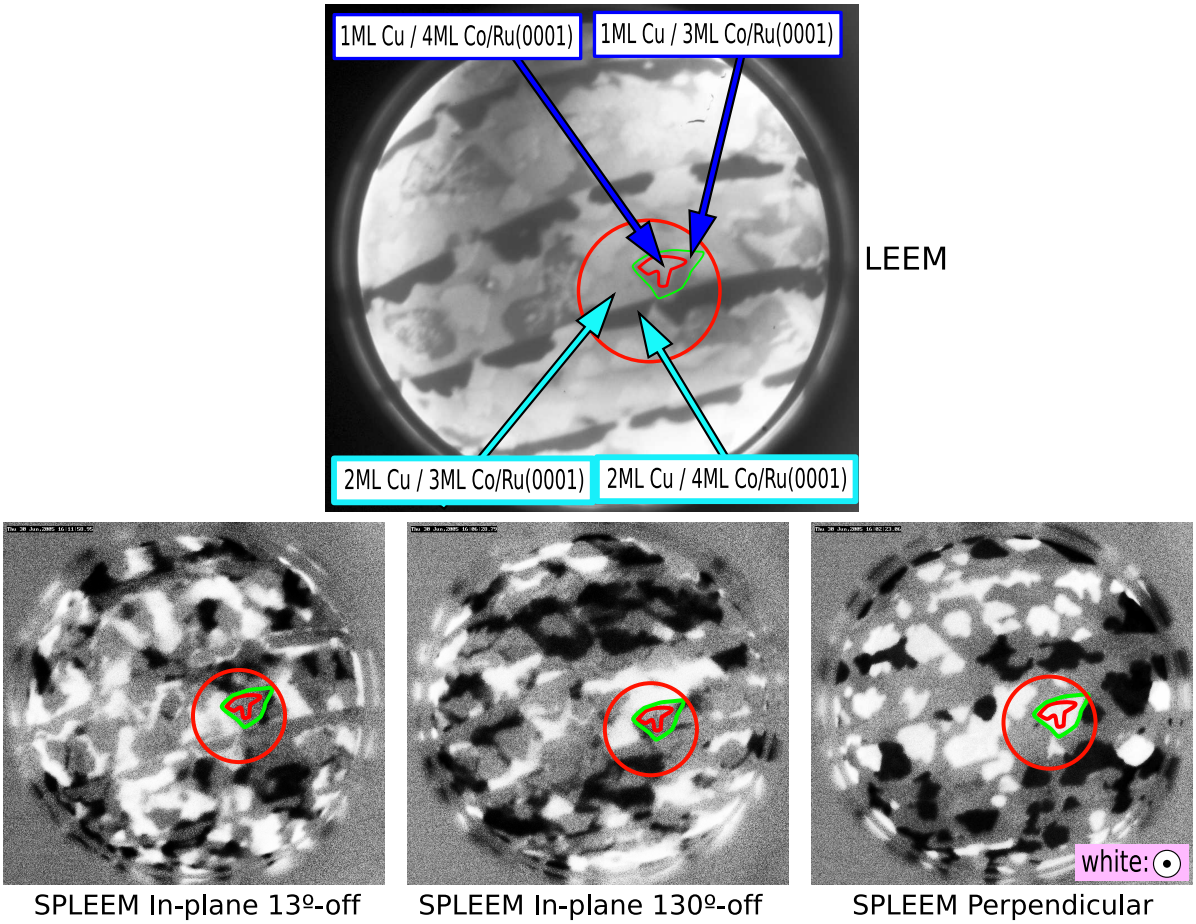

Figure 6.7: LEEM and SPLEEM images of the same area of the surface with regions of 3 and 4 ML of Co over Ru(0001) covered with 1 or 2 ML Cu. The experiment parameters are: FOV is 7 μm, eE is 7 eV and the temperature is 511 K. a) LEEM image of the surface. The Co thickness is indicated in the picture. b)-d) SPLEEM images with electron-polarization oriented: b) in-plane and 13° off a compact-direction; c) in-plane and 103° off a compact-direction; d) perpendicular. Some regions are framed in color for easy comparison between images.

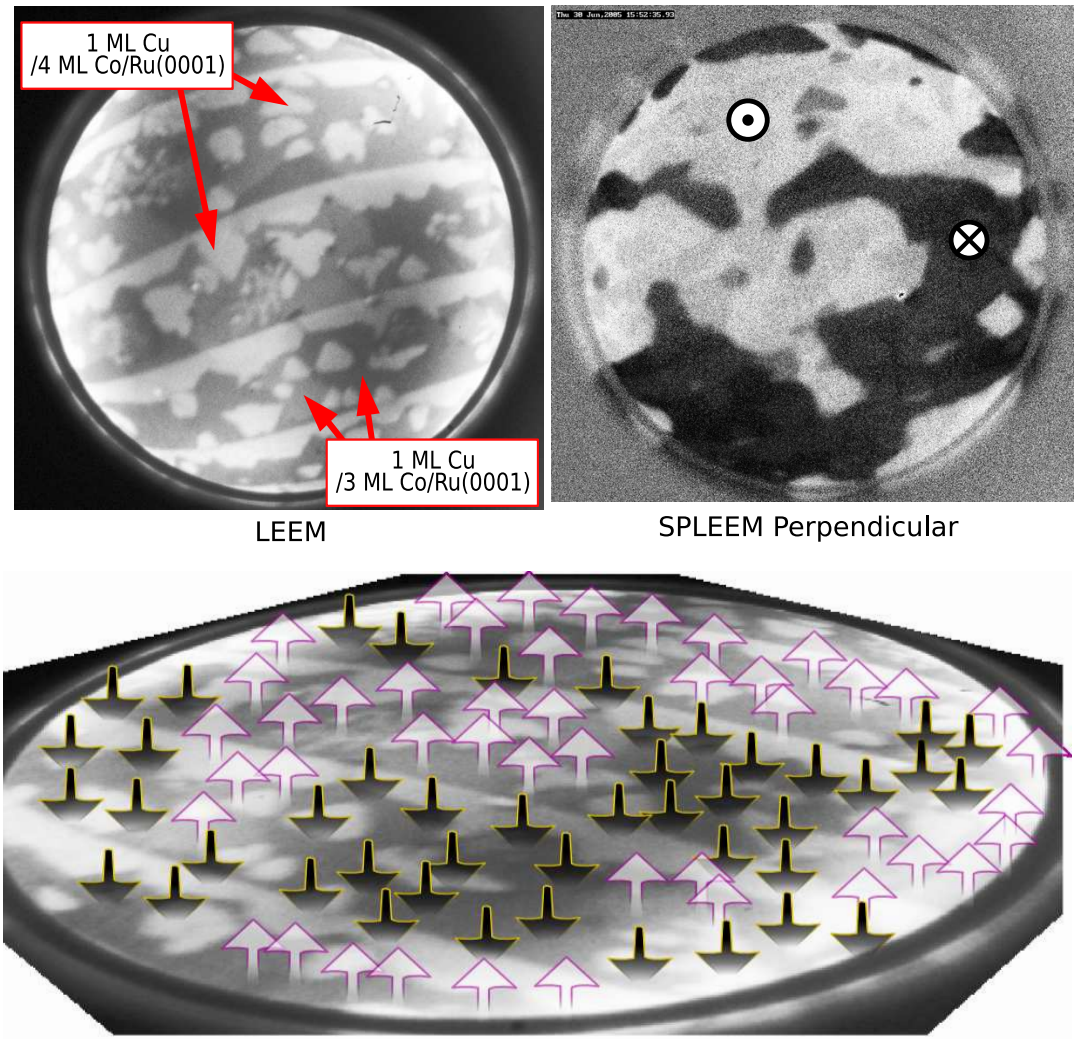

Figure 6.8: LEEM and SPLEEM images of the same area of the surface with regions of 3 and 4 ML of Co over Ru(0001) covered with 1 monolayer of Cu. The experiment parameters are: FOV is 7 μm, eE is 7 eV and the temperature is 510 K. Top: LEEM and SPLEEM images of the surface. The Co thickness is indicated in the LEEM image. The SPLEEM image was taken with the electron-polarization oriented perpendicular to the surface. Bottom: LEEM image with the magnetization direction of each region indicated by arrows.

There are no big changes in the LEEM-LEED pattern upon Cu deposition. Fig. 6.9 shows the diffraction patterns of 3 ML Co/Ru(0001): a,b) without Cu; c,d) with 1 ML Cu; e,f) with 2 ML Cu. The two Cu overlayers follow the Co structure[2], which for 3 ML and 4 ML over Ru(0001) is close to be relaxed to the bulk Co structure. The diffraction patterns show no evidence of ordered alloy formation in this temperature range (440-520 K).

6.2.4 1 and 2 ML Cu/5 and 6 ML Co/Ru(0001)

5 and 6 ML Co/Ru(0001) are magnetized in-plane (Fig. 6.10). The addition of 1 (Fig. 6.11) or 2 ML (Fig. 6.12) of Cu does not result in a SRT.

6.3 *Ab-initio* Calculations: Preliminary Results

To understand the effects that give rise to the observed SRT, we perform ab-initio calculations in terms of the SKKR method [112] (for all the details see section §A-ii). The brief conclusions presented in this section are based on preliminary calculations which are not yet completely finished.

Ab-initio calculations have been done for several different stacking sequences and lattice parameters for Cu and Co. For each structure, the total energy of the system, the total MAE and layer by layer contributions to the MAE were calculated.

Calculations on the system Cu over 3 and 4 ML Co/Ru(0001) suggest that the Cu can grow with fcc or hcp structure[3] on top of Co, with atomic volume close to hcp Co. The Cu could induce an fcc stacking of Co, that can lead to the production of stacking faults in Co topmost layer[4] as has been reported for Cu/Co(0001) [126].

MAE calculations for different structures of the Cu and Co reveal that capping layers effects on the MAE are intimately related to the structural modifications (stacking and lattice parameter): hcp Cu lowers the MAE (it favors in-plane magnetization) and fcc Cu increases the MAE (it favors perpendicular magnetization). The second Cu layer

[2]The in-plane lattice mismatch between bulk Co and bulk Cu is only 1.83 %.

[3]The total energy of both systems is almost identical.

[4]The energy difference between: (i) all Co grown in hcp with one monolayer of Cu in fcc (Ru/Co/Cu: BA/BAB/C) and (ii) all Co but the topmost layer in hcp, the topmost layer and the Cu in fcc (Ru/Co/Cu: BA/BAC/B) is only ∼20 meV/atom.

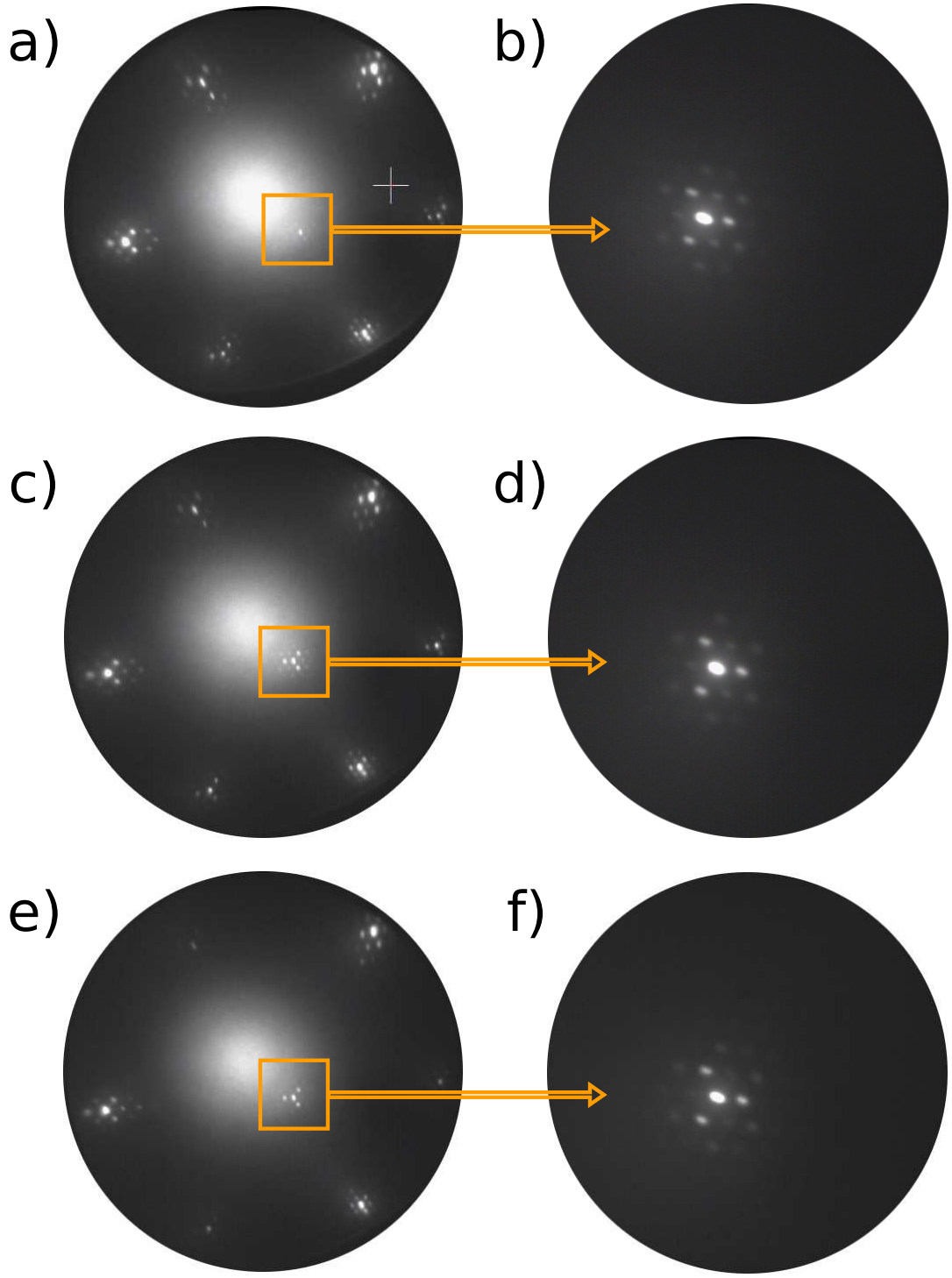

Figure 6.9: LEED patterns measured at room temperature of: a) 3 ML Co/Ru(0001); c) 1 ML Cu/3 ML Co/Ru(0001); e) 2 ML Cu/3 ML Co/Ru(0001); eE=53.4 eV. b,d,f) Zoomed specular spots (correspondence indicated by arrows), eE=24.5 eV. LEED patterns show no dramatic changes in the structure.

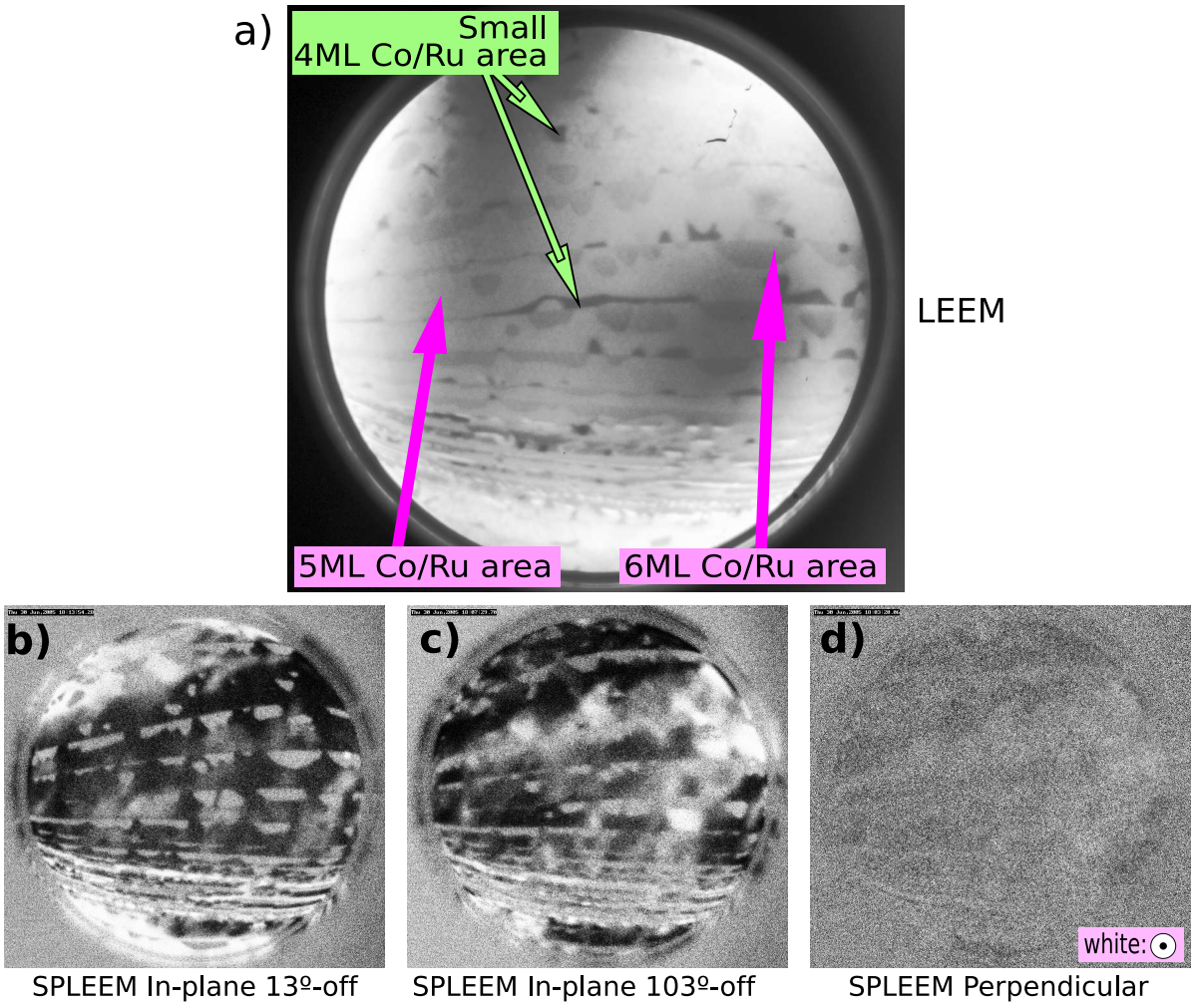

Figure 6.10: LEEM and SPLEEM images of the same area of the surface with regions of 5 and 6 ML of Co over Ru(0001). The experiment parameters are: FOV is 7 μm, eE is 7 eV and the temperature is 518 K. a) LEEM image of the surface. The Co thickness is indicated in the picture. There are some small regions with 4 ML Co. b)-d) SPLEEM images with electron-polarization oriented: b) in-plane and 13° off a compact-direction; c) in-plane and 103° off a compact-direction; d) perpendicular. Images b)- d) shows that 5 and 6 ML of Co/Ru(0001) are completely magnetized in-plane, with no perpendicular magnetic contrast (this can be easily check comparing the FOV region grey with the grey at the corners of the image).

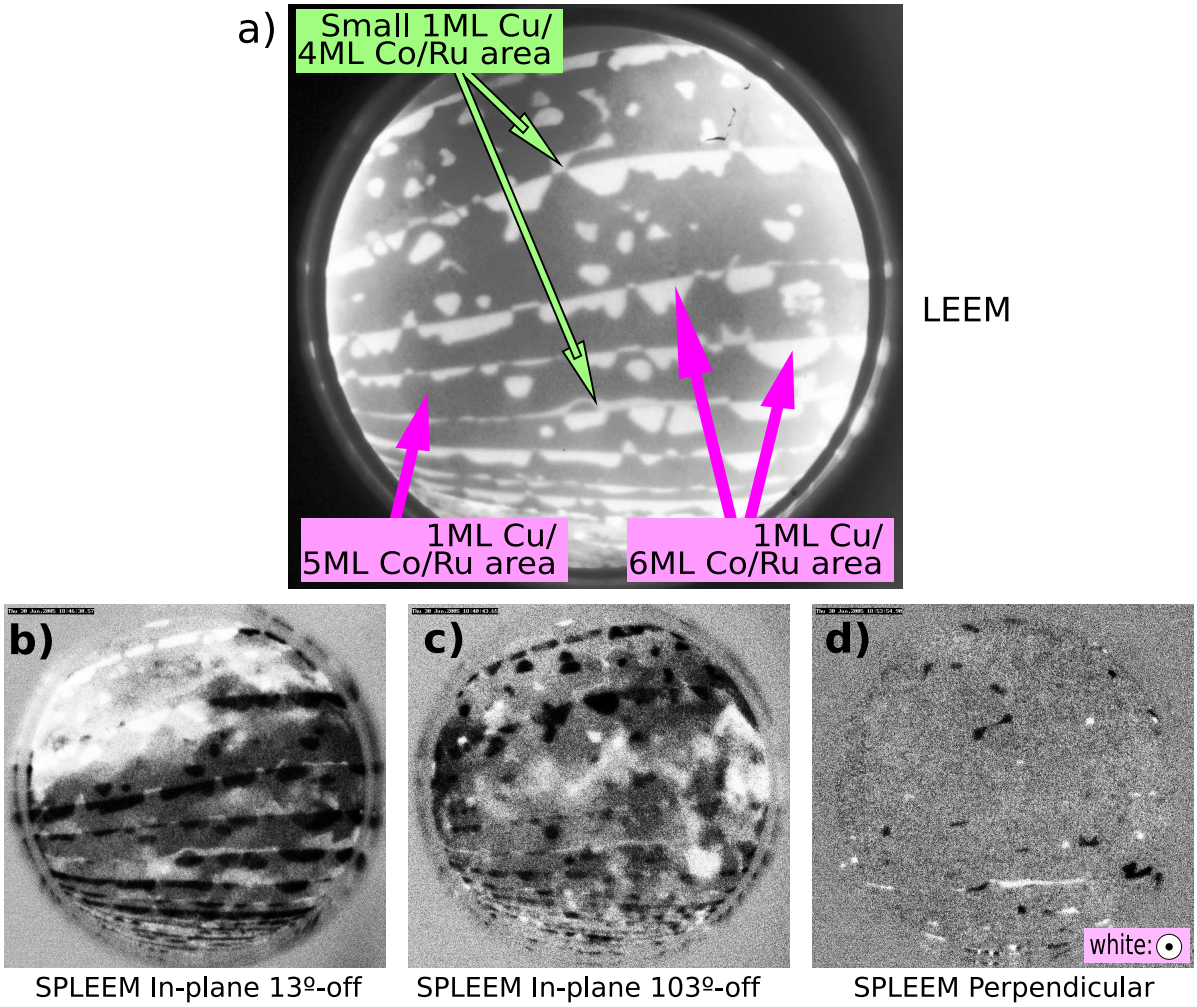

Figure 6.11: LEEM and SPLEEM images of the same area of the surface with regions of 5 and 6 ML of Co over Ru(0001) covered with 1 ML Cu. The experiment parameters are: FOV is 7 μm, eE is 8.2 eV and the temperature is 518 K. a) LEEM image of the surface. The Cu/Co thickness is indicated in the picture. b)-d) SPLEEM images with electron-polarization oriented: b) in-plane and 13° off a compact-direction; c) in-plane and 103° off a compact-direction; d) perpendicular. Images b)- d) shows that 1 ML Cu over 5 and 6 ML of Co/Ru(0001) are completely magnetized in-plane, with no perpendicular magnetic contrast. There are some small regions with 1 ML Cu/4 ML Co/Ru(0001) that present perpendicular magnetization, as can be seen in the perpendicular SPLEEM image.

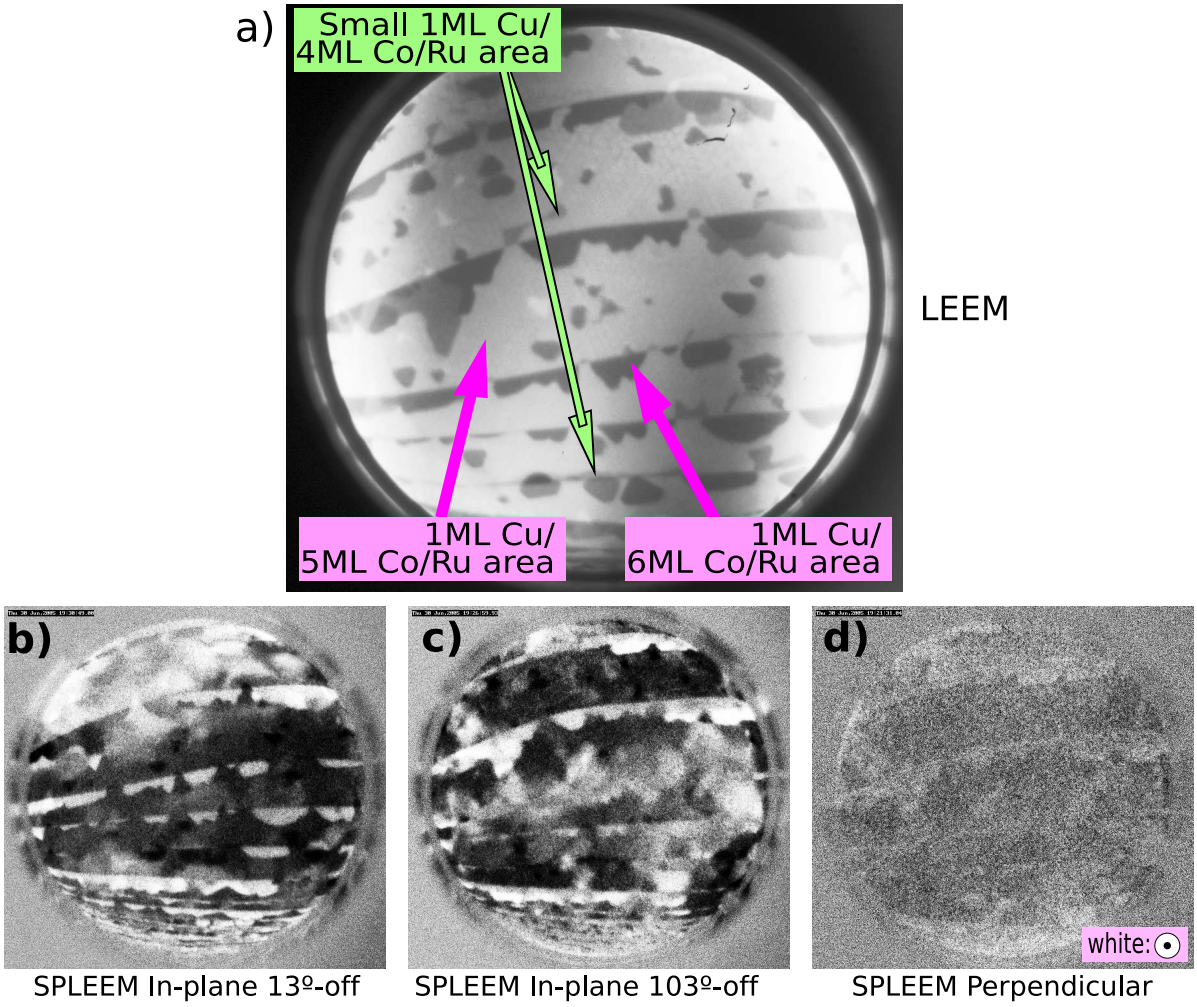

Figure 6.12: LEEM and SPLEEM images of the same area of the surface with regions of 5 and 6 ML of Co over Ru(0001) covered with 2 ML Cu. The experiment parameters are: FOV is 7 μm, eE is 8.2 eV and the temperature is 513 K. a) LEEM image of the surface. The Cu/Co thickness is indicated in the picture. b)-d) SPLEEM images with electron-polarization oriented: b) in-plane and 13° off a compact-direction; c) in-plane and 103° off a compact-direction; d) perpendicular. Images b)- d) shows that 2 ML Cu over 5 and 6 ML of Co/Ru(0001) are completely magnetized in-plane, with no perpendicular magnetic contrast. The regions with 2 ML Cu/4 ML Co/Ru(0001) are magnetized in-plane.

would prefer to grow with fcc structure. The increase of Cu thickness tends to favor the in-plane magnetization.

6.4 Summary and Conclusions

In conclusion, we deposited films of Cu onto 1 to 6 ML of Co on Ru(0001) in the thickness range of up to 2 atomic monolayers. We found that Cu produces two sharp spin reorientation transitions only in the films composed by 3 or 4 ML Co/Ru(0001): the films without Cu are magnetized in-plane; the films with one monolayer of Cu are magnetized out-of plane; the films with two or more monolayers of Cu are magnetized in-plane again. The Curie temperature of the perpendicularly magnetized system 1 ML Cu/3–4 ML Co/Ru(0001), is above 510 K. Preliminary results of our first principles calculations suggest that both transitions are associated with a structural transformation.

Chapter 7

Summary and Conclusions

"The most exciting phrase to hear in science, the one that heralds new discoveries, is not 'Eureka!' (I have found it!) but 'That's funny...'"

— Isaac Asimov 1920–1992

In this thesis diverse magnetic SRTs have been investigated by means of LEEM and SPLEEM. The results presented for the different thin films of Co over Ru prove the applicability of our experimental approach. We start with the simplest system, just a Ru(0001) single crystal substrate. Using a LEEM instrument we have performed, for the first time, a LEED I-V analysis from a single atomic Ru(0001) terrace. The experimental I-V curves were excellently fit by full dynamical calculations. The best-fit parameters are shown in Table 3.1. In the best-fit structure, the topmost Ru layer is relaxed inward by about 3.5%, in excellent agreement with *ab-initio* calculations. We suggest that determining structures from small areas has clear advantages even for unreconstructed surfaces, such as Ru.

The next step was to grow Co on the Ru(0001) surface: we followed in real time the growth dynamics and studied its structure in detail by means of LEEM, LEED and dynamical IV calculations. The large terraces found on the Ru substrate allow Co to grow layer-by-layer despite the large difference in in-plane lattice parameters. We show in Figure 4.16a an schematic of the structures derived in the present work. The first layer grows pseudomorphically and continues the hcp stacking sequence of the Ru(0001) substrate. The shape of the islands is triangular, exposing {100}-type steps, and the orientation rotates 180° in consecutive terraces, as expected from the hcp substrate.

Thicker films reconstruct in order to recover the Co bulk in-plane lattice constant, yielding satellite spots in the diffraction patterns. For these coverages, and although at the limit of our sensitivity, best IV fits are always obtained for weighted mixtures of hcp and fcc stackings between the bottommost Co layer and the topmost Ru layer. The second layer of Co also forms triangular-like islands. The orientation now is inverted with respect to the 1 ML, and there is only one stacking sequence within the film itself. The third layer grows again in triangular islands, but this time it presents islands with two orientations. By selected area LEED IV-analysis, we confirm the correspondence between island orientation and stacking-sequence in the 3 ML islands: the two regions experimentally detected correspond to the two possible stacking sequences of the 3^{rd} layer on top of the 2 ML film. In the future we expect to complement the data presented here with a full IV analysis, including satellite spots, of the thicker films.

Once we knew the detailed structure of the ultrathin films of Co on Ru(0001) we studied its magnetic properties by means of SPLEEM. The resultant SPLEEM images show the power of this yet relatively unisual microscopy technique for magnetic studies. We deposited films of Co on Ru(0001) in the thickness range of up to 3 atomic monolayers and find that the Curie temperature is well above room temperature provided the thickness is more than a single atomic monolayer. We observe two sharp reorientation transitions of the magnetization: 1 ML as well as 3 ML or thicker Co films have an in-plane easy axis, while only 2 ML thick films are magnetized in the out-of plane direction. The first transition is associated with a structural transformation from laterally strained, pseudomorphic 1 ML thick films to relaxed 2 ML thick films. Our first principles calculations show that the in-plane easy-axis of one- and three-monolayer films is stable with respect to variations of the strain conditions. Only for two-monolayer films, the combination of strain with additional interface and surface effects drives the magnetic easy-axis into the out-of-plane direction. The knowledge of the stacking and island shape structure revealed here, along with the interesting magnetic properties of the first layers and the limited intermixing, makes the Co/Ru system an excellent combination for basic and applied material research studies.

The use of capping layers is a standard practice for measuring the magnetic properties ex-situ. We have studied the growth and magnetism of Cu capping layers over the system that we have studied in previous chapters: Co/Ru(0001). We deposited films of Cu onto 1 to 6 ML of Co on Ru(0001) in the thickness range of up to 2 atomic monolayers. We found that Cu produces two sharp spin reorientation transitions only in films composed by 3 or 4 ML Co/Ru(0001): films without Cu are magnetized in-plane; films with

one monolayer of Cu are magnetized out-of plane; films with two or more monolayers of Cu are magnetized in-plane again. The Curie temperature of the perpendicularly magnetized system 1 ML Cu/3–4 ML Co/Ru(0001), is above 510 K. Preliminary results of our first principles calculations suggest that both transitions are associated with a structural transformation of the growing Cu and probably of the topmost Co layer.

Conclusiones

En el transcurso de esta tesis hemos estudiado varias reorientaciones de la dirección de imanación mediante LEEM y SPLEEM. Los resultados presentados para las diferentes películas delgadas de Co sobre Ru demuestran la utilidad de nuestro método experimental. Hemos decidido empezar por el sistema más simple: la superficie de nuestro substrato, el monocristal de Ru(0001). Mediante el LEEM hemos realizado por primera vez un análisis de difracción cuantitativa de electrones lentos (LEED IV) en una terraza sin escalones del Ru(0001). Hemos encontrado un ajuste excelente de las curvas IV experimentales mediante cálculos dinámicos. Los parámetros con los mejores ajustes pueden verse en la Tabla 3.1. En el mejor ajuste la última capa de Ru está contraída alrededor de un 3.5%, coincidiendo con los cálculos de primeros principios encontrados en la literatura. Hemos demostrado que determinar las estructuras estudiando regiones pequeñas de la superficie tiene ventajas claras incluso para superficies no reconstruidas como la del Ru.

El siguiente paso fue crecer Co en la superficie de Ru(0001). Hemos seguido en tiempo real el crecimiento y hemos estudiado en detalle su estructura. En resumen, hemos estudiado el crecimiento de las primeras capas de Co en Ru(0001) mediante LEEM, LEED y cálculos dinámicos IV. Las terrazas de gran tamaño que encontramos en el Ru permiten crecer el Co capa a capa a pesar de la diferencia de parámetros de red en el plano. La Figura 4.16a muestra un esquema de las estructuras encontradas en este trabajo. La primera capa crece pseudomórfica y sigue la secuencia de apilamiento hcp del substrato de Ru(0001). La forma de las islas es triangular, con bordes tipo {100}, y la orientación rota 180° en terrazas consecutivas como es de esperar en un substrato hcp. Las películas de más de una monocapa (MC) de Co se reconstruyen para acercarse al parámetro de red del Co en volumen, produciendo haces satélite en los patrones de difracción. Para dichos recubrimientos, los mejores ajustes IV se obtienen para estructuras mixtas compuestas por redes hcp y fcc entre el Ru y la primera capa de Co (en la intercara). La segunda capa de Co también crece en islas triangulares. La orientación sin embargo está invertida con respecto a las islas triangulares de la primera MC. Solo hay una secuencia de apilamiento en la película de Co. La tercera capa crece de nuevo en islas de forma triangular, pero en este caso con dos orientaciones diferentes. Mediante un análisis LEED IV en pequeñas regiones de la superficie hemos confirmado la correspondencia entre la orientación de las islas y la secuencia de apilamiento en las islas de 3 MC: las dos regiones detectadas experimentalmente corresponden a las dos

secuencias de apilamiento para la tercera MC encima de la película de 2 MC. En el futuro esperamos completar los datos presentados con un análisis completo de curvas IV, incluyendo los haces satélite, de estas películas.

Una vez resuelta la estructura de las películas ultradelgadas de Co en Ru(0001) procedimos al estudio de sus propiedades magnéticas mediante SPLEEM. Las imágenes de SPLEEM muestran la potencia de este microscopio para estudios de magnetismo, del cual solo hay tres disponibles en el mundo. Hemos crecido películas de Co en Ru(0001) de una a tres MC y hemos descubierto que la temperatura de Curie está muy por encima de temperatura ambiente cuando el grosor es mayor de una MC. Hemos medido dos transiciones de reorientación de la dirección de imanación durante el crecimiento: 1 y 3 MC de Co tienen su dirección de imanación dentro del plano de la superficie; 2 MC tienen su dirección de imanación perpendicular a la superficie. La primera transición está asociada con la transformación estructural de la primera MC (pseudomórfica con el Ru y tensionada lateralmente) a la segunda (relajada). Los cálculos de primeros principios demuestran que la dirección de magnetización en el plano para 1 y 3 MC permanece estable frente a variaciones en las tensiones. Sólo para películas de dos MC de Co la interacción entre los efectos producidos por las tensiones, la superficie y la intercara pueden desembocar en un eje fácil de imanación perpendicular. Dadas las interesantes propiedades magnéticas que poseen sus primeras MC del sistema Co/Ru lo convierten en una combinación excelente para la investigación en ciencia de materiales básica y aplicada.

El uso de capas de recubrimiento (capping layers) es una técnica estándar para proteger los sistemas magnéticos en medidas ex-situ. Hemos estudiado el crecimiento y el magnetismo de capas de Cu sobre el sistema Co/Ru(0001). Hemos depositado las películas de Cu sobre 1–6 MC de Co en Ru(0001) en grosores desde 1 a 2 capas atómicas. Hemos encontrado que las capas de Cu producen dos nuevas reorientaciones de la dirección de imanación sólo en películas de 3 o 4 MC de Co/Ru(0001): las películas sin Cu están magnetizadas en el plano; las películas con una MC están magnetizadas en dirección perpendicular; las películas con 2 o más MC de Cu están magnetizadas de nuevo en el plano. La temperatura de Curie del sistema totalmente magnetizado en dirección perpendicular 1 MC Cu/3–4 MC Co/Ru(0001) es alrededor de 510 K. Resultados preliminares de cálculos de primeros principios sugieren que las dos transiciones están relacionadas con transformaciones estructurales del Cu y probablemente de la última capa de Co.

Appendix: Theoretical Methods

"Writing in English is the most ingenious torture ever devised for sins committed in previous lives."
— James Joyce, 1882–1941

§A-i LEED I-V analysis

Full dynamical I-V calculations were performed with a modified version of the Van Hove-Tong package [86, 127, 128]. The experiment-theory agreement was quantified via Pendry's R-factor [72] (R_P), while the error bars for each parameter were obtained from its variance: $\Delta R_P = R_P^{min} \times \sqrt{(8E_i/\Delta E)}$, where E_i gives the optical (inner) potential and ΔE corresponds to the total energy range analyzed. Correlations between the structural parameters were taken into account for the error-limits estimation. We note that all structural parameters derived in this thesis (see Table 3.1 and Table 4.1) presented well-defined minima in their respective R-factor plots. Non-structural parameters such as the muffin-tin radius (r_m), the optical potential (E_i) or the Debye temperatures at the surface planes were varied. They were, however, not systematically optimized, since we checked that they had no impact on the final structural conclusions. Next sections explain the details of the two modeled system presented in this thesis.

§A-i.1 Clean Ru(0001)

The surface was modeled by stacking two Ru atomic-planes on top of a Ru(0001) bulk. Well-converged values for both the number of beams and the number of phase shifts ($l_{max} = 8$) were employed. In the structural search only normal displacements for the first two Ru atomic planes were considered (d_1 and d_2). The resulting parameter space was fully explored by calculating the I-V curves over a fine 2D grid where d_1 and d_2 were swept over wide ranges.

§A-i.2 Co on Ru(0001)

The surface was modeled by stacking the required number of Co atomic planes (1, 2 or 3) on top of two Ru atomic planes. The surface layers were then stacked on top of the bulk Ru(0001) using the Renormalized Forward Scattering (RFS) approach. Well-converged values for both the number of beams and the number of phase shifts ($l_{max} = 8$) were employed in all cases. Relativistic phase-shifts [129] —spin averaged later— were calculated for each stacking sequence from 2 dimensional (2D) slabs containing 8-10 atomic layers in total. The parameter space, comprising of the stacking sequence of the Co layers and the first three interlayer spacings, d_{1-3}, was fully explored by calculating the IV curves over fine 3D-grids where the d_is were swept over wide ranges for all possible stacking sequences of the Co layers. We also included the in-plane lattice parameter, $a_{\|}$, in the structural search. $a_{\|}$ was made common to all surface and bulk layers. Since the R-factor turned out to be rather insensitive to d_3 and d_{bulk}, while their inclusion in the IV-analysis increased significantly the error bars for the rest of parameters, we fixed both to the bulk Ru spacing, d_{bulk}=2.14 Å. All simulations were performed for a temperature T=300 K using an energy increment of 2 eV.

§A-ii Magnetic Anisotropy Energy *Ab-initio* Calculations

All ab-initio calculations presented here have been performed by using the SKKR method, i.e., a Green's function formalism relying on density functional theory. Details of the method can be found in Ref. [112]. The self-consistent potentials and effective fields are calculated for layers embedded between two semi–infinite systems using a surface Green's function technique. The intermediate region under study is formed by the Co film with two to three buffer layers of Ru on the substrate side and layers of empty spheres beyond the surface, thus representing a smooth transition from the substrate to the vacuum. The semi–infinite regions are the perfect bulk Ru and the vacuum, respectively, the latter described by a constant potential also determined self-consistently. A common two-dimensional translational symmetry is required for all layers in these three regions, while the interlayer distances can be varied independently. We considered different hcp structures ranging between the Ru bulk (a = 2.71 Å, c/a = 1.58) and the Co bulk (a = 2.51 Å, c/a = 1.63). More specifically, we have chosen a = 2.71 Å, a = 2.65 Å and a = 2.60 Å, the latter being the experimental lattice parameter estimated for the thicker Co films. Energy integrations have been performed along a semicircular contour using a 16-point Gaussian sampling on an asymmetric mesh; the k-integrations have been performed using 180 points in the Surface Brillouin Zone (SBZ). According to the experimental results, only ferromagnetic configurations have been considered for the Co film. The magnetic moments show minor variations between the different structures, and, in general, the spin and orbital moments of the Co atoms are around 1.6 μ_B and 0.1 μ_B, respectively, with a slight enhancement in the surface layer. The interface Ru

atoms show an induced spin polarization that oscillates between -0.08 μ_B and 0.03 μ_B, depending on the structure and the Co film thickness.

In the spirit of the magnetic force theorem, the MAE is calculated as the sum of two terms: the band energy contribution, ΔE_b, and the magnetostatic dipole-dipole interaction energy, ΔE_{dd}. The latter is equivalent to the shape anisotropy, while the former incorporates the magnetocrystalline and the magnetoelastic terms. ΔE_b is obtained by using the fully relativistic version of the SKKR method [112]. It is defined as

$$\Delta E_b = \int_{-\infty}^{\epsilon_F} (\epsilon - \epsilon_F) \Delta n(\epsilon) d\epsilon \ , \tag{A1.1}$$

with $\Delta n(\epsilon)$ being the difference of the local density of states with respect to a uniform in-plane and a uniform normal-to-plane orientation of the magnetization, and ϵ_F denoting the Fermi level of the non-magnetic substrate. Since ΔE_b is only of the order of a few tenths of meV, its corresponding calculation requires a rigorous convergence test with respect to the number of k-points chosen for the SBZ integrations. Here convergence has been achieved by taking $\sim 4 \cdot 10^4$ k-points in the SBZ, a much larger value than required for the self-consistent calculations. E_{dd} is calculated by using the layer–dependent dipole–dipole Madelung constant matrix, $M_{p,q}$, evaluated in terms of a two-dimensional Ewald method,

$$E_{dd}(\hat{n}) = \sum_{p,q} \frac{m_p m_q}{c^2} \hat{n} M_{p,q} \hat{n} \tag{A1.2}$$

where m_p denotes the magnitude of the magnetic moment in a layer labelled by p, c is the velocity of light, and the unit vector $\hat{n}$ refers to a uniform orientation of the magnetization.

In order to estimate the preferred relaxation of the interlayer distances for the different lattices we assume that atoms try to maintain the nearest-neighbors (NN) distances of their bulk materials, with Co-Ru distances being an average of the preferred Co-Co and Ru-Ru interlayer distances. In the ideal hcp case (c/a = 1.63) each atom has 12 NN which along the [0001] direction are distributed as follows: 6 in-plane, 3 in the upper adjacent plane and 3 in the lower adjacent plane. For the Ru lattice with c/a = 1.58, the NN distance with respect to the adjacent layers, $d_{NN}^{\perp}$, is slightly less than the in-plane one, $d_{NN}^{\parallel}$. The corresponding $d_{NN}^{\perp}$ can easily be expressed in terms of the interlayer spacing, d, and the two-dimensional lattice parameter, a, as

$$d_{NN}^{\perp} = \sqrt{\frac{a^2 + 3d^2}{3}} \ . \tag{A1.3}$$

For the bulk Co and Ru lattices $d_{NN}^{\perp}$ is 2.51 Å and 2.65 Å, respectively. When Co and Ru atoms form a lattice with an in-plane lattice parameter a that is different from the corresponding bulk value, they recover $d_{NN}^{\perp}$ by adjusting the interlayer spacing d according to Eq. (A1.3). In a Ru-like lattice this leads to a perpendicular contraction of 8% for the Co layers. With a = 2.60 Å and an ideal hcp structure, d is contracted by 7% for the Co layers while the Ru layers tend to expand by 3%. Accordingly, in this case, the corresponding Co-Ru interlayer distance is expected to relax less than 2%.

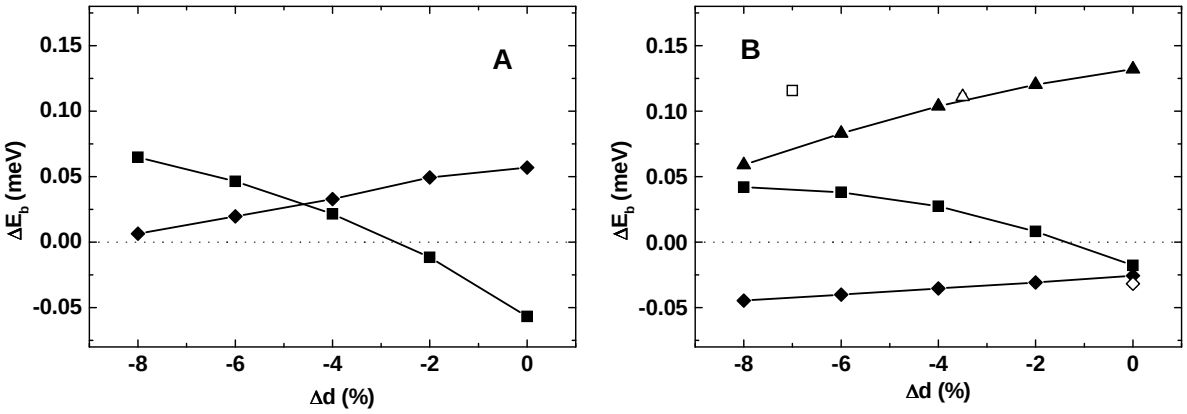

Figure A1: Calculated layer-resolved ΔE_b of Co films under uniform relaxations of d. (A) pseudomorphic 1 ML films: diamonds, interface Ru; squares, surface Co. (B, solid symbols) in-plane strained 2 ML thick films: diamonds, interface Ru; squares, surface Co; triangles, interface Co. In panel (B), the corresponding open symbols refer to the 2 ML film with non-uniform interlayer relaxations of fig.4d.

Bibliography

[1] C. P. Bean and J. D. Livingston, J. Phys. Lett. **30**, 1205 (1959).

[2] E. Bauer, Rep. Prog. Phys. **57**, 895 (1994).

[3] T. Duden and E. Bauer, Surf. Rev. Lett. **5**, 1213 (1998).

[4] E. Fullerton, D. Margulies, M. Schabes, M. Carey, B. Gurney, A. Moser, M. Best, G. Zeltzer, K. Rubin, H. Rosen, and M. Doerner, App. Phys. Lett. **77**, 3806 (2000).

[5] K. Ounadjela, D. Muller, A. Dinia, A. Arbaoui, P. Panissod, and G. Suran, Phys. Rev. B **45**, 7768 (1992).

[6] C. L. Dennis, R. P. Borges, L. D. Buda, U. Ebels, J. F. Gregg, M. Hehn, E. Jouguelet, K. Ounadjela, I. Petej, I. L. Prejbeanu, and M. J. Thornton, J. Phys.: Condens. Matt. **14**, R1175 (2002).

[7] D. Muller, K. Ounadjela, P. Vennegues, V. Pierron-Bohnes, A. Arbaoui, J. P. Jay, A. Dinia, and P. Panissod, J. Mag. Mag. Mat. **104-107**, 1873 (1992).

[8] C. Liu and S. D. Bader, J. Mag. Mag. Mat. **119**, 81 (1993).

[9] H. F. Ding, A. K. Schmid, D. Li, K. Y. Guslienko, and S. D. Bader, Phys. Rev. Lett. **94**, 157202 (2005).

[10] C. T. Yu, D. Q. Li, J. Pearson, and S. D. Bader, Appl. Phys. Lett. **78**, 1228 (2001).

[11] F. El Gabaly, S. Gallego, C. Munoz, L. Szunyogh, P. Weinberger, C. Klein, A. K. Schmid, K. F. McCarty, and J. de la Figuera, Phys. Rev. Lett. **96**, 147202 (2006).

[12] L. Royer, Bull. Soc. Fr. Min. **51**, 7 (1928).

[13] E. Bauer, App. Surf. Sci. **11**, 479 (1982).

[14] F. C. Frank and J. H. van der Merve, Proc. Roy. Soc. (London) A **198**, 205 (1949).

[15] N. C. Bartelt, `morse` code version 2, 1998, calculated with the software `morse2` written by Norm C. Bartelt. It uses a Morse potential between adsorbate atoms, which are over a corrugated potential. The parameters are chosen to show clearly the relaxation of the initial 14×14 moiré structure (in the example shown in this work).

[16] Y. I. Frenkel and T. Kontorova, Zh. Eksp. Teor. Fiz. **8**, 1340 (1938).

[17] A. Hinchliffe, *Molecular Modelling for Beginners* (John Wiley & Sons, West Sussex, 2003).

[18] P. F. Carcia, A. D. Meinhaldt, and A. Suna, Appl. Phys. Lett. **47**, 178 (1985).

[19] P. Grünberg, R. Schreiber, Y. Pang, M. B. Brodsky, and H. Sowers, Phys. Rev. Lett. **57**, 2442 (1986).

[20] M. N. Baibich, J. M. Broto, A. Fert, van Dau F. Nguyen, F. Petroff, P. Eitenne, G. Creuzet, A. Friederich, and J. Chazelas, Phys. Rev. Lett. **61**, 2472 (1988).

[21] P. Bruno, Phys. Rev. B **39**, 865 (1989).

[22] S. Chikazumi and J. Lothe, *Physics of Magnetism* (Wiley, New York, 1964).

[23] C. M. Schneider, P. Bressler, P. Schuster, J. Kirschner, J. J. de Miguel, and R. Miranda, Phys. Rev. Lett. **64**, 1059 (1990).

[24] D. J. Craik and R. S. Tebble, *Ferromagnetism and Ferromagnetic Domains* (North-Holland, Amsterdam, 1965).

[25] R. Carey and E. D. Isaac, *Magnetic Domains and Techniques for their Observation* (Academic Press, New York, 1966).

[26] A. Hubert and R. Schäfer, *Magnetic Domains* (Spriger-Verlag, Berlin, 2000).

[27] R. Allenspach, J. Mag. Mag. Mat. **129**, 160 (1993).

[28] L. L. Hirst, Rev. Mod. Phys. **69**, 607 (1997).

[29] D. Sander, Rep. Prog. Phys. **62**, 809 (1999).

[30] D. Sander, J. Phys. **16**, R603 (2004).

[31] L. Néel, J. Phys. Radium **15**, 225 (1954).

[32] U. Gradmann, J. Appl. Phys. **40**, 1182 (1969).

[33] A. Aharoni, *Introduction to the Theory of Ferromagnetism* (Oxford University Press, Oxford, 2000).

[34] D. P. Pappas, K.-P. Kämper, and H. Hopster, Phys. Rev. Lett. **64**, 3179 (1990).

[35] Z. Q. Qiu and S. D. Bader, Phys. Rev. Lett. **70**, 1006 (1993).

[36] B. Schulz and K. Baberschke, Phys. Rev. Lett. **50**, 13467 (1994).

[37] D. R. Penn, Phys. Rev. B **13**, 5248 (1976).

[38] T. N. Rhodin and J. W. Gadzuk, *The Nature of the Surface Chemical Bond* (North-Holand, Amsterdam, 1976).

[39] G. Somorjai, *Chemistry in Two Dimensions: Surfaces* (Cornell, Ithaca, 1981).

[40] A. Zangwill, *Physics at Surfaces* (Cambridge University Press, Cambridge, 1988).

[41] R. M. Tromp, IBM J. Res. Dev. **44**, 503 (2000).

[42] H.-C. Kan and R. J. Phaneuf, J. Vac. Sci. and Technol. **19**, 1158 (2001).

[43] E. Bauer, Surf. Rev. Lett. **5**, 1275 (1998).

[44] M. S. Altman, W. F. Chung, and C. H. Liu, Surf. Rev. and Lett. **5**, 1129 (1998).

[45] R. J. Phaneuf and A. K. Schmid, Physics Today **56**, (2003).

[46] E. Bauer, Surf. Sci. **299/300**, 102 (1993).

[47] E. Bauer, App. Surf. Sci. **92**, 20 (1996).

[48] A. K. Schmid, N. C. Bartelt, and R. Q. Hwang, Science **290**, 1561 (2000).

[49] S. Kodambaka, S. V. Khare, W. Swiech, K.Ohmori, I. Petrov, and J. Greene, Nature **429**, 49 (2004).

[50] K. F. McCarty, J. A. Nobel, and N. Bartelt, Nature **412**, 622 (2001).

[51] F. El Gabaly, W. L. W. Ling, K. F. McCarty, and J. de la Figuera, Science **308**, 1303 (2005).

[52] V. Kolaric, M. Mankos, and L. Veneklasen, Optik **87**, 1 (1991).

[53] G. D. Archard and T. Mulvey, J. Sci. Instrum. **35**, 279 (1958).

[54] A. Walther, *The Ray and Wave Theory of Lenses* (Cambridge University Press, Cambridge, 1995).

[55] E. Bauer, T. Duden, and R. Zdyb, J. Phys. D: Appl. Phys **35**, 2327 (2002).

[56] Wikipedia, Micro-channel plate, Website, 2006, `http://en.wikipedia.org/wiki/Micro-channel_plate`.

[57] W. F. Chung and M. S. Altman, Ultramicroscopy **74**, 237 (1998).

[58] P. Falstad, Fresnel Diffraction Applet, Java applet, `http://www.falstad.com/diffraction`.

[59] M. S. Altman, W. F. Chung, Z. Q. He, H. C. Poon, and S. Y. Tong, Appl. Surf. Sci. **169-170**, 82 (2001).

[60] D. Menzel, Surf. Sci. **318**, 437 (1994).

[61] J. E. Prieto, C. R. , S. Muller, R. Miranda, and K. Heinz, Surf. Sci. **401**, 248 (1998).

[62] D. B. Williams and C. B. Carter, *Trasmission Electron Microscopy* (Plenum Press, New York, 1996).

[63] R. Ramchal, A. K. Schmid, M. Farle, and H. Poppa, Phys. Rev. B **69**, 214401 (2004).

[64] H. Hopster and H. P. O. (Eds.), *Magnetic Microscopy of Nanostructures* (Springer-Verlag, Berlin, 2005).

[65] K. Grzelakowski, T. Duden, E. Bauer, H. Poppa, and S. Chiang, IEEE Trans. Magn. **30**, 4500 (1994).

[66] T. Duden and E. Bauer, Rev. Sci. Instr. **66**, 2861 (1995).

[67] S. T. Pierce and F. Meier, Phys. Rev. B **13**, 5484 (1976).

[68] R. Cun-Jun, Chin. Phys. **12**, 483 (2003).

[69] P. A. Hayes, D. H. Yu, and J. F. Williams, Rev. Sci. Instrum. **68**, 1708 (1997).

[70] H. Poppa, E. D. Tober, and A. K. Schmid, J. App. Phys. **91**, 6932 (2002).

[71] J. A. Rodriguez and D. W. Goodman, Surf. Sci. Rep. **14**, 1 (1991).

[72] J. Pendry, J. Phys. C **13**, 937 (1980).

[73] G. Michalk, W. Moritz, H. Pfnür, and D. Menzel, Surf. Sci. **129**, 92 (1983).

[74] P. J. Feibelman, J. E. Houston, H. L. Davis, and D. G. Oneill, Surf. Sci. **302**, 81 (1994).

[75] P. J. Feibelman, Surf. Sci. **360**, 297 (1996).

[76] L. Xu, H. Y. Xiao, and X. T. Zu, Chem. Phys. **315**, 155 (2005).

[77] A. P. Baddorf, V. Jahns, D. M. Zehner, H. Zajonz, and D. Gibbs, Surf. Sci. **498**, 74 (2002).

[78] G. Held, S. Uremovic, and D. Menzel, Surf. Sci. **331-333**, 1122 (1995).

[79] J. B. Maxson, N. Perkins, D. E. S. nad A. R. Woll, L. Zhang, T. F. Keuch, and M. G. Lagally, Surf. Sci. **464**, 217 (2000).

[80] M. Lindroos, H. Pfnür, and D. Menzel, Phys. Rev. B **33**, 6684 (1986).

[81] J. R. S. Å . Lindgren, L. Walldén and P. Westrin, Phys. Rev. B **29**, 576 (1984).

[82] S. D. Ruebush, R. E. Couch, S. Thevuthasan, and C. S. Fadley, Surf. Sci. **421**, 205 (1999).

[83] K. Meinel, M. Klaua, and H. Bethge, Phys. Stat. Sol. (a) **110**, 189 (1988).

[84] J. de la Figuera, J. E. Prieto, C. Ocal, and R. Miranda, Phys. Rev. B **47**, 13043 (1993).

[85] L. J. Clarke, *An Introduction To Low-energy Electron Diffraction* (Wiley, New York, 1985).

[86] M. A. Van Hove and S. Y. Tong, *Surface Crystallography by LEED* (Springer-Verlag, Berlin, 1979).

[87] J. de la Figuera, F. El Gabaly, J. M. Puerta, J. I. Cerda, and K. F. McCarty, Surf. Sci. **600**, L105 (2006).

[88] F. C. Frank, Phil. Mag. **42**, 1014 (1951).

[89] E. Lundgren, B. Stanka, M. Schmid, and P. Varga, Phys. Rev. B **62**, 2843 (2000).

[90] J. de la Figuera, A. K. Schmid, N. C. Bartelt, K. Pohl, and R. Q. Hwang, Phys. Rev. B **63**, 165431 (2001).

[91] R. Pushpa and S. Narasimhan, Phys. Rev. B **67**, 205418 (2003).

[92] W. L. Ling, T. Giessel, K. Thurmer, R. Q. Hwang, N. C. Bartelt, and K. F. McCarty, Surf. Sci. **570**, L297 (2004).

[93] R. Q. Hwang, C. Günther, J. S. Günther, E. Kopatzki, and R. J. Behm, J. Vac. Sci. Tech. **10**, 1970 (1992).

[94] C. Günther, Ph.D. thesis, Lundwig-Maximilians Universität, 1994.

[95] M. Bott, T. Michely, and G. Comsa, Surf. Sci. **272**, 161 (1992).

[96] M. Kalff, G. Comsa, and T. Michely, Phys. Rev. Lett. **81**, 1255 (1998).

[97] S. Ovesson, A. Bogicevic, and B. I. Lundqvist, Phys. Rev. Lett. **83**, 2608 (1999).

[98] C. Günther, S. Günther, E. Kopatzki, R. Q. Hwang, J. Schröder, J. Vrijmoeth, and R. J. Behm, Ber. Bunsenges Phys. Chem. **97**, 522 (1993).

[99] J. de la Figuera, F. El Gabaly, N. C. Bartelt, and K. F. McCarty, in preparation (unpublished).

[100] G. Kellogg, private communication (unpublished).

[101] J. de la Figuera, private communication (unpublished).

[102] W. L. Ling, J. de la Figuera, N. C. Bartelt, R. Q. Hwang, A. K. Schmid, G. E. Thayer, and J. C. Hamilton, Phys. Rev. Lett. **92**, 116102 (2004).

[103] C. Busse, C. Polop, M. Muller, K. Albe, U. Linke, and T. Michely, Phys. Rev. Lett. **91**, 056103 (2003).

[104] D. W. Pashley, M. J. Stowell, M. H. Jacobs, and T. J. Law, Phil. Mag. **10**, 127 (1964).

[105] C. Busse and T. Michely, Surf. Sci. **552**, 281 (2004).

[106] S. Bleikamp, A. Thoma, C. Polop, G. Pirug, U. Linke, and T. Michely, Phys. Rev. Lett. **96**, 115503 (2006).

[107] W. L. Ling, N. C. Bartelt, K. F. McCarty, and C. B. Carter, Phys. Rev. Lett. **95**, 166105 (2005).

[108] P. Varga, E. Lundgren, J. Redinger, and M. Schmid, Phys. Stat. Sol. A **187**, 97 (2001).

[109] B. N. Engel, C. D. England, R. A. V. Leeuwen, M. H. Wiedmann, and C. M. Falco, Phys. Rev. Lett. **67**, 1910 (1991).

[110] M. T. Johnson, P. J. H. Bloemen, F. J. A. d. Broeder, and J. J. d. Vries, Rep. Prog. Phys. **59**, 1409 (1996).

[111] C. Chappert, H. Bernas, J. Ferre, V. Kottler, J.-P. Jamet, Y. Chen, E. Cambril, T. Devolder, F. Rousseaux, V. Mathet, and H. Launois, Science **280**, 1919 (1998).

[112] J. Zabloudil, R. Hammerling, L. Szunyogh, and P. Weinberger, *Electron Scattering in Solid Matter: a theoretical and computational treatise* (Springer-Verlag, Berlin, 2005).

[113] H. J. Elmers, J. Hauschild, H. Hoche, U. Gradmann, H. Bethge, D. Heuer, and U. Kohler, Phys. Rev. Lett. **73**, 898 (1994).

[114] O. Pietzsch, A. Kubetzka, M. Bode, and R. Wiesendanger, Science **292**, 2053 (2001).

[115] K. von Bergmann, Ph.D. thesis, Hamburg, 2004.

[116] H. J. F. Jansen, Phys. Rev. B **59**, 4699 (1999).

[117] S. S. P. Parkin, N. More, and K. P. Roche, Phys. Rev. Lett. **64**, 2304 (1990).

[118] A. Cebollada, R. Miranda, C. M. Schneider, P. Schuster, and J. Kirschner, J. Magn. Magn. Mat. **102**, 25 (1991).

[119] F. Wilhelm, U. Bovensiepen, A. Scherz, P. Poulopoulos, A. Ney, G. C. H. Wende, and K. Baberschke, J. Magn. Magn. Mat. **222**, 163 (2000).

[120] M. Madami, S. Tacchi, G. Carlotti, G. Gubbiotti, and R. L. Stamps, Phys. Rev. B **69**, 144408 (2004).

[121] H. J. Elmers, J. Hauschild, and U. Gradmann, Phys. Rev. B **59**, 3688 (1999).

[122] W. Weber, A. Bischof, D. Pescia, and R. Allenspach, Nature **374**, 788 (1995).

[123] A. K. Schmid, D. Atlan, H. Itoh, B. Heinrich, T. Ichinokawa, and J. Kirschner, Phys. Rev. B **48**, 2855 (1993).

[124] A. K. Schmid, J. C. Hamilton, N. C. Bartelt, and R. Q. Hwang, Phys. Rev. Lett. **77**, 2977 (1996).

[125] J. de la Figuera, J. E.Prieto, C. Ocal, and R. Miranda, Surf. Sci. **307–309**, 538 (1994).

[126] J. E. Prieto, C. (Rath), S. Muller, R. Miranda, and K. Heinz, Surf. Sci. **401**, 248 (1998).

[127] J. Cerdá, Ph.D. thesis, Universidad Autnoma de Madrid, 1995.

[128] H. Huang, S. Tong, W. E. Packard, and M. B. Webb, Phys. Lett. A **130**, 166 (1988).

[129] M. A. V. Hove and A. Baraldi, private communication (unpublished).

List of Figures

List of Tables

List of Publications

♢ F. El Gabaly, R. Miranda, and J. de la Figuera, *Properties of dislocation half loops in Au(100): Structure, formation energy,and diffusion barrier*, Phys. Rev. B **70**, 012102 (2004).

♢ F. El Gabaly, W.L.W. Ling, K.F. McCarty, and J. de la Figuera, *The importance of Threading Dislocations on the Motion of Domain Boundaries in Thin Films*, Science **308**, 1303 (2005). Mentioned in Science magazine weekly highlights (Fig. I).

♢ J. de la Figuera, J.M. Puerta, J.I. Cerda, F. El Gabaly, K.F. McCarty, *Determining the structure of Ru(0001) from low-energy electron diffraction of a single terrace*, Surf. Sci. **600**, L105 (2006).

♢ F. El Gabaly, S. Gallego, C. Muñoz, L. Szunyogh, P. Weinberger, C. Klein, A.K. Schmid, K.F. McCarty, and J. de la Figuera, *Imaging Spin-Reorientation Transitions in Consecutive Atomic Co layers on Ru(0001)*, Phys. Rev. Lett. **96**, 147202 (2006). Cover of the suplemental magazine Physical Review Focus (Fig. II).

Submitted or in preparation

♢ F. El Gabaly, J.M. Puerta,C. Klein, A. Saa, A.K. Schmid, K.F. McCarty, J.I. Cerda, and J. de la Figuera, *Structure and morphology of the initial stages of the growth of cobalt on Ru(0001*, Submitted to New Journal of Physics

ABSTRACT: We follow the layer-by-layer growth of cobalt on ruthenium by means of low-energy electron microscopy (LEEM) and diffraction (LEED). The first monolayer grows pseudomorphically following the hcp stacking sequence. The vertical lattice spacing is contracted by 4% relative to the bulk ruthenium value. Films thicker than a monolayer present a relaxed in-plane lattice spacing, as detected by the presence of satellite spots in the diffraction pattern. By means of selected-area diffraction IV analysis we identify the stacking sequence of the different films. Films thinner than three monolayers are hcp without any stacking faults. Three monolayer thick islands nucleate in two different stacking sequences, starting the evolution of the

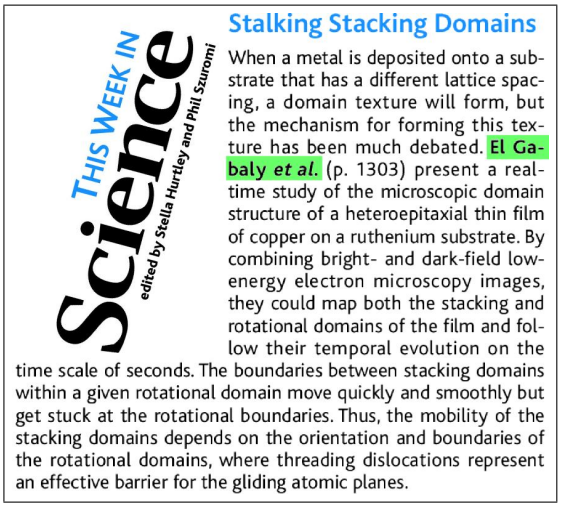

I: Science magazine weekly highlights (27 May 2005)

II: Physical Review Focus cover (18 April 2006)

film towards an fcc structure. The different stacking sequences of the islands are reflected in their shape, as proven by comparison with selected-area diffraction data.

♢ F. El Gabaly, N. Rougemaille, R. Stumpf, C. Klein, A.K. Schmid, N.C. Bartelt, J. de la Figuera, *Labyrinth-like atomic step motion during heteroepitaxial growth*, in preparation

ABSTRACT We report real-time and atomically resolved observations of the growth of Pd on Ru(0001) at high temperature. We find a novel growth mechanism in which the Pd only attaches at special points along the atomic step edges of the growing film. This results in a distinctive labyrinth-like growth front. We propose a model in which the formation of a surface alloy on slow moving regions the step edge poisons the step edge to growth. DFT calculations, STM observations and measurements of the growth velocity as a function of deposition flux support this model. We suggest that this growth mode will be characteristic of (technologically important) multicomponent systems in which one component passivates step edges.

♢ F. El Gabaly, C. Klein, K.F. McCarty, A.K. Schmid, and J. de la Figuera, *Multiple spin-reorientation transitions caused by consecutive copper capping layers on cobalt on ruthenium*, in preparation

ABSTRACT Capping layers on magnetic films can affect the properties of the underlying film. We report the spin-reorientation transition that takes place on three and four cobalt layers on Ru(0001) upon copper deposition. The bare films present an in-plane magnetization in remanence. By means of spin-polarized low energy electron microscopy we observe in real space with nanometer resolution how the magnetization changes to out-of-plane when depositing a single copper atomic layer. Deposition of an additional copper layer drives the magnetization in-plane. No further changes were observed. No other thicknesses below six cobalt layer show such behavior.

Acknowledgements

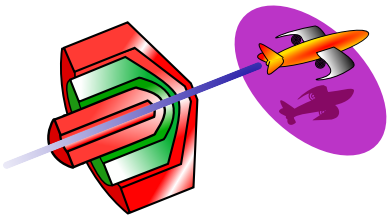

≻ Thanks ≺

Of the many people who deserve thanks, some are particularly prominent:

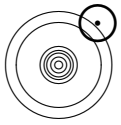

My supervisor, Juan de la Figuera, for teach me how to do research, for the chance to do it têtê-a-têtê and for your encouragement.

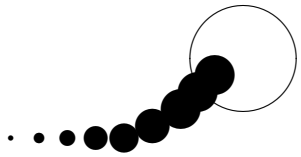

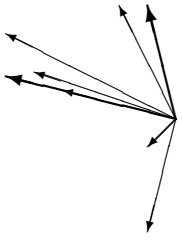

My USA *connectiON*: Andreas K. Schmid ($\sqrt{A/K_d}$ *Schmid*), Cristof Klein and Kevin F. McCarty, for open your laboratories and houses to me, and for the friendship forged in that wonderful summers in California. You show me how to become a LEEM fan.

$$\begin{array}{ccc} Madrid & \xrightarrow{f} & Berkeley \\ {\scriptstyle g}\downarrow & & \downarrow{\scriptstyle g'} \\ Livermore & \xrightarrow[f']{} & LaneSplitter \end{array}$$

Theoretician collaborators, Silvia Gallego, Carmen Muñoz, Juan M. Rodríguez Puerta y Jorge I. Cerda, your calculations represented an indispensable compliment to understand the *real life* data (always $\mathbf{dirt_{i_{e_r}}}$ than yours).

♢ Rodolfo Miranda, for believe in me since the beginning, and for the useful discussions and advises that I always enjoyed.

♠ Friends and colleges from the C-III (at UAM), specially Fabian Calleja, Juanjo Hinarejos (a.k.a *Body*), Cristina Navío, Pablo Nieto, Victor Joco. The leisure at the C-III was great in your company. Nikolai Mikuszeit, for the in-depth reading of the manuscript. Fabian, I am really looking forward to play guitar with you again .

$$[\,\xi \underset{yamaha}{\overset{gibson}{\rightleftarrows}} \vartheta\,]$$

♣ Elsa Fuentes and the technical staff at the C-III and at the SEGAINVEX, for working efficiently and always with a smile.

All the ⋆ CMAM ⋆ mates $(\underbrace{a+b+\cdots+z}_{\sim 26})$, specially Raquel G. Arrabal, Ángel Muñoz and Nuria Gordillo for the funny lunches and wise advises (received and given, je je).

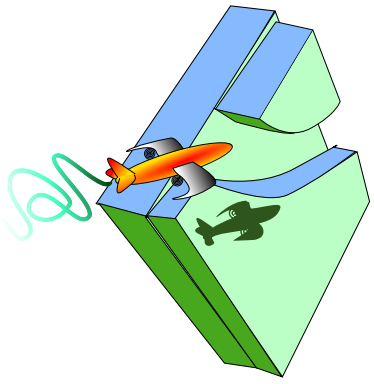

○ My parents, brother and sister, for their continuous encouragement and support. ○○○○